Inhomogeneities in Cosmology

David Kraljic

St Cross College

University of Oxford

A thesis submitted for the degree of

Doctor of Philosophy

Trinity 2016

Abstract

The standard ΛCDM cosmological model has been successful in accommodating most of the cosmological observations to date. However, there are still many theoretical and observational issues that this model needs to address before it can constitute a reliable framework in this era of 'precision cosmology'. In this thesis, we focus on some of these issues and shortcomings of the ΛCDM model that stem from inhomogeneities in the universe.

We begin by focusing on the generation of inhomogeneities by suggesting a generic approach to building suitable models for the origin of structure within the inflationary paradigm. This is in contrast with the study of specific models that has been commonly practised so far. Within the inflationary paradigm the universe in the earliest stages undergoes exponential expansion that stretches quantum fluctuations to astronomical scales, thus providing seeds of future structure. However, this inflationary phase can be generated by many different theoretical 'toy' models of inflation. To alleviate this arbitrariness, we argue that certain potentials for a scalar field are preferred from the viewpoint of the renormalisation group. We arrive at these potentials by decomposing generic UV complete theories for a scalar field in a way that isolates the part that dominates at energies lower than the initial UV scale of the theory. In our calculations, we adopt approximations usually made within the inflationary paradigm. We obtain predictions for the main inflationary observables consistent with the current measurements.

We continue by studying the way how the inhomogeneous distribution of matter can be characterised. The structure in the universe at late times exhibits complicated fractal-like behaviour. We propose new methods built on the ideas of anomalous diffusion and random walks to characterise this behaviour. Our methods complement the well-established 'count-in-spheres' approach. Moreover, we draw attention to and explicitly demonstrate biases that have existed in the previous applications of these methods, thus improving on them. Finally, we determine the distance scale above which the fractal behaviour disappears and the distribution of matter can be considered homogeneous.

The inhomogeneities can also be analysed in terms of the velocity field. We study the most extreme example of it observed to date, namely the 'Bullet Cluster', a system of two massive clusters of galaxies which have collided at a high relative speed. This collision poses a potential issue for the standard cosmological model since such mergers are expected to be extremely rare. We calculate the observationally relevant quantity – the expected number of such mergers on the sky in a survey complete up to some redshift. We find that, up to the redshift of the Bullet Cluster, we only expect about 0.1 such collisions. Many more similar merging clusters have been found recently, thereby increasing the tension with the ΛCDM model. We provide a formula for the expected number of mergers within the ΛCDM model given their collisional parameters and their redshift, which can be used to aid the future analyses and directly confront the model.

Finally, we focus on the role of the inhomogeneous velocity field in determining the background rate of expansion of space. The Hubble parameter, when measured in the

frame of the Local Group of galaxies, has less variation about the background value than when it is measured in the Cosmic Microwave Background frame. This appears to be at odds with the standard cosmological model in which the CMB frame is the one where quantities are expected to be most uniform. We quantify this apparent discrepancy and show that the boost to the frame that makes the Hubble flow most uniform for our position is in fact consistent with the standard model. We show that such boosts to the frame of most uniform flow are typical if observers are located in underdensities and participate in local bulk flows, which is indeed the case for our position.

Acknowledgements

I would like to express my gratitude to my supervisor Subir Sarkar for his support at various stages of my DPhil, collaboration, and insightful discussions on cosmology that stimulated most of the work in this thesis.

I would also like to thank Joe Conlon for his support as my co-supervisor in the first year of my DPhil.

I am grateful for the opportunity to collaborate with Sašo Grozdanov, Eirik Svanes, and Markus Rummel.

I would like to acknowledge the financial support of the STFC, the Rudolf Peierls Centre for Theoretical Physics, St Cross College, and hospitality of the Niels Bohr Institute, Copenhagen.

Statement of Originality

This thesis is based on original research and contains no material that has already been accepted, or is concurrently being submitted, for any degree or diploma or certificate or other qualification in this university or elsewhere. To the best of my knowledge and belief this thesis contains no material previously published or written by another person, except where due reference is made in the text.

Part of Chapter 2 is based on S. Grozdanov, D. Kraljic and E. E. Svanes, "Inflationary Potentials from the Exact Renormalisation Group," Nucl. Phys. B **909** (2016) 657

Chapter 3 is based on D. Kraljic, "Characterizing cosmic inhomogeneity with anomalous diffusion," Mon. Not. Roy. Astron. Soc. **451** (2015) no.4, 3393

Chapter 4 is based on D. Kraljic and S. Sarkar, "How rare is the Bullet Cluster (in a ΛCDM universe)?," JCAP **1504** (2015) no.04, 050

Chapter 5 is based on D. Kraljic and S. Sarkar,"Frames of most uniform Hubble flow," submitted to JCAP, arXiv:1607.07377

There is a further publication on an unrelated topic that is not part of this thesis: D. Kraljic, M. Rummel and J. P. Conlon, "ALP Conversion and the Soft X-ray Excess in the Outskirts of the Coma Cluster," JCAP **1501** (2015) no.01, 011

David Kraljic 2016

Contents

Chapter 1: Introduction

Modern cosmology, the study of the largest scales in the Universe, is a relatively new field. For centuries, cosmology was a philosophical discipline outside the realm of scientific investigation, despite the existence of a successful theory of gravity due to Newton. It was only with the introduction of Einstein's General Relativity (GR) in 1915 [1] that the equations for the geometry and dynamics of the whole Universe could be written down [2–5].

The development of the field of cosmology and the establishment of the standard model of cosmology have largely been dependent on observational breakthroughs, the most important of which were the discovery of the 'Hubble expansion' [6], the discovery of dark matter [7–10], Cosmic Microwave Background [11] and its temperature fluctuations [12], and the discovery of the accelerated expansion [13, 14].

In this chapter, we begin with a short review of the theoretical basis for the current mainstream understanding of cosmology. It is widely claimed that the field is currently entering the era of 'precision cosmology'. However, at the end of this chapter, we argue that there are still potential issues within the standard model which need to be addressed. These problems motivate most of the work within this thesis.

1.1 The standard model of cosmology

1.1.1 General relativity

The standard model of cosmology[1] is based on general relativity, which is a theory of gravity. GR surpassed the Newtonian theory by offering a completely different view of reality: absolute space and time with gravitational forces acting instantaneously over distance were replaced by one four dimensional entity, space-time, with gravity being its curvature. The curvature results in non-trivial trajectories for objects living in space-time. For example, paths of light rays bend near massive objects. This was the first observational test of GR, performed in 1919 by Eddington during a Solar eclipse, which

[1] Also called the concordance model.

led to wide acceptance of the theory.[2] Eddington's experiment confirmed the GR prediction for the amount of deflection and rejected the Newtonian prediction.

In this section, we briefly review the basics of Riemannian geometry, the mathematical description of curved space underpinning GR. We choose a simple heuristic approach for brevity; detailed and pedagogical treatments can be found in e.g. [15, 16].

Curved space-time is modelled as a smooth manifold. Physical quantities such as four-momentum vectors or stress-energy tensors 'live' in tangent spaces – flat approximations of the underlying manifold at each point. We need a prescription on how to move between infinitesimally close tangent spaces in order to follow vectors and tensors along paths in space-time or differentiate tensor fields. The problem is that, when moving from point to point, it is not only the components of tensors that change but also the basis vectors spanning their tangent spaces. Given a patch of curved space-time covered by a coordinate system $\{x^\mu, ...\}$, we therefore need a prescription for the infinitesimal change of basis vectors $\{\mathbf{e}_\mu, ...\}$ as the coordinates change by some δx^μ. We can express this infinitesimal change $\delta \mathbf{e}_\mu$ in terms of the original basis:

$$\delta \mathbf{e}_\mu / \delta x^\nu = \Gamma^\sigma_{\mu\nu} \mathbf{e}_\sigma. \tag{1.1}$$

where $\Gamma^\sigma_{\mu\nu}$ are called the connection coefficients.[3] Therefore, as we move by δx^μ, a vector $\mathbf{u} = u^\nu \mathbf{e}_\nu$ changes as:

$$\frac{\delta \left(u^\nu \mathbf{e}_\nu\right)}{\delta x^\mu} = \frac{\delta(u^\nu)}{\delta x^\mu}\mathbf{e}_\nu + u^\nu \frac{\delta(\mathbf{e}_\nu)}{\delta x^\mu} = \left(\frac{\partial u^\nu}{\partial x^\mu} + \Gamma^\nu_{\mu\sigma} u^\sigma\right) \mathbf{e}_\nu = \left(\nabla_\mu u^\nu\right) \mathbf{e}_\nu \tag{1.2}$$

Above we defined the appropriate derivative for curved space-time ∇_μ, which is called the covariant derivative. In addition to the usual partial derivative terms, it contains those terms involving the connection coefficients which encode the effects of curvature. Manifolds in GR are also equipped with the metric tensor $g_{\mu\nu}$ that enables the measurements of lengths of vectors and the formation of inner products. For example, $\mathbf{u} \cdot \mathbf{v} = u^\mu v^\nu \mathbf{e}_\mu \cdot \mathbf{e}_\nu = u^\mu v^\nu g_{\mu\nu}$. In any given coordinate system the metric is used to write

[2] Arguably, the first 'test' of GR was the correct value for the observed precession of the perihelion of Mercury calculated in 1915.

[3] Throughout this thesis we employ the summation convention.

line elements as well as volume elements:

$$\mathrm{d}s^2 = g_{\alpha\beta}\mathrm{d}x^\alpha \mathrm{d}x^\beta, \quad \mathrm{d}V = \sqrt{-g}\mathrm{d}x^4, \tag{1.3}$$

where g is the determinant of the metric.

The connection coefficient in GR is not arbitrary but is 'metric compatible' such that $\nabla_\mu g_{\alpha\beta} = 0$. This condition enables us to write the connection solely in terms of the metric:

$$\Gamma^\sigma_{\mu\nu} = \frac{1}{2} g^{\sigma\alpha} \left(\partial_\mu g_{\nu\alpha} + \partial_\nu g_{\mu\alpha} - \partial_\alpha g_{\mu\nu}\right). \tag{1.4}$$

Hence, the fundamental quantity describing space-time in GR is the metric.

A vector in flat space-time does not change when transported along two different paths to the same endpoint. However, a vector changes if transported in curved space-time. The size of the change encodes the amount of curvature in that region.

Let us move a vector $\mathbf{u}$ parallelly along a path determined by small displacement δa^μ. This means that $\delta\mathbf{u} = 0$ along the path or equivalently, upon using Eq.(1.2), that $\nabla_\mu u^\nu \delta a^\mu = 0$ in terms of components. Therefore, the change in the components of the vector u^ν is:

$$u^\nu \to u^\nu + \partial_\mu u^\nu \delta a^\mu + ... = u^\nu - \Gamma^\nu_{\mu\sigma} u^\sigma \delta a^\mu + ... \ . \tag{1.5}$$

Further transporting this vector in the direction δb^α gives:

$$u^\nu - \Gamma^\nu_{\mu\sigma} u^\sigma \delta a^\mu - \Gamma^\nu_{\beta\alpha}(\delta\alpha)\left[u^\beta - \Gamma^\beta_{\mu\sigma} u^\sigma \delta a^\mu + ...\right]\delta b^\alpha + ... \tag{1.6}$$

$$= u^\nu - \Gamma^\nu_{\mu\sigma} u^\sigma \delta a^\mu - \left(\Gamma^\nu_{\beta\alpha} + \partial_\rho \Gamma^\nu_{\beta\alpha}\delta a^\rho\right)\left[u^\beta - \Gamma^\beta_{\mu\sigma} u^\sigma \delta a^\mu + ...\right]\delta b^\alpha + ... \ . \tag{1.7}$$

Choosing a different path where the vector $\mathbf{u}$ is first transported along δb^α and then along δa^μ results in the same expression as above but with the indices $\alpha,\ \mu$ and vectors $a,\ b$ switched. By taking the difference between the vectors transported via two different paths, the terms linear in a and b cancel. We are thus left with:

$$\Delta u^\nu = \left(\partial_\mu \Gamma^\nu_{\beta\alpha} - \partial_\alpha \Gamma^\nu_{\beta\mu} + \Gamma^\beta_{\mu\sigma}\Gamma^\nu_{\beta\alpha} - \Gamma^\beta_{\alpha\sigma}\Gamma^\nu_{\beta\mu}\right) u^\sigma \delta a^\mu \delta b^\alpha + ... = R^\nu{}_{\sigma\alpha\mu} u^\sigma \delta a^\mu \delta b^\alpha + ... \tag{1.8}$$

Therefore, the difference in a transported vector to the same endpoint via different paths

is proportional to the Riemann tensor $R^{\nu}{}_{\sigma\alpha\mu}$ times the area that the two paths enclose. Hence, the Riemann tensor encodes the effects of curvature and is equal to zero in flat space-time. Note that the curvature tensor contains terms that are second order derivatives of the metric.

Contracting the Riemann tensor gives the trace part called the Ricci tensor:

$$R_{\mu\nu} = R^{\alpha}{}_{\mu\alpha\nu}, \tag{1.9}$$

which can be contracted further to construct the Ricci scalar:

$$R = R^{\alpha}{}_{\alpha}. \tag{1.10}$$

If the Ricci tensor is zero, then the Riemann tensor is trace free and is called the Weyl tensor.

The basic idea behind GR is *covariance*, that is, the invariance of equations under local coordinate transformations. Because the action is a scalar, the simplest covariant action that includes the curvature of space-time will have a term proportional to the Ricci scalar. This is called the Einstein-Hilbert action. Adding the matter Lagrangian and a constant term to the action yields:

$$S = \int \left[\frac{1}{2\kappa}R + \mathcal{L}_m + \Lambda\right]\sqrt{-g}\mathrm{d}x^4, \tag{1.11}$$

where R is the Ricci scalar, $\mathcal{L}_m$ is the matter Lagrangian, κ is a constant, and $\sqrt{-g}dx^4$ the proper volume element. The arbitrary constant term Λ, allowed by the requirement of covariance, is called the cosmological constant.

Varying the action above with respect to the metric results in the Einstein equations:

$$G_{\mu\nu} + \Lambda g_{\mu\nu} = \kappa T_{\mu\nu} \tag{1.12}$$

where $G_{\mu\nu} = R_{\mu\nu} - 1/2Rg_{\mu\nu}$. The stress-energy tensor $T_{\mu\nu}$ describing matter corresponds to $\frac{2}{\sqrt{-g}}\frac{\delta\mathcal{L}_m}{\delta g_{\mu\nu}}$. It can also be written for a perfect fluid in terms of the density ρ and the pressure p as $T_{\mu\nu} = (\rho + p)U_\mu U_\nu + pg_{\mu\nu}$, where U_μ is the four velocity of the fluid. The constant κ that encodes the coupling between matter and geometry is determined in the Newtonian limit to be $8\pi G c^{-4}$. The conservation of the stress-energy tensor, expressed

by the condition$\nabla_\mu T^\mu_\nu = 0$, is already encoded in the Einstein equations because of the geometrical requirement $\nabla_\mu G^\mu_\nu = 0$ called the Bianchi identity.

1.1.2 The Cosmological Principle and the background

The Copernican principle, states that the Earth is not the centre of the universe. The Cosmological Principle, first formulated by Milne [17], is a an extension of this and says that *no* position in the universe is special. The requirement that all observers are equivalent, meaning that the universe looks the same in all directions at each location, restricts the geometry of space to be isotropic and homogeneous. As the real universe has structure, the Cosmological Principle needs to be understood in statistical terms. That is, the principle only holds on average for an ensemble of observers. In practice this means, as we cannot move from our location in the universe, that ensemble averages are replaced by volume averages with us at the centre.

The standard cosmological model is based on the assumption of the existence of a background Friedmann-Lemaitre-Robertson-Walker (FLRW) geometry [2–5] that embodies the homogeneity and isotropy and can be written as:[4]

$$ds^2 = dt^2 - a(t)^2 \left(\frac{dr^2}{1 - kr^2} + r^2 \left(d\theta^2 + \sin^2 \theta d\phi^2 \right) \right), \tag{1.13}$$

where constant k describes the curvature of the spatial part of space-time. If k is positive, then the spatial sections are three-spheres, if k is zero, then the sections are flat and Euclidean, and if k is negative, then the sections are hyperbolic. The cosmic time t corresponds to the proper time of observers at rest in the FLRW coordinates (also called comoving observers). The scale factor $a(t)$ multiplying the spatial part is the only degree of freedom allowed by the FLRW geometry and determines the size of the universe at every time. As photons travel through the expanding universe, their wavelengths stretch. Therefore, the redshift z of arriving photons today is related to the ratio of the scale factors between observation and emission: $1 + z = a(t_0)/a(t_E)$. The origin of the radial coordinate in the FLRW metric can be placed freely anywhere in accordance with homogeneity. The scale factor can be used to define the Hubble parameter $H = \dot{a}/a$, which gives the typical length and time scale for a FLRW universe. For example, up to

[4]We set the speed of light c equal to one throughout this thesis.

prefactors of order unity, the age of the universe is roughly H^{-1} (Hubble time) and the size of the observable universe approximately cH^{-1} (Hubble radius).

When solving the Einstein equations with the metric ansatz above (1.13) we need to assume that the matter content of the universe is also distributed homogeneously and isotropically. The standard model of cosmology is also termed Lambda(Λ) Cold Dark Matter (ΛCDM) model. The content of the model is the cosmological constant which can be absorbed into the right hand side of the Einstein equations (1.12) as $T_{\mu\nu} = -\Lambda/8\pi G g_{\mu\nu}$, and non-relativistic pressure-less dark matter $T_{\mu\nu} = \rho_{\mathrm{dm}} U_\mu U_\nu$. Visible matter only amounts to a small fraction of the matter content of the universe, while the energy density of radiation is important only in the early universe as it is redshifted away with the expansion.

Solving the Einstein equations for the space-space part we get the Friedmann equation:

$$H^2 = \left(\frac{\dot{a}}{a}\right)^2 = \frac{8\pi G}{3}\rho - \frac{k}{a^2} + \frac{\Lambda}{3}, \tag{1.14}$$

where ρ is the sum of the densities of matter and radiation.[5] Taking the time-time part in the Einstein equations results in the Raychaudhuri equation:

$$\frac{\ddot{a}}{a} = -\frac{4\pi G}{3}(\rho + 3p) + \frac{\Lambda}{3}. \tag{1.15}$$

Note that fluids satisfying the strong energy condition ($\rho + 3p > 0$), such as matter and radiation, lead to the deceleration of the universe ($\ddot{a}/a < 0$), whereas the cosmological constant causes the acceleration. Imposing the conservation of the stress-energy tensor results in the continuity equation:

$$\dot{\rho} + 3H(\rho + p) = 0. \tag{1.16}$$

These three equations are not independent of each other since the conservation of stress-energy tensor is already encoded in the Einstein equations.

[5] assuming that different species are independently conserved

1.1.3 Linear regime and perturbation theory

The exactly isotropic and homogeneous model for the universe is unrealistic. We observe a wealth of structure which cause inhomogeneities in the curvature. The standard approach to describing an inhomogeneous universe is via the cosmological perturbation theory developed in Refs. [18–20]. It assumes the maximally symmetric FLRW spatial sections as the background geometry with added perturbations. The perturbation theory breaks down when the fluctuations become large and the expansion does not converge any more. This happens, for example, at small scales where the density contrast becomes bigger than one. Note that the typical overdensity of bound objects is about 200, where they decouple from the Hubble expansion and start collapsing through gravitational instability. Pedagogical treatment of cosmological perturbation theory can be found in e.g. [21], whereas a more complete treatment can be found in [22, 23].

We can write the perturbed FLRW metric in the Conformal Newtonian Gauge [22] as:

$$ds^2 = a(\eta)^2 \left[(1+2\Psi)d\eta^2 - (1-2\Phi)\left(\frac{dr^2}{1-kr^2} + r^2 \left(d\theta^2 + \sin^2\theta d\phi^2 \right) \right) \right]. \qquad (1.17)$$

We use η, the conformal time here, which is related to the cosmic time as $dt = a(t)d\eta$. The metric in this gauge is simple as it does not contain vector or tensor modes. It is diagonal and has two scalar fields: $\Psi(\eta, \mathbf{x})$ and $\Phi(\eta, \mathbf{x})$. The two fields become the same, $\Phi = \Psi$, in the absence of anisotropic stress, which happens at late times, when CDM and Λ dominate. The metric above resembles the limit of weak gravitational fields in Minkowski space where Φ plays the role of the gravitational potential.

Einstein equations for the perturbed metric and the perturbed stress-energy tensor are solved for the background ($\overline{G}_{\mu\nu} = \kappa \overline{T}_{\mu\nu}$) and the perturbation ($[\delta G]_{\mu\nu} = \kappa [\delta T]_{\mu\nu}$). The conservation of the stress-energy tensor is also imposed $\nabla_\mu T^\mu_{\ \nu} = 0$. The background equations are exactly the same as for the FLRW case. The perturbed density field is $\rho(\eta, \mathbf{x}) = \overline{\rho}(\eta)(1+\delta(\eta, \mathbf{x}))$, where $\delta(\eta, \mathbf{x})$ is the overdensity (or density contrast). Here we limit ourselves to late times, dominated by Λ and pressure-less CDM. The conservation equations give:

$$\delta' + \nabla \cdot \mathbf{v} - 3\Phi' = 0, \tag{1.18}$$

which is the usual continuity equation but with the GR correction $3\Phi'$ due to the perturbation to the expansion rate of space. The derivatives here are with respect to the conformal time and comoving coordinates.

$$\mathbf{v}' + \mathcal{H}\mathbf{v} + \nabla\Phi = 0 \tag{1.19}$$

This is the Euler equation where the velocities are accelerated by the gravitational potential $\nabla\Phi$ while the expansion of underlying space provides the friction term $\mathcal{H}\mathbf{v}$, where $\mathcal{H} = a'/a = aH$ is the Hubble parameter in conformal time.

The Einstein equations result in a Poisson-like equation for the metric perturbation, which can be interpreted in the Newtonian limit of weak fields and slow speeds as the gravitational potential:

$$\nabla^2\Phi = 4\pi G a^2 \overline{\rho}\,(\delta - 3\mathcal{H}v)\,. \tag{1.20}$$

Here v is the scalar mode of the velocity field such that $\mathbf{v} = \nabla v$.

In perturbation theory, the average of any perturbation is zero. For example, the ensemble average of the overdensity $\langle\delta(\eta, \mathbf{x})\rangle$ is zero. The first non-zero moment is the two-point correlation function:

$$\xi(\eta, r) = \langle\delta(\eta, \mathbf{x} + \mathbf{r})\delta(\eta, \mathbf{x})\rangle. \tag{1.21}$$

We assume, according to the cosmological principle, that the perturbations are statistically homogeneous and isotropic. It follows then that the two-point correlation function does not depend on the origin of one of the points $\mathbf{x}$ or on the relative vector $\mathbf{r}$ but only on the relative distance $r = |\mathbf{r}|$. The two-point function describes the probability of finding two objects at distance r in excess of the unclustered or random distribution. Note that the two-point function can only be defined if the background average is well defined or measured.[6]

If the density perturbations are Gaussian distributed, then the two-point correlation function contains all the information about the density field. In fact, observations of

[6]We discuss this in more detail in Chapter 3.

the CMB suggest that the fluctuations in the universe are indeed Gaussian [24]. The Gaussian nature of perturbations is also a common prediction of many models for the origin of structure, which we introduce in Sec. 1.1.3.1. Note that at the first order in perturbation theory, quantities are linearly related to each other, and hence all follow the same type of probability distribution.

A related quantity to the two-point function is its Fourier space representation in terms of the power spectrum:

$$P(k) = \langle|\delta(k)|^2\rangle = \int \xi(r) e^{-i\mathbf{k}\cdot\mathbf{r}} \mathrm{d}^3\mathbf{x} = \int_0^\infty \xi(r) \frac{\sin kr}{kr} 4\pi r^2 \mathrm{d}r. \tag{1.22}$$

Well inside the cosmological horizon ($\ll H^{-1}$) the equations for the evolution of linear perturbations simplify to Newtonian result:

$$\delta' + \nabla \cdot \mathbf{v} = 0. \tag{1.23}$$

Since modes in the linear theory evolve independently, we can express δ' in terms of the growth factor $f = \frac{\partial \log \delta(\eta,\mathbf{x})}{\partial \log a(\eta)} = \frac{\delta'}{\mathcal{H}\delta}$ as follows:

$$\mathcal{H} f \delta + \nabla \cdot \mathbf{v} = 0. \tag{1.24}$$

Provided that the vorticity of the velocity field vanishes, $\nabla \times \mathbf{v} = 0$, the equation above can be rewritten as:

$$\mathbf{v}(\mathbf{r}, t) = \frac{H(t) f}{4\pi} \int \frac{\delta(\mathbf{r}')(\mathbf{r} - \mathbf{r}')}{|\mathbf{r} - \mathbf{r}'|^3} \, \mathrm{d}\mathbf{r}'^3, \tag{1.25}$$

where we used the usual cosmic time t and actual distance $\mathbf{r} = a(t)\mathbf{x}$. Neglecting the vorticity can be justified by taking the curl of Eq.(1.19):

$$\frac{\nabla \times \mathbf{v}'}{\nabla \times \mathbf{v}} = -\mathcal{H} = -\frac{a'}{a}. \tag{1.26}$$

Hence, the curl scales as $\nabla \times \mathbf{v} \propto 1/a$ and vanishes as the universe grows.

The real universe exhibits non-linear fluctuations at small scales. Therefore, to make contact with predictions of the linear perturbation theory, we need to smooth or average out the fluctuations over some large scale R where the theory applies. This can be achieved by convolution with a window function[7], e.g. $\mathbf{V} = \mathbf{v} * W(\mathbf{r}; R)$. The average of

[7]Typically Gaussian or spherical top-hat.

the velocity field in a region defined by some window function, corresponds to the bulk flow of matter within the window. The typical size of the bulk flow can be estimated by considering the variance of the field:

$$\sigma_V^2 = \langle \mathbf{V} \cdot \mathbf{V} \rangle = \iint W(\mathbf{r}'; R) W(\mathbf{r}; R) \langle \mathbf{v}(\mathbf{r}') \cdot \mathbf{v}(\mathbf{r}) \rangle \mathrm{d}r'^3 \mathrm{d}r^3 = \frac{1}{2\pi^3} \int P_{\mathbf{vv}}(k) \tilde{W}^2(k; R) \mathrm{d}k^3, \tag{1.27}$$

where $P_{\mathbf{vv}}(k)$ is the velocity power spectrum and $\tilde{W}(k; R)$ is the Fourier transform of the window function. Taking the Fourier transform of Eq.(1.24) we obtain $\mathcal{H} f \delta_{\mathbf{k}} + i\mathbf{k} \cdot \mathbf{v}_{\mathbf{k}} = 0$. Hence, we can write the velocity power spectrum in terms of the matter one and obtain:

$$\sigma_V^2 = \frac{(Hf)^2}{2\pi^3} \int \frac{P_{\delta\delta}(k)}{k^2} \tilde{W}^2(k; R) \mathrm{d}k^3. \tag{1.28}$$

1.1.3.1 Origin of perturbations and the primordial power spectrum

Having discussed the evolution of perturbations, let us turn to how they are produced. The most successful and widely accepted paradigm for the origin of structure is inflation. It refers to (almost) exponential expansion of space during the very early stages of the universe, before the early radiation dominated phase of the standard Big Bang cosmology begins.

Such a period of expansion was proposed in Ref. [25, 26] and soon after used as a solution to several of the puzzles of the non-inflationary Big Bang cosmology [27, 28].

The primary issue is the horizon problem. Assuming conventional Big Bang cosmology, points on the Cosmic Microwave Background sky with angular separation of more than two degrees would have never been in causal contact (assuming the forward light cones from the Big Bang can be calculated back to $t = 0$). This makes the observed uniformity of the CMB (about 1 part in 10^5) puzzling.

Another problem is the flatness of the universe, which is measured at the present epoch to be flat (to better than one part in 100) [29]. However, in the standard cosmology, the zero curvature case is unstable under evolution. That is, the departure from flatness grows with time. This means that the early universe must have been even flatter which poses a serious fine tuning problem.

In the hot early stages of the universe particle energies may be above the energy scale ($\sim 10^{16}$ GeV) of Grand Unified Theories (GUT).[8] As the temperature drops, GUTs typically predict production of topological defects (e.g. monopoles, strings, domain walls) during a phase transition associated with spontaneous symmetry breaking. Such defects have not been observed, requiring a way to explain their absence.

All the three problems mentioned above can be solved by a period of accelerated expansion at very early times. For example, this allows the patches of the CMB sky to come into causal contact, it dilutes away the unobserved monopoles and flattens out any initial curvature.

In addition to solving the problems of the standard Big Bang cosmology, inflation also provides a way to generate structure in the universe. Whatever is driving the inflation (e.g. a scalar field) possesses quantum fluctuations which cause perturbations in space-time [31]. Those perturbations are then inflated to scales beyond the horizon where they do not evolve[9]. Later, when the accelerated expansion stops, those perturbations enter the horizon and act as seeds for the present day structure through gravitational collapse. For more detailed and pedagogical treatment see e.g. [33].

We can understand the nature of fluctuations generated during inflation via a simple argument [34]. In the approximation where the inflationary phase is exactly exponential, $a(t) \propto \exp(Ht)$, the universe possesses a time translation symmetry. Formulated otherwise, the only physical length scale H^{-1} is constant with time. Therefore, at two different times, such a universe cannot be distinguished. Small perturbations in this background respect this property. It then follows that the metric perturbations Φ have to be the same for every length scale as it exits the horizon. If this were not the case, one could use the changing value of the fluctuation at the horizon scale as a 'clock' to distinguish future from past.

The metric perturbation is related to the density perturbation. In conformal Newtonian gauge they are related via the Poisson equation:

[8] A calculation of the scattering rate in the QCD plasma at high temperatures shows, however, that equilibrium is achieved only up to 3×10^{14} GeV [30]

[9] This is true for the single-field inflation that produces adiabatic primordial density perturbations (detailed proof in e.g. [32]) but can be violated in models with multiple fields.

$$\nabla^2\Phi \propto \delta. \tag{1.29}$$

Therefore, on average $\langle\Phi^2\rangle \sim \lambda^4\langle\delta^2\rangle$ for some length scale λ. Requiring the metric perturbation to be constant for all length scales forces the two-point correlation function to behave as $\langle\delta^2\rangle \sim 1/\lambda^4$. Therefore the primordial power spectrum arising from such fluctuations is obtained via Eq.(1.22) by Fourier transforming:

$$P(k) \propto k. \tag{1.30}$$

This is known as the scale-invariant Harrison-Zeldovich power spectrum [35, 36]. In fact, the universe evolves and H^{-1} changes very slowly during inflation – this can give the spectrum of fluctuations a small 'tilt' away from scale-invariance [31]. The power spectrum of density fluctuations at later times, in particular at the present epoch, can be obtained via the perturbation theory describing the evolution of initial scale-invariant perturbations.

1.1.3.2 Slow-roll scalar field

The most common 'toy' models of inflation are based on a single scalar field, the 'inflaton', which evolves slowly ('slow-rolls') along a nearly flat potential to its minimum, during which it sources a quasi-exponential growth of the cosmological scale factor. Hence, in the slow-roll regime, the spatial and time derivatives are negligible compared to the approximately constant vacuum energy sourced by the potential.

The background dynamics of the homogeneous scalar field in the FLRW universe is governed by the continuity and Friedmann equations:[10]

$$\ddot{\phi} + 3H\dot{\phi} + \partial_\phi V = 0, \tag{1.31}$$

$$H^2 = \frac{1}{3M_{\rm Pl}^2}\left(\frac{1}{2}\dot{\phi}^2 + V(\phi)\right). \tag{1.32}$$

It follows then that the accelerated expansion of the universe ($\ddot{a}/a > 0$) is achieved when $\dot{\phi}^2 < V(\phi)$. That is, the potential energy of the scalar field dominates over the

[10]We use the reduced Planck mass $M_{\rm Pl}^2 = 1/8\pi G_{\rm N}$ in the units where $\hbar = c = 1$.

kinetic energy. If the potential energy is much bigger, $\dot{\phi}^2 \ll V(\phi)$, then the Hubble parameter is roughly constant, resulting in quasi-exponential expansion.

Sustaining the accelerated expansion for long enough also requires the second derivative of the field $\ddot{\phi}$ to be small. These slow-roll conditions can be encoded in the smallness of two potential dependent slow-roll parameters:

$$\begin{aligned} \epsilon_V(\phi) &\equiv \frac{M_{\rm Pl}^2}{2}\left(\frac{\partial_\phi V}{V}\right)^2, \\ \eta_V(\phi) &\equiv M_{\rm Pl}^2\left(\frac{\partial_\phi^2 V}{V}\right). \end{aligned} \tag{1.33}$$

Inflation proceeds when $\epsilon_V \ll 1$ and $|\eta_V| \ll 1$, and roughly ends when $\epsilon_V(\phi_{\rm end}) \approx 1$. During the expansion, the universe grows by a number of e-folds:

$$N(\phi) \equiv \log\left(\frac{a_{\rm end}}{a}\right) = \int_t^{t_{\rm end}} H{\rm d}t \approx \int_{\phi_{\rm end}}^{\phi} \frac{1}{\sqrt{2\epsilon_V}}\frac{{\rm d}\phi}{M_{\rm Pl}}. \tag{1.34}$$

The Cosmic Microwave Background fluctuations are created about 40 to 60 e-folds before the end of inflation [37]. The precise value depends on the details of reheating, post-inflationary thermal history and the energy scale of inflation. The integral constraint $N(\phi_{\rm CMB}) \approx 40 - 60$ provides us with the field value when the CMB fluctuations are created. This in turn can be used to find the main observables related to the power spectrum of the fluctuations on the sky.

Because the inflationary Hubble parameter is not exactly constant, the primordial power spectrum deviates from the scale-invariant Harrison-Zeldovich spectrum. Assuming it has a power law form, this gets encoded in the spectral index $n_{\rm s}$:

$$P_\delta(k) \sim k^{n_{\rm s}}. \tag{1.35}$$

Conventionally, the primordial power spectrum is expressed in terms of the curvature perturbation:

$$P_{\mathcal{R}}(k) \approx \frac{2\pi^2}{k^3} A_{\rm s}\left(\frac{k}{k_{\rm pivot}}\right)^{n_{\rm s}-1}, \tag{1.36}$$

where for a single scalar field the spectral index $n_{\rm s}$ and the amplitude $A_{\rm s}$ can be written in terms of the slow-roll parameters:

$$n_s - 1 \approx 2\eta_V - 6\epsilon_V,$$
$$A_s \approx \frac{V}{24\pi^2 M_{\rm Pl}^4 \epsilon_V}. \tag{1.37}$$

Another observable is the ratio r of the amplitudes of tensor and scalar modes of perturbations created during inflation. It can be written as $r \approx 16\epsilon_V$ in terms of the potential. All the three observables above are evaluated at $\phi_{\rm CMB}$, the value of the field when the CMB perturbations are created. During the slow-roll phase the scalar field is nearly free. Therefore, the quantum mechanical fluctuations it produces are very close to Gaussian.

1.1.4 Non-linear regime and N-Body simulations

The universe is modelled as initially in a very homogeneous and isotropic state with small perturbations seeded by inflation. Gravitational collapse results in the growth of structure. Eventually the initial perturbations become too large for the linear theory to be applicable. Below the horizon scale the Newtonian approximation works well[11] with corrections arising only on super-horizon scales (calculated within perturbation theory in e.g. [39,40]). Therefore, the non-linear regime can be accessed by assuming an expanding cosmological background with action-at-a-distance Newtonian theory of gravity.

Here we briefly outline the basics of cosmological N-Body simulations that enable us to study the growth of structure even in the non-linear regime. The matter content is modelled as collisionless massive particles (corresponding to CDM) with Newtonian gravity acting between them. Baryons are usually neglected as modelling and simulating their dissipative effects is computationally much more intensive.[12] The initial conditions for simulations are set up in the linear regime where the positions and velocities of particles can be calculated theoretically within perturbation theory.

Newton's second law of motion for particle i in an expanding universe with only the gravitational force acting can be written in terms of comoving coordinate $\mathbf{x}$ and cosmic time t as:

[11] Specifically, Newtonian gravity is a very good approximation to the GR field equations when the fields are non-relativistic and the modes are sufficiently below the horizon scale (see discussion in e.g. [38]).

[12] This means that the cosmological hydrodynamical simulations are considerably smaller compared to the CDM only simulations.

$$\ddot{\mathbf{x}}_i + 2H(t)\dot{\mathbf{x}}_i = -\frac{1}{a^2}\nabla_x \phi_i \tag{1.38}$$

The expansion of the background provides the friction term slowing down peculiar motions in comoving coordinates. The gradient of the potential $-\frac{1}{a^2}\nabla_x\phi_i$ is just the usual Newtonian force of gravity acting on particle i:

$$\mathbf{F_i} = \sum_{i \neq j} \frac{G m_i m_j (\mathbf{x}_i - \mathbf{x}_j)}{a^2 \left(|\mathbf{x}_i - \mathbf{x}_j|^2 + \epsilon^2\right)^{3/2}} \tag{1.39}$$

Here we include the softening length ϵ [41] which is a way to suppress the gravitational force at small distances. The unmodified Newtonian force law would lead to singularities in the force and consequently to errors in numerical integration such as unbounded velocities of particles. The non-regularised force law would also cause formation of unphysical binaries which would be inconsistent with the fact that DM is simulated to correspond to a collisionless fluid. There are varieties of more optimal softening kernels, see e.g. [42], all with some characteristic length scale ϵ.

A simple integration of the equations of motion for N_p particles would result in computational complexity of $\mathcal{O}(N_\mathrm{p}^2)$ and long computational times as for each of the N_p particles $(N_\mathrm{p}-1)/2$ forces have to be calculated. Hence, approximation methods to calculate the force were developed to optimize simulations. Two popular codes, the Particle Mesh algorithm and the Tree algorithm both reduce the computational complexity. The Particle Mesh method uses a grid and Fast Fourier Transform to solve the Newtonian Poisson equation for the gravitational potential and then interpolates to get the force at the particle position, which reduces the complexity to $\mathcal{O}(N_\mathrm{G} \log N_\mathrm{G})$ where N_G is the grid size. Tree algorithms set up the information about the density field in a hierarchical tree with each level corresponding to a different degree of coarse-graining. Force from particles at greater distances can be approximated with a force from a coarse-grained cell containing those particles. This lowers the number of operations and leads to the reduced computational complexity of $\mathcal{O}(N_\mathrm{p} \log N_\mathrm{p})$.

At this stage an N-body simulation only contains the position of particles and their peculiar velocities. Structures corresponding to the gravitationally bound objects in the universe are found with algorithms called halo finders (for a review of many of them

see [43]). Generally they can be separated into two categories: configuration-space based halo finders and (newer) phase-space based halo finders. Configuration-space halo finders only use position information to group particles together. For example, Friend of Friend (FoF) algorithms connect all particles that are within some distance of each other while Spherical Overdensity (SO) codes connect particles corresponding to certain overdensity within a spherical region. Phase-space halo finders use particle velocities in addition to their position. The advantage of this approach is that structures undergoing mergers can be identified as they are well separated in phase-space contrary to position space only.

1.1.5 N-Body simulation used in this thesis

The work in Chapters 3, 4, and 5 relies on N-Body simulation data which we describe below.

We use one of the largest N-Body simulations to date – the Dark Sky (DS) Simulation [44]. It is a dark matter only ΛCDM simulation using $10240^3 \approx 10^{12}$ particles in a volume of $(8000\,h^{-1}\mathrm{Mpc})^3$, with the following cosmological parameters: $(\Omega_\mathrm{m} = 0.295, \Omega_\mathrm{b} = 0.0468, \Omega_\Lambda = 0.705, n_\mathrm{s} = 0.969, h = 0.688, \sigma_8 = 0.835)$. The Newtonian forces between particles of mass $M_\mathrm{par} \sim 3.9 \times 10^{10} M_\odot/h$ are calculated using a tree method and the halo catalogue is obtained using ROCKSTAR [45], a phase-space based halo finder. We study the output of the simulation at $z = 0$. To make computation more efficient, we reduce the number of halos by imposing a mass cut ($M_\mathrm{vir} > 10^{12} M_\odot/h$). This includes clusters of galaxies as well as massive galaxies, whereas the lightest galaxies are neglected. The resulting catalogue contains 2.3×10^9 DM halos with a mean number density of 4.6×10^{-3} halos/$(h^{-1}\mathrm{Mpc})^3$. Equivalently, the mean halo-halo distance is approximately $6\,h^{-1}$Mpc.

1.2 Problems of the standard model and motivation

It is widely believed that the field of cosmology is currently entering the 'precision' stage [46]. However, in this section we list some of the shortcomings of the standard ΛCDM model which need to be addressed before the model can be reliably considered as a basis for 'precision cosmology'.

Observations of distant supernovae [13,14] are the key to requiring that the universe, as modelled by a FLRW background, is currently accelerating, implying that Λ is currently non-zero. However, the evidence for acceleration, after careful analysis, is still marginal [47] [13]. Introducing other datasets (e.g. Baryonic Acoustic Observations and CMB observations) strengthens the claim for acceleration. Acceleration is achieved by a component of the stress-energy tensor that includes a fluid with negative pressure. The simplest contribution with such a property is the cosmological constant Λ as well as the zero point fluctuations of the vacuum. They combine together to provide the energy density that effectively drives acceleration. A naïve theoretical estimate of the vacuum energy implies a number about 60 orders of magnitude bigger than the observationally inferred value[14], requiring huge cancellation between the geometrical Λ and the vacuum energy from the matter sector. This is the cosmological constant problem (for reviews see e.g. [48–50]). Another issue associated with the inferred value of Λ is the coincidence problem. The energy density associated with the cosmological constant is roughly equal to the energy density of matter. This means that we live in a very special point in time, just when Λ starts to dominate and the universe starts to accelerate, which requires very special initial condition in the early universe.

In Sec. 1.1.1 we saw that GR is a non-linear theory. Einstein equations are a set of second order, coupled, and non-linear partial differential equations. As a result, the inhomogeneities on small scales influence the dynamics of large scales - the effect called backreaction. This is in contrast with the linear perturbation theory where the background and all modes evolve independently. N-Body simulations, despite modelling non-linear evolution, cannot capture the backreaction effects as the dynamics of the background is determined independently using the FLRW solution in GR. Some studies of backreaction suggested that the inhomogeneities can mimic some of the acceleration of the universe (e.g. in [51–54]). Related to backreaction is the issue of averaging a lumpy universe to arrive to a more homogeneous state we can describe in perturbation theory as well as the issue of fitting a lumpy universe to our idealised model. For a review of these problems see e.g. [55]. The precise size of backreaction effects has still not been

[13] This is true when supernovae data is analysed without introducing extra unknown sources of error by hand and artificially adjusting those to achieve fits of $\chi^2 = 1$ per degree of freedom.

[14] More detailed calculations can be found in Refs. [48, 49]

determined exactly. Arguments for significant effects [56, 57] are countered by claims to the contrary [58, 59]. Recent works employing the tools of numerical relativity [60, 61] promise to shed more light on this issue once fully relativistic cosmological simulations become available.

The universe is modelled as filled uniformly by an ideal fluid. However, the structure in the universe appears to be mostly in highly localised overdensities (e.g. galaxies and galaxy clusters) with the rest of the space being empty. Therefore, it needs to be verified whether what is essentially a collection of point particles can be faithfully described as a fluid (see [62] for detailed discussion). It has been shown, within the framework of Newtonian cosmology, that point particles on average behave the same as a fluid [62]. However, within GR the fluid approximation has been verified only in systems with regularly arranged particles [63, 64] and not for realistic distributions.

The universe described by the standard model has a non-zero Ricci tensor sourced by the stress-energy tensor via the Einstein equations (1.12). The observable universe is mostly empty and so the Ricci tensor is zero almost everywhere. While the overall dynamics of both the model and the real universe might be the same, the optical properties need not be so. Refs. [65, 66] show that, in the context of Swiss-cheese models of the universe[15], the cosmological parameters deduced shift significantly from their true values due to optical effects, depending on the value of the cosmological constant.[16] The shift is much smaller (below 1%) when calculated within the context of Newtonian N-Body simulations [67] but nevertheless becomes relevant in the era of 'precision cosmology'.

Inflation is a successful paradigm in explaining the origin of structure and in ameliorating the puzzles of the non-inflationary Big Bang cosmology. However, there are hundreds of different models [68, 69] for the inflationary period – all roughly consistent with the observations. Even limiting the models to a single scalar field, there are dozens [70] of potentials suitable for driving inflation. They are either phenomenological or inspired by various high energy (UV-complete) theories. We address this arbitrariness in Chapter 2. We propose a different approach to deriving a scalar field theory suitable

[15]Swiss-cheese models cut holes in the FLRW space-time and replace them with spherically symmetric solutions corresponding to the removed mass. This way the overall dynamics of the Swiss-cheese model is exactly as the original FRLW but with empty regions.

[16]The cosmological constant suppresses the growth of structure and hence the effects of inhomogeneities are smaller when the cosmological constant is bigger.

for the slow-roll inflation. We argue that inflation can be understood as a generic, non-perturbative consequence of the exact renormalisation group (ERG).

The three dimensional distribution of matter observed on the sky exhibits a complex structure of nodes, filaments, walls, and voids. A similar "Cosmic Web" structure appears in N-body DM simulations. This intricate fractal-like distribution cannot be deduced from the matter power spectrum as it does not contain the phase information needed for coherent structures such as filaments and walls [71]. The fractal-like nature has been characterised in terms of the 'counts-in-spheres' dimension that measures how the number of galaxies scales with the radii of spheres containing those galaxies. However, this fractal dimension contains the same information as the two-point correlation function (given certain conditions), as we discuss in Chapter 3. There we propose an alternative method to characterise the inhomogeneity in cosmology based on the ideas of diffusion and random walks.

In the standard model of cosmology, observers that are not moving with respect to the background geometry are called the fundamental observers. The natural question arises whether there are structures in the universe that can be identified with such observers. Potential candidates are galaxy clusters since they are the largest gravitationally bound structures. Naïvely they would be expected to follow the Hubble flow and move *away* from each other. The discovery of many merging clusters thus poses an issue for the standard model where such mergers are expected to be rare. We address this problem in Chapter 4.

In Chapter 5 we focus on the locally measured Hubble parameter. It was observed that the Hubble parameter measured in the frame of the Local Group of galaxies converges quicker to its background value compared to when it is measured in the CMB frame. This seems to be at odds with the ΛCDM expectations, since all quantities have minimum variation in the CMB frame on average. We explore whether the observation is consistent with the standard model and in doing so we touch upon the related issues of bulk flows and locally measured Hubble parameter. Both have been measured to be higher than the ΛCDM prediction and potentially inconsistent with the model. The higher Hubble parameter has motivated purely statistical studies in terms of linear theory [72] and N-Body simulations [73] as well as studies of biases coming from relativistic

effects [74], optical effects [67], and the density of the local universe [75]. Anomalously high bulk flows persisting to large scales, which are discussed in Sec. 5.1 in more detail, might require a different theoretical model of the universe (e.g. tilted universe [76]) or even a rethink of what defines the cosmic rest frame [77].

Chapter 2: Inflation from Exact Renormalisation Group

2.1 Introduction

A brief overview of the inflationary paradigm and its concrete realisation in the form of a slowly rolling scalar field has been given in Sec. 1.1.3.1.

In this chapter we propose a different approach to deriving a scalar field theory suitable for slow-roll inflation. Inspired by the multitude of different models of inflation, either phenomenological or embedded in various UV complete theories, we argue that inflation can be understood as a generic, non-perturbative consequence of the exact renormalisation group (ERG). Renormalisation group is a systematic way of studying the changes in physical systems at different energy/distance scales, in particular the changes from high energies (UV) to low energies (IR). Transformations in the action as the energy scale changes can be encoded in the exact renormalisation group equation (ERGE) [78]. For reviews and derivation of ERGE see e.g. [79–81].

Our approach to deriving inflationary potentials from ERGE is largely insensitive to the details of the UV physics since we assume that the scalar mode of the UV theory has suppressed couplings to other fields. We take the UV energy scale to be somewhere below the Planck scale, $M_{\rm UV} < M_{\rm Pl}$. This assumption allows us to ignore quantum gravity effects.

To have a valid potential for the description of inflation, we must ensure that the effective theory is valid below some scale M, where M is roughly on the order of the inverse Hubble radius at the start of inflation. This is the IR scale of our original theory [1]. Thus, $1/M^4$ will be approximately the volume of the patch of space-time of the resulting effective theory, which we assume resides within the Hubble radius. We will assume that the UV theory at $M_{\rm UV} >> M$ contains a scalar mode ϕ that couples very weakly to other fields. Hence, during the RG flow from $M_{\rm UV}$ to M, the corrections to the effective potential of such a scalar from the couplings to other UV fields would remain small. In

[1] To clarify, we follow the RG flow of the UV theory from $M_{\rm UV}$ to the IR scale M of the RG flow with the effective potential obtained valid below this energy M

the RG analysis, ϕ can therefore be treated independently.

The second assumption will be the validity of the mean-field approximation (MFA) near the scale M.[2] That is, we will treat the constant mode of the theory separately when we do our IR analysis. An argument for the plausibility of this assumption is given in [85]. The assumption of the validity of MFA may at first seem peculiar, but we note that for inflation to begin, the inflaton field has to be sufficiently smooth to overcome the gradient energy preventing the exponential expansion. Indeed, the MFA is a common feature of most inflationary scenarios, where the field is assumed constant at the scale where inflation begins [86] and the dynamics is mostly driven by the potential.

Lastly, we will also ignore effects of gravity in the ERG. We start at a scale M_{UV} somewhere below the Planck scale, so that quantum gravity effects can be ignored. For the most part of the RG flow, we are at an energy scale where the vacuum energy is negligible in comparison, and we can work in Minkowski space where gravitational effects are unimportant. We end our flow at the scale at which inflation begins. Flows beyond this point would require us to take gravitational effects into account and work in de Sitter space [82–84].

After introducing the ERG equation relevant for our setup we will show that the MFA of the ERG equation gives rise to a one-dimensional Schrödinger-type equation for the resulting effective theory, which can be solved exactly. This is similar to the stochastic approach of [87, 88] as well as the study of renormalisation group in quantum mechanics [89]. In essence, we will solve a simple quantum mechanical problem in which the resulting "wave-function" will correspond to the effective theory, or potential, for the constant mode. Because in QFT the theories need not be normalisable functions of the field variable, we will only insist that the resulting potential is bounded from below. What is meant by normalisable and un-normalisable solutions will be explained below. Our analysis will then result in non-perturbative IR effective potentials with shapes suitable for inflation. It will give predictions that are consistent with current observations.

We note that spectral methods have been applied in the context of ERG before, see

[2]For other recent implementations of the ERG within the MFA, in particular in de Sitter space, see [82–84].

e.g. [90–94] and references therein for more details. Additionally, the observation that renormalisation group dynamics can produce experimentally viable inflation scenarios has been noted in the literature earlier [95, 96]. The exact RG has been applied in the context of inflation, see e.g. [97–99].

2.2 Exact renormalisation group analysis

2.2.1 The ERG equation

Let us begin by considering a UV quantum field theory in the early universe that contains some set of fields at the UV scale $M_{\rm UV} < M_{\rm Pl}$, including a scalar mode ϕ. By Φ, we collectively denotes the remaining UV fields. As the theory runs between M_{UV} and the IR scale M, we assume that ϕ and Φ interact very weakly so that the IR theory for energies less than M takes the form,

$$Z = \int_M \mathcal{D}\phi\, e^{-S_\phi[\phi]} \int_M \mathcal{D}\Phi\, e^{-S_\Phi[\Phi]}. \tag{2.1}$$

We can thus focus only on the decoupled renormalisation group flow for the scalar ϕ by following the procedure of the exact Wilsonian renormalisation group [78]. The ERG equation for the decoupled scalar mode takes the form

$$\partial_t S_\phi = \int_p \Big(\alpha(t) + 2p^2\Big)\left[\frac{\delta^2 S_\phi}{\delta\phi_p \delta\phi_{-p}} - \frac{\delta S_\phi}{\delta\phi_p}\frac{\delta S_\phi}{\delta\phi_{-p}} + \phi_p \frac{\delta S_\phi}{\delta\phi_p}\right], \tag{2.2}$$

where $\alpha(t)$ depends on the choice of the cut-off and $t = -\log(M/M_{\rm UV})$ denotes the RG time – roughly an inverse of the cut-off scale M.[3] The equation above is dimensionless and so from an inflationary standpoint it is common and convenient to express the field ϕ and energies in units of $M_{\rm Pl}$[4], rather than $M_{\rm UV}$, which would mean a redefinition of the field.

The ERG equation (2.2) is a non-linear equation. However, if we instead consider the functional

$$\Psi\left[\phi\right] = e^{-S_\phi[\phi]}, \tag{2.3}$$

[3]Since we are only interested in solving the theory in the IR, we do not include the rescaling of the theory back to the original UV scale – blocking from $M_{\rm UV}$ to M suffices.

[4]Throughout this chapter, we use the reduced Planck mass, $M_{\rm Pl} = 2.44 \times 10^{18}\,\text{GeV}$.

then Eq. (2.2) becomes a linear Schrödinger-type equation,

$$\partial_t \Psi\left[t,\phi\right] = \hat{\mathcal{H}}\Psi\left[t,\phi\right], \tag{2.4}$$

with a Hamiltonian operator in position space,

$$\hat{\mathcal{H}} = \int d^4x \left(\alpha(t) - 2\partial^2\right)\left(\frac{\delta^2}{\delta\phi_x^2} + \phi_x\frac{\delta}{\delta\phi_x}\right). \tag{2.5}$$

This is the usual form of the Wilsonian ERG equation, written in terms of Ψ. Similar equations have been derived in the literature, see e.g. [100, 101]. Note that one common feature of these equations is that the Hamiltonian has a kinetic part $\delta^2/\delta\phi^2$, together with a divergence term $\phi\,\delta/\delta\phi$.

2.2.2 Solution of the RG flow

We can now use the MFA to solve the ERG equation (2.4) for the patch of the universe of the size of $1/M^4$, i.e. in the IR regime of the theory. In the UV, we wish to remain as general as possible, so we do not specify the details of the theory. Let us then write the Euclidean partition function (2.1) with its initial theory specified in the UV as

$$Z = \int \mathcal{D}\phi\,\Psi_{UV}\left[t,\phi\right]. \tag{2.6}$$

In the MFA, an eigenmode of the Hamiltonian $\hat{\mathcal{H}}$ evolves under the ERG equation (2.4) as

$$\Psi(t,x) = e^{Et}\Psi(x), \tag{2.7}$$

where E are the eigenvalues of the RG time-independent equation

$$\hat{\mathcal{H}}\Psi = E\Psi. \tag{2.8}$$

Here we explicitly write the dimensionless field as $\hat{x} \equiv \phi/M_{\rm Pl}$. Note that we are using $\Psi \equiv \Psi(x)$. In analogy with quantum mechanics, we assume that $\Psi_{UV}(t,x)$ can be expanded as

$$\Psi_{UV}(t,x) = \sum_i \gamma_i e^{E_i t}\Psi_i(x), \tag{2.9}$$

where Ψ_i have eigenvalues E_i. In the IR, where $t \to \infty$, the dominant contribution will therefore come from the highest eigenvalue solution, Ψ_i with $\max[E_i]$, that has a non-trivial overlap with the UV theory. The contribution of other eigenvalue solutions will decay exponentially fast with RG time so we expect the highest eigenvalue solution to dominate even with little RG flow. Note that in Eq. (2.9), a functional integral over Ψ_i should be used instead of the sum when E_i are a continuous set.

It is convenient to introduce a new functional ψ so that

$$\Psi \equiv e^{-\hat{x}^2/4}\psi. \tag{2.10}$$

The ERG eigenvalue equation in the MFA then becomes

$$\hat{H}\psi = E\psi. \tag{2.11}$$

We also let $\hat{p} \equiv -i\partial_{\hat{x}}$, which gives the Hamiltonian operator $\hat{H}$:

$$\hat{H} = -\left(\hat{p}^2 + \frac{\hat{x}^2}{4} + \frac{1}{2}\right), \tag{2.12}$$

where we have set $\alpha = 1$ without loss of generality and derivatives ∂^2 with respect to coordinates to zero as we are working in the MFA. It is important to note that the solutions to (2.8) and (2.11), i.e. Ψ_i and ψ_i, respectively, have the same eigenvalues, E_i. In the MFA, the two Hamiltonians are related by

$$\hat{\mathcal{H}} = e^{-x^2/4}\hat{H}e^{x^2/4} = \partial_x^2 + x\partial_x\,. \tag{2.13}$$

The form of $\hat{H}$ in Eq. (2.12) is highly reminiscent of the quantum harmonic oscillator in imaginary (Euclidean) time. Indeed, by defining the ladder operators

$$\hat{a} = \frac{1}{2}\hat{x} + i\hat{p}, \tag{2.14}$$

$$\hat{a}^* = \frac{1}{2}\hat{x} - i\hat{p}, \tag{2.15}$$

the Hamiltonian takes the form

$$\hat{H} = -(\hat{a}^*\hat{a} + 1). \tag{2.16}$$

Eq. (2.16), which describes the renormalisation group evolution of the effective action

thus only differs from the usual harmonic oscillator by an overall minus sign and the additive factor of 1 in place of 1/2.

For modes of ψ which tend to zero as $x \to \pm\infty$, the operator a^* is the adjoint of a, $a^* = a^\dagger$. To see this, let ψ_i and ψ_j be modes that tend to zero at infinity and consider the inner product:

$$(\hat{a}\psi_i, \psi_j) = \int dx\, (\hat{a}\psi_i)\psi_j^* = \int dx\, \psi_i(\hat{a}^*\psi_j)^* = (\psi_i, \hat{a}^\dagger\psi_j), \tag{2.17}$$

where we have performed an integration by parts. $\hat{H}$ is negative definite for such modes, and the highest eigenvalue is the "vacuum energy",

$$E_0 \equiv E = -1, \tag{2.18}$$

which corresponds to the vacuum of the theory, ψ_0,

$$\hat{a}\,\psi_0(x) = \left(\frac{1}{2}x + \partial_x\right)\psi_0(x) = 0. \tag{2.19}$$

The corresponding re-scaled "original" theory reads

$$\begin{aligned}\Psi_0(x) &= C_0 e^{-x^2/4}\psi_0(x) \\ &= C_0 e^{-x^2/2},\end{aligned} \tag{2.20}$$

which precisely corresponds to the potential of a free theory. Besides the free theory, there exists a mode, $\tilde{\psi}_0$, with the same eigenvalue (2.18),

$$\tilde{\psi}_0(x) = D_0 e^{-x^2/4}\,\mathrm{erfi}\left(\frac{x}{\sqrt{2}}\right), \tag{2.21}$$

$$\tilde{\Psi}_0(x) = D_0 e^{-x^2/4}\tilde{\psi}_0(x) = D_0 e^{-x^2/2}\,\mathrm{erfi}\left(\frac{x}{\sqrt{2}}\right), \tag{2.22}$$

were $\mathrm{erfi}(x)$ denotes the imaginary error function. Note that while $\tilde{\psi}_0(x)$ diverges as $x \to \pm\infty$, as expected for a un-normalisable mode of the harmonic oscillator, the re-scaled wave-function, $\tilde{\Psi}_0$, exhibits the correct behaviour and tends to zero at infinity. $\tilde{\Psi}_0$ leads to a bounded potential, as

$$S_\phi\,[\phi] = -\log\tilde{\Psi}_0 = \frac{\tilde{V}_0(\phi)}{M^4}, \tag{2.23}$$

where

$$\tilde{V}_0(\phi) = M^4 \left[\log(D_0) + \frac{1}{2}x^2 - \log\left[\text{erfi}\left(\frac{x}{\sqrt{2}} \right) \right] \right]. \tag{2.24}$$

In order to avoid considering theories of arbitrarily high eigenvalues, one reasonable assumption is that the UV theory has *no* overlap with modes Ψ_i of which the eigenvalues would be higher than the "vacuum" energy E_0, cf. Eq. (2.18). In physical terms, this means that we assume that the IR limit of Ψ_{UV} is connected to the free theory – the state Ψ_0.

In the absence of such a restriction, it is clear that the eigenstates of (2.11), and thus also Ψ, could have arbitrarily high eigenvalues. However, we want our dominant IR theory, denoted temporarily by $\Psi = \Psi_E$, with some eigenvalue E, to tend to zero as $x \to \pm\infty$, as required by a stability condition that potentials need to be bounded from below. The eigenvalue equation (2.8) then reads

$$\begin{aligned} \hat{\mathcal{H}}\Psi_E &= E\Psi_E \\ &= \partial_x^2 \Psi_E + x\partial_x \Psi_E \,. \end{aligned} \tag{2.25}$$

If we multiply this equation by Ψ_E and integrate over x, we get after integration by part,

$$E\Psi_E = -\int_x (\partial_x \Psi_E)^2 - \frac{1}{2}\int_x \Psi_E^2. \tag{2.26}$$

The main point is that integration by parts can only be performed for Ψ_E that tend to zero at infinity. Since the integrands on the right-hand-side of (2.26) are negative-definite, it follows that theories with bounded potentials must have $E < 0$.

In the remainder of this chapter, we will focus on two classes of stable effective potentials: the IR effective theories with *discrete* and *continuous* spectra of $E_i < 0$. In the deep IR limit where $t \to \infty$, the existence of a discrete spectrum with integral eigenvalues implies that the state with the highest eigenvalue, $E_0 = -1$, will dominate the first class of theories. In the continuous case, theories with E_i close to 0 will dominate.

We can now restate the above results in the following way: By assuming that Ψ_{UV} has a non-zero overlap only with the states of integral eigenvalues $E = -n$ for $n \in \mathbb{N}$, the IR limit of the theory takes the generic form

$$\Psi_0(x) = e^{-\frac{1}{2}x^2} \left[C_0 + D_0 \,\text{erfi}\left(\frac{x}{\sqrt{2}} \right) \right], \tag{2.27}$$

where C_0 and D_0 are arbitrary constants. Importantly, the IR effective theory is continuously connected to the free Gaussian IR limit, as is often the case in perturbative RG.

If we lift the restriction of including the free Gaussian potential in our IR solution, then it becomes more natural to consider the second, continuous class of theories for which the Eq. (2.11) (or Eq. (2.8)) gives

$$\begin{aligned}\Psi(x) = e^{-\frac{1}{2}x^2}\Bigg[C_0\,{}_1F_1\left(\frac{1+E}{2};\frac{1}{2};\frac{x^2}{2}\right)\\ + D_0\,x\sqrt{\frac{2}{\pi}}\,{}_1F_1\left(\frac{2+E}{2};\frac{3}{2};\frac{x^2}{2}\right)\Bigg],\end{aligned} \tag{2.28}$$

where ${}_1F_1\left(a;b;x^2/2\right)$ is the confluent hypergeometric function of the first kind. The solution in Eq. (2.28) is valid for all E and reduces to (2.27) at $E=-1$.

A simple complete set of orthogonal polynomials (the Hermite polynomials) can be formed from the $\Psi(x)$ functions in (2.28) by restricting the eigenvalues E to be negative integers, $E \in \{-1,-2,-3,\ldots\}$. In this way, we can form an infinite series of finite and "normalisable" contributions to the expansion of Ψ_{UV} in (2.9). Here, we define normalisable to mean that the integral over x of $\Psi(x)^2$ is finite for some choice of E:

$$\int_{-\infty}^{\infty} dx\,\Psi_E^2(x) = \text{finite}. \tag{2.29}$$

However, in general, we expect that the integrals over $\Psi(x)^2$ need not converge to give us a physically acceptable effective potentials. Therefore in this chapter, we will also study such "un-normalisable" theories, for which the integrals diverge:

$$\int_{-\infty}^{\infty} dx\,\Psi_E^2(x) \to \infty. \tag{2.30}$$

In particular, the potentials that we will use as candidates for inflation will be of the un-normalisable type. In practice this means that the original theory $\Psi_{\rm UV}$ is expanded[5] in Eq. (2.9) with weights being continuous in E.

It is important to keep in mind that both MFA solutions, (2.27) and (2.28), can be non-perturbative in the coupling constants of the original UV theory. However, the dependence of the effective potential on the couplings can only be computed if we had

[5]E.g. this is similar to expanding any function that has a finite integral in terms of basis functions cosine and sine that themselves do not have a finite integral.

specified the UV theory and somehow computed the relevant overlap integrals that would reveal the true weights of Ψ_i in Ψ. We do not pursue this direction here and only consider IR effective potentials with unspecified dependence on the coupling constant.

Before we move on to considering the phenomenological implication of the two solutions, we note that our approach resembles that of the stochastic approach discussed in [87,88]. It is also similar to the approach of Halpern and Huang [102] and Periwal [103], where a linearisation of the ERG equation (2.2) was performed. Those works showed that there are non-polynomial deformations of the free Gaussian theory for which the Gaussian is IR-unstable. Such cases are also included in our analysis, within the MFA. Furthermore, this gives credence to the inclusion of the extra mode $\tilde{\psi}_0$ in addition to the Gaussian when considering theories of eigenvalue -1. It also prompts us to consider in detail theories with eigenvalue greater than -1, which can be argued to be preferable over the free theory from the exact renormalisation group point of view.

Finally, we also note that our non-perturbative result differs from the conventional perturbative approach where the effective Lagrangian is expanded in the powers of the field suppressed by some mass scale. Our approach is also different to what is known as the Effective Field Theory of Inflation [104], where the background dynamics sourced by a potential is assumed as given and the effective theory refers to the fluctuations around that background.

2.3 Inflation

2.3.1 Inflationary potential

Having found solutions that are likely to dominate the non-perturbative IR regimes of scalar theories, we now turn our attention to studying the phenomenological implications of such theories. In particular, we will show that solutions of Eq. (2.4) naturally lead to potentials capable of sustaining inflation in the early universe. The physical requirement in the patch of space-time where inflation starts is that the temporal derivative of the field is small and the field is homogeneous [86,105]. To describe inflation, we are therefore primarily interested in the potentials for the constant mode of the theory, which means that we can use our MFA results, where we effectively ignored the higher momentum

modes in order to derive equation (2.11) and its solutions.

We begin by restating the un-normalisable solution with a continuous spectrum of E_i, i.e. Eq. (2.28), as an effective potential of the scalar field ϕ. Restoring the mass dimensions,

$$\begin{aligned}\frac{V(\phi)}{M^4} =& \frac{1}{2}\left(\frac{\phi}{M_{\rm Pl}}\right)^2 \\ & - \log\left[{}_1F_1\left(\frac{1+E}{2};\frac{1}{2};\frac{1}{2}\left(\frac{\phi}{M_{\rm Pl}}\right)^2\right) + c\sqrt{\frac{2}{\pi}}\left(\frac{\phi}{M_{\rm Pl}}\right){}_1F_1\left(\frac{2+E}{2};\frac{3}{2};\frac{1}{2}\left(\frac{\phi}{M_{\rm Pl}}\right)^2\right)\right] \\ & + \frac{C(c)}{M^4},\end{aligned} \tag{2.31}$$

where $M_{\rm Pl}$ is the reduced Planck mass. The potential has an overall factor expressed in terms of some mass scale M. Furthermore, we have two integration constants c and C. Our universe has a very small cosmological constant, therefore the constant C needs to be fixed so that the vacuum energy at the minimum of the potential is zero, $V_{min} = 0$. This constrains C to be a function of c, i.e. $C(c)$.

At the minimum of the potential, the mass of the scalar field is independent of the shape parameter c,

$$\partial_\phi^2 V(\phi_{min}) = -\frac{EM^4}{M_{\rm Pl}^2}. \tag{2.32}$$

When $c \gtrsim 1$, the potential and its derivatives do not depend on c (see Fig. 2.1). Hence, the potential has a stable shape and the exact value of c for $c \gtrsim \mathcal{O}(1)$ does not matter.

We are particularly interested in the cases that dominate the IR regime of the RG flow, where $E \to 0^-$. For small $|E|$, the plateau region of the potential is not only flat, but also small (see Fig. 2.1). Such a potential can support slow-roll inflation as well as result in small amplitude of the scalar perturbations required by the observations, thus alleviating the fine-tuning of M (see next section).

Let us explore the plateau region. We can use the asymptotic expansion of the hypergeometric functions to obtain the leading behaviour that is logarithmic:

$$V(\phi) \approx M'^4\left[1 + \alpha\log\left(\frac{\phi}{M_{\rm Pl}}\right)\right]. \tag{2.33}$$

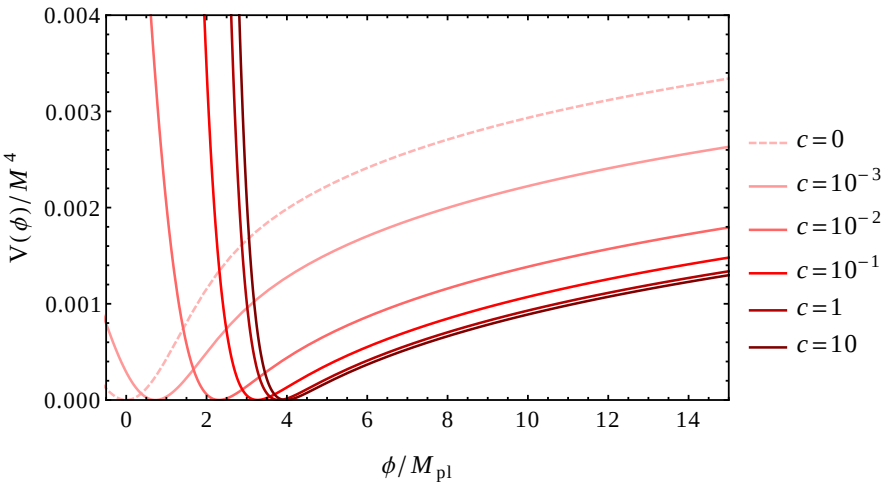

Figure 2.1: The dependence of the potential from Eq. (2.31) on the parameter c. Note that the shape does not change for $c \gtrsim \mathcal{O}(1)$. Here, we choose $E \sim -10^{-3}$.

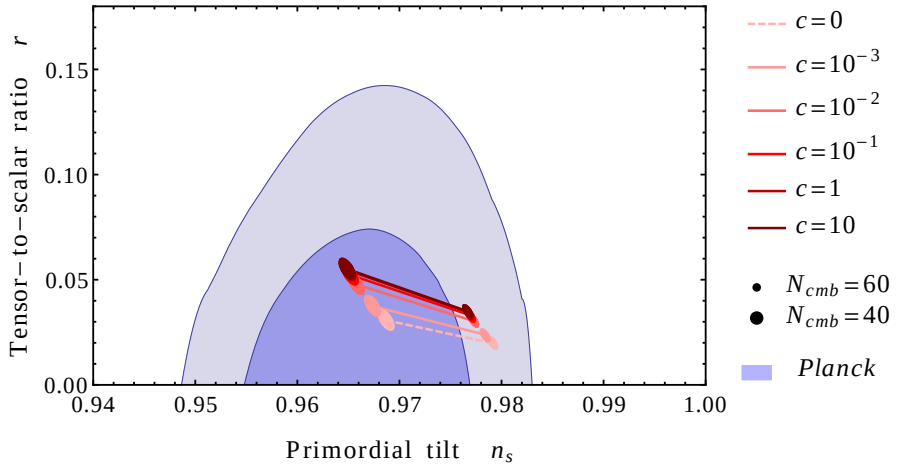

Figure 2.2: Predictions for the $(n_{\rm s}, r)$ plane for $-10^{-1} \lesssim E < 0$ against the observations (*Planck* TT+lowP data).

This potential shape is reminiscent of the 'Loop Inflation' model[6] where the logarithmic dependence arises from the loop corrections that spoil the flatness of the inflationary potential (aka the η-problem[7]). This has been studied in the context of the F- and D-term models in supersymmetric theories of inflation.[8]

2.3.2 The slow-roll analysis in theories with a continuous spectrum of E

Here we discuss the predictions of the potential in Eq.(2.31) for the main inflationary observables, the primordial tilt (also spectral index) $n_{\rm s}$ and the tensor-to-scalar ratio r

[6] Frequently termed 'Spontaneously broken SUSY' model.
[7] η is naturally of $\mathcal{O}(1)$ rather than $\ll 1$ as is required for inflation
[8] For a review of these approaches, see Refs. [69, 70] and references therein.

as well as constraints on the potential stemming from the measured amplitude A_s of fluctuations.

In Sec. 1.1.3.2 we studied the dynamics of a slowly rolling scalar field in an expanding universe. From the Eqs. (1.33) and (1.37) there we see that n_s and r do not depend on the overall factor M^4. Scanning the interesting parameter ranges, $-10^{-1} \lesssim E < 0$ and $0 \leq c < \infty$, the primordial tilt n_s changes by at most 0.5% and the tensor-to-scalar ratio r by a couple of per cent. Thus the slow-roll results stemming from the potentials considered here are fairly universal as well as completely consistent with the current observational constraints coming from *Planck* [106]. We plot the predictions for the (n_s, r) pair in Fig. 2.2.

On the plateau, the potential of the field is $V \sim |E|M^4$. As a result the amplitude of the scalar perturbations $A_\mathrm{s} \sim M^4|E|/M_\mathrm{Pl}^4$ is degenerate in parameters E and M. Observationally, the amplitude is given by $A_\mathrm{s} \approx 2.3 \times 10^{-9}$. For the ranges of E and c considered here, M can range from about two orders of magnitude below the GUT scale all the way to the Planck scale where our formalism breaks down as there is very little RG flow and gravitational effects become important. As a limiting case the potential in Eq. (2.31) gives the correct normalisation A_s for $M \sim M_\mathrm{Pl}$ and $E \sim -10^{-10}$.

2.3.3 The discrete case with $E = -1$

In the remainder of this chapter, we will limit ourselves to the theory with $E = -1$ in Eq. (2.25). As argued above, this special choice of the eigenvalue corresponds to the IR theory that is connected to the free theory. In terms of our quantum mechanical problem, this is the un-normalisable solution that contains the lowest-state normalisable mode (i.e. free theory) within the discrete spectrum of integral eigenvalues. Eq. (2.27) now gives us the potential for ϕ, which is

$$\frac{V(\phi)}{M^4} = \frac{1}{2}\left(\frac{\phi}{M_\mathrm{Pl}}\right)^2 - \log\left[1 + c\sqrt{\frac{\pi}{2}}\,\mathrm{erfi}\left(\frac{\phi}{\sqrt{2}M_\mathrm{Pl}}\right)\right] + \frac{C(c)}{M^4}. \tag{2.34}$$

We expect the overall scale M to be low, as we are examining the dominant solution of the ERG in the IR. As in the general case, fixing the constant C makes the potential

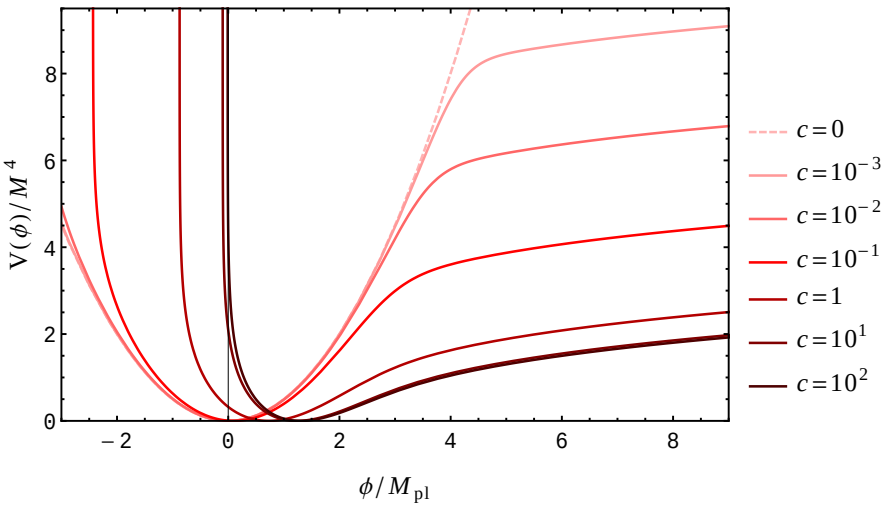

Figure 2.3: The potential from Eq. (2.34) depending on the parameter c. Note that the shape doesn't change for $c \gtrsim \mathcal{O}(1)$ and that for small c a kink appears in the potential.

only depend on the overall scale parameter M and the shape parameter c.

Again, at the minimum of the potential, $\partial_\phi V(\phi_{min}) = 0$, the mass of the scalar field is independent of the shape parameter c,

$$\partial_\phi^2 V(\phi_{min}) = M^4/M_{\rm Pl}^2. \tag{2.35}$$

Furthermore, when $c \gtrsim \mathcal{O}(1)$, the potential and its derivatives do not depend on c and the potential has a stable shape (see Fig. 2.3). The plateau of the potential and the quadratic behaviour near the minimum are also fairly independent of c. The parameter governs how sharp the transition is between the two regimes and where it happens. For smaller c the transition happens at higher ϕ. At $c = 0$ we restore the familiar quadratic potential of the free theory.

In the plateau region we use the asymptotic expansion of the error function,

$$\sqrt{\frac{\pi}{2}}\,\mathrm{erfi}\left(\frac{\phi}{\sqrt{2}}\right) \sim e^{\phi^2/2}\left(\frac{1}{\phi} + \dots\right), \tag{2.36}$$

which is approximately valid for $\phi \gtrsim 4M_{\rm Pl}$. As before, in Eq.(2.33), we recover the logarithmic behaviour reminiscent of the radiative corrections to a flat potential. In the special case considered here ($E = -1$), the corrections can be turned off for $c = 0$, when the free Gaussian theory is recovered.

The slow-roll predictions of our model are plotted in Fig. 2.4 against the observational constraints. The spectral index and the tensor-to-scalar ratio are independent of the

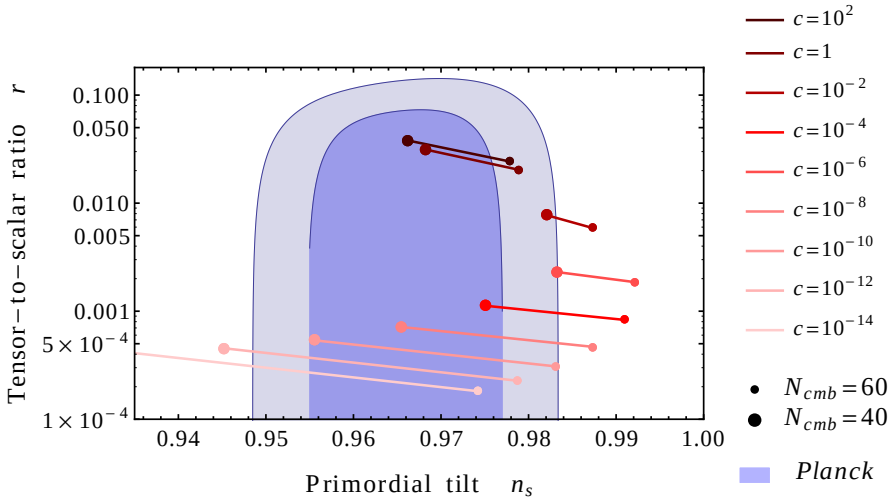

Figure 2.4: Predictions for the $(n_{\rm s}, r)$ plane against the observations (*Planck* TT+lowP data) when $E = -1$.

overall scale M. For the given shape of the potential (i.e. fixed c) the values of $n_{\rm s}$ and r are determined. Then M is determined such that the amplitude of fluctuations matches the observations. Hence, the inflationary model described by the potential in Eq. (2.34) would fall in the class of 'One parameter' models [70].

For the theoretically natural values of the shape parameter, $c \sim \mathcal{O}(1)$, we are in good agreement with the observed spectral tilt, but the expected gravitational background is higher and slightly disfavoured by the data (still within 1-2σ region)[9]. Parameter c measures the deformation of the potential away from the free theory ($c = 0$) and for sufficiently small values ($10^{-8} \lesssim c \lesssim 10^{-14}$) the scalar to tensor ratio r is reduced by several orders of magnitude so as to be consistent with the observations. This results in the further lowering of the scale M of the potential to about three orders of magnitude below the GUT scale, thus providing more room for the RG flow and adding to the validity of our analysis. Of course the required small value of c is similar to the 'fine-tuning' typically required in models of inflation. For the values of the shape parameter where $c \gtrsim 1$ the predictions of the discrete case with $E = -1$ and the cases where $0 > E > -1$ for the values of $n_{\rm s}$ and r are similar. This results in the degeneracy between the two parameters E and c describing our potentials.

For the cases of small c the potential we study develops a kink (see Fig. 2.3) that

[9]Large values for r are also disfavoured theoretically as they signal super-Planckian field excursions (i.e. the Lyth bound [107]).

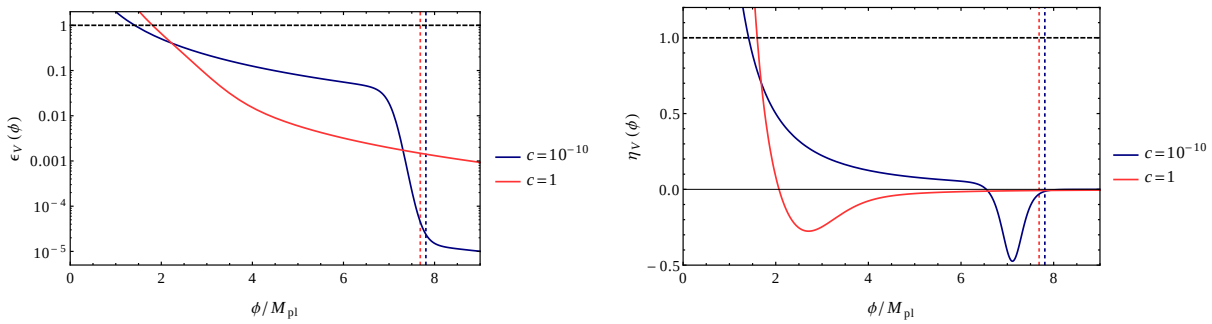

Figure 2.5: Inflationary slow-roll parameters for two potentials, one with a kink and one without. Note the transient deviation from the slow-roll phase. The vertical lines correspond to the field values where the CMB fluctuations are created.

introduces non-negligible derivatives of the field ϕ. This makes the slow-roll prediction as well as our mean-field approximation less accurate. In Fig.(2.5) we plot the two slow-roll parameters for the potentials with a kink and without one. The transient violation of the slow-roll conditions in the potential can give rise to observable features in the primordial power spectrum. This motivates further study with the exact integration of the inflationary background and perturbations together with the relaxation of the mean-field approximation in our derivation of the potential.

2.4 Summary

In this chapter, we studied non-perturbative scalar field potentials derived as an IR limit of the exact renormalisation group equation within the mean-field approximation where the field is assumed to be constant in space and time. This setup is just what is required to initiate the exponential expansion of space – inflation. The potentials we derived are capable of supporting slow-roll inflation with the values of the spectral index and tensor-to-scalar ratio consistent with the recent observations. Despite our very general treatment of the scalar field potentials, the slow-roll results are largely independent on the constants parametrising the potentials and thus result in fairly universal predictions. For the special case where we required that the IR theory was continuously connected to a free Gaussian fixed point, we identified a parameter range that led to transient violation of the slow-roll conditions. Hence, this results in a possibly observable feature in the primordial power spectrum, which should be studied further in the future.

Chapter 3: Inhomogeneity and anomalous diffusion

3.1 Introduction

The three dimensional distribution of matter observed on the sky exhibits a complex structure of nodes, filaments, walls, and voids. A similar "Cosmic Web" structure appears in N-body DM simulations. Due to the biasing of the luminous matter with respect to the dominant DM component, the knowledge of the distribution of DM in the universe comes mostly from such numerical simulations. This intricate distribution is far from the description used in standard models in cosmology which assumes a Friedmann-Lemaître-Robertson-Walker (FLRW) background with small density perturbations. The FLRW assumption is based on the high degree of isotropy inferred from observations of the cosmic microwave background (CMB) (once the dipole is subtracted) and the 'Copernican Cosmological Principle' [108]. The inhomogeneities are assumed to be only at small scales, so their effect should become vanishingly small after averaging over large enough scales, such that the simple description applies. It is therefore important to identify the scale above which the statistical properties of the universe do not depend on the location. This requires a definition of the notion of the transition to (statistical) homogeneity.

One approach to characterise the complex structure in the universe is via fractal analysis. Fractal analysis can also be used to determine the transition to homogeneity in a statistical sense. The analysis has been applied to redshift galaxy surveys: PSCz [109], SDSS LRG [110], SDSS DR6 [111], WiggleZ [112], SDSS DR9 [113] and to N-Body simulations [114, 115]. The quantities of interest are the number of objects within a sphere of radius r, $n(< r)$, and its scaling with r. This is known as a 'counts-in-cells' method. The scaling exponent (or fractal dimension) approaches 3 on the large scales, which is the case for a homogeneous distribution. The transition to homogeneity has been detected at a scale of $70\,h^{-1}$Mpc [112] all the way up to $180\,h^{-1}$Mpc [113], or not detected at all [116].

Many different definitions for the transition have been used. Ref. [117] defines the

transition to homogeneity at the point where the clustered distribution scaling exponent cannot be distinguished from the homogeneous one within 1σ uncertainty. The transition, of course, depends on the survey size and intrinsic clustering. They find, for the standard ΛCDM universe, the upper bound for the transition (according to their definition) to be about $260\,h^{-1}$Mpc.

Another definition for the transition has been developed in Ref. [112]. The definition is insensitive to the statistical error of the scaling exponent, but it arbitrarily chooses the transition to happen when the exponent reaches to within 1% of the homogeneous value. This enables comparison of different surveys at the expense of arbitrariness.

The 'counts-in-cells' method was modified to test cosmic homogeneity with Shannon entropy [118]. This made possible a discussion of the finite volume effect of the surveys and the effect of overlapping of the spheres used to measure the scaling dimension. Those effects contribute to the confinement bias (sample of spheres mainly coming from the centre of the survey with lots of overlap), which is especially important for inhomogeneous samples with large fluctuations.

Recent proposals to quantify the structure of the "Cosmic Web" focus on the topology, studying the scale-dependent Betti numbers [119] or the genus statistic [120]. The topological information can be used as a measure of cosmological parameters [121].

In this chapter we revisit and improve the results from [115], which uses the 'counts-in-cells' method on 'Millennium Run' (MR) simulation [122]. We use one of the biggest N-body simulations to date [123] from the 'Dark Sky Simulations' (DS) [44] to avoid the finite volume and overlapping bias, which appear in smaller simulations like the MR simulation when large distances are probed. It is found that MR-sized simulations or samples are inadequate to accurately measure the transition to homogeneity.

We extend the methods of fractal analysis to include anomalous diffusion on the DM halo distribution. Diffusion can be modelled as a continuum limit of random walkers on the underlying network [124]. It probes different properties of the underlying point set compared with the 'counts-in-cells' method [125]. Anomalous diffusion exhibits a number of scaling exponents (or dimensions) that are different from the normal diffusion and is associated with a fractal structure of the network [125, 126]. Thus, it can be used as another characterisation of the distribution of matter. The methods and relevant

theoretical background are summarised in Sec. 3.2. Results for the determination of the fractal exponents and their scale dependence for the 'counts-in-cells' method and methods based on anomalous diffusion are presented in Sec. 3.3.

3.2 Methods and theoretical background

Visual inspection of the distribution of matter in the universe exhibits a self-similar "Cosmic Web" structure. A point set (e.g. DM halos, galaxies) can be characterized via a number of scaling dimensions. Cosmologically, we are interested in the spatial scale above which the transition to a homogeneous distribution occurs, which is determined by scaling dimensions reaching the usual, homogeneous values.

The simplest fractal dimension is the 'counts-in-cells' dimension,

$$N_i(< r) \propto r^{D_i} \tag{3.1}$$

which counts the number of points within a sphere of radius r centred on the point i with the scaling fractal dimension D_i. An associated quantity, the correlation integral, is defined as in [127–130]:

$$C_2(r) = \frac{1}{NM} \sum_{i=1}^{M} n_i(< r) \tag{3.2}$$

where N is the total number of points in the distribution (formally $N \to \infty$) and M is the number of centres on which spheres of radius r have been positioned. This exhibits scaling:

$$C_2 \propto r^{D_2}, \quad D_2 = \frac{\partial \log C_2(r)}{\partial \log r} \tag{3.3}$$

The deviation of the correlation (or 'counts-in-cells') dimension D_2 from the ambient value D is due to clustering of points. In samples that are big enough to possess a well defined average number density $\overline{n}$ we can define the two-point correlation function $\xi(r)$ as the excess probability above random to find two-points separated by distance r in volumes $\mathrm{d}V_1$ and $\mathrm{d}V_2$ [131]:

$$P(r) = \overline{n}^2 \left(1 + \xi(r)\right) \mathrm{d}V_1 \mathrm{d}V_2 \tag{3.4}$$

Hence, the correlation integral $C_2(r)$, which is proportional to the average number of

points within a certain radius, can be written as:

$$C_2(r) \propto \int_0^r \overline{n}\,(1+\xi(r'))\,4\pi r'^2 \mathrm{d}r' = \frac{\overline{n}4\pi r^3}{3}\left(1+\frac{3}{4\pi r^3}\int_0^r \xi(r')4\pi r'^2 \mathrm{d}r'\right) \tag{3.5}$$

The last term in the brackets above is the average $\overline{\xi}(r)$ of the two-point correlation function up to radius r. Using Eq.(3.3) we can write the 'counts-in-cells' dimension in the limit of weak clustering ($\overline{\xi}(r) \ll 1$) as $D_2(r) \simeq D - D(\overline{\xi}(r) - \xi(r))$ [127]. Hence, the 'counts-in-cells' dimension contains the same information as the two-point correlation function, provided that the number density $\overline{n}$ can be defined.

The structure of matter in the universe is highly irregular and does not exhibit just one simple scaling. Different moments of the correlation integral can be taken to extract more information from the distribution. The generalised correlation integral and dimension are:

$$C_q(r) = \frac{1}{NM}\sum_{i=1}^{M} n_i^{q-1}(<r), \quad D_q = \frac{\partial \log C_q(r)}{\partial \log r} \tag{3.6}$$

A mono-fractal has just one scaling $D_q = D_2$ at all scales, whereas a multi-fractal has a spectrum of D_q. Positive values of q put more weight on the dense regions whereas negative values on the underdense ones. We can thus extract the scaling behaviour for points mainly located in clusters or voids.

3.2.1 Transition to homogeneity

The correlation dimension D_2 depends on the spatial scale r. We are interested in the distance above which the distribution of objects is homogeneous. In the framework of the fractal analysis, this happens when the scaling dimension is equal to the ambient dimension (e.g $D_2 = 3$). For finite samples, however, the ambient value cannot be reached exactly. Based on [117], a clustered distribution is defined to become homogeneous when $D_2^{\text{clustered}}$ cannot be distinguished from $D_2^{\text{unclustered}}$ of the unclustered distribution within their errors. That is, $D_2^{\text{unclustered}} - D_2^{\text{clustered}} = \Delta D_2 \simeq \sigma_{\Delta D_2}$, where $\sigma_{\Delta D_2}$ is the statistical error, which has been calculated to happen at about $260\,h^{-1}$Mpc for the ΛCDM model [117]. This definition is statistically well-motivated. However, this only considers the statistical contribution. Additional contributions to $\sigma_{\Delta D_2}$ due to survey

geometry, sparseness and the selection function bias the above definition of the transition to homogeneity towards smaller values.

The unclustered[1] distributions we use are of the same size as the clustered sample in terms of the volume and the number of objects, but in which the positions of the objects are random.

Above the scale of homogeneity the number of points within a certain radius roughly scales as $N(< r) \propto r^3$. Hence, the average number density $\overline{n} = N/V$ is well defined as it does not depend on the scale r. Therefore, in the samples that exhibit transition to homogeneity the expression in Eq.(3.5) can be used to calculate the correlation dimension D_2.

3.2.2 Diffusion

Normal diffusion

Diffusion on a point set or a network can be modelled with a large number of random walkers[2]. Diffusion is their continuum limit. The walkers jump to neighbouring points from their current position and thus traverse a certain distance, assuming the set of points is embedded in a space that has a notion of distance (e.g. Euclidean space). The standard result for the random walkers (assuming the uncorrelated nature of the walk and no directional bias) is:

$$\langle \mathbf{R}^2 \rangle = \int P(r,t) r^2 \mathrm{d}^d\mathbf{r} \propto t \tag{3.7}$$

$$P(\mathbf{r}, t|K, d) = \frac{1}{(4\pi K t)^{d/2}} \exp\left(-\frac{d\, r^2}{4Kt}\right) \tag{3.8}$$

That is, the mean squared displacement $\langle \mathbf{R}^2 \rangle$ scales with the number of steps t and is independent of the dimension d of the Euclidean space. This is a property of normal diffusion. $P(\mathbf{r}, t|K, d)$ is the probability distribution for the distance $\mathbf{r}$ of the random walker from the origin after t number of steps with K being the diffusion coefficient and d the dimensionality of the underlying space.

On a lattice point set the random walker jumps onto the neighbouring points. However, on non-lattice point sets random walkers have to be supplied with the notion of

[1]The terms "unclustered", "random", and "homogeneous" will be used interchangeably

[2]For a short review see Ref. [126]

neighbouring points. To have a meaningful long-distance scaling, the prescription for the random walker on how to jump to the next point should be limited to short distances. The asymptotic scaling should also be robust against changes in the short-distance prescription. This can be achieved by linking each point to a fixed number of the nearest points, thus creating a network for the walkers. This prescription introduces a slight modification of the scaling law at short distances, while the asymptotic behaviour remains unchanged with respect to the number of nearest points the walker is allowed to jump on.

Anomalous diffusion

A diffusive process is said to be anomalous [124] if the mean squared displacement grows as:

$$\langle\langle \mathbf{R}_i^2 \rangle\rangle_i \propto t^\alpha \tag{3.9}$$

with $\alpha \neq 1$. Again, t is the number of steps of the random walker, i the initial position of the walker, and $\langle\cdot\rangle_i$ is the average over positions i. The values with $\alpha < 1$ and $\alpha > 1$ correspond to subdiffusion and superdiffusion.

The advantage of this method is that the anomalous diffusion exponent α is the same ($\alpha = 1$) for homogeneous distributions in any dimension, unlike the 'counts-in-cells' method which gives $D_2 = 1, 2, 3$ respectively for a homogeneous line, sheet, and volume distribution and does not necessarily imply fractal behaviour. For example, a galaxy located in a wall would have $D_2 \simeq 2$ but $\alpha \simeq 1$. Similarly as the 'counts-in-cells' method, the homogeneity is reached when $\alpha^{\text{unclustered}}(R) - \alpha^{\text{clustered}}(R) = \Delta\alpha(R) \simeq \sigma_{\Delta\alpha(R)}$ at a certain 'radius' R. Note that the effective distance scale here is $\sqrt{\langle \mathbf{R}^2 \rangle}$, meaning that the diffusion is sensitive to a range of scales.

Cosmological data (simulated or observed) is limited in volume. Therefore, a diffusion process must be stopped as it reaches the boundaries of the dataset to prevent unphysical leakage (or reflections) of random walkers from the volume. In other words, the whole probability distribution must be contained within the dataset volume to correctly evaluate the mean distance squared of the random walkers. This imposes an upper bound on the distances probed (smaller than characteristic length-scale of the sample)

and makes this method suitable only for large-volume datasets.

Conversely one can consider:

$$\langle\langle T\rangle\rangle_i \propto R^{d_w} \tag{3.10}$$

The walk dimension d_W is defined via the mean number of steps $\langle T\rangle$ that a random walker needs in order to leave for the first time a ball of radius R centred on the position i. This method has a clearly defined scale R, unlike the previously discussed method above that considers the mean square displacement $\sqrt{\langle \mathbf{R}^2\rangle}$. It is comparable to the 'counts-in-cells' method in terms of efficiency of volume use. For normal diffusion we have $d_W = 2$, and for a mono-fractal with one scaling exponent we have $d_W = 2/\alpha$. Again, the distribution is homogeneous above the radius where $\Delta d_W(R) \simeq \sigma_{\Delta d_W(R)}$.

From Eq.(3.8) we see that the direct handle on the dimensionality of the underlying Euclidean or fractal space is the probability of return $P(\mathbf{r} = \mathbf{0}, t) \propto t^{-d_s/2}$, where d_s is the spectral dimension ($d_s = 3$ for a homogeneous three dimensional distribution). However, this approach is difficult to apply on cosmological data that is limited in volume. Random walkers might leak out of the box and never return, thus biasing the probability of return. Also, spatial scale is not present directly. The scale can be indirectly inferred from the diffusion time t, i.e. long/short t corresponds to large/small spatial scale.

3.3 Results and discussion

In all the determinations of the scaling exponents' dependence on the radial distance we use linear fits to the log-log data with $15\,h^{-1}$Mpc bin size. We use N-Body simulation data from the Dark Sky (DS) Simulations [44] described in detail in Sec. 1.1.5.

3.3.1 'Counts-in-cells' dimension and the overlapping/confinement bias

Here we revisit the results from [115] that measured the 'counts-in-cells' dimension $D_2(r)$ in the Millennium Run simulation. We address the shortcomings mostly stemming from the small size of the simulation ($500\,h^{-1}$Mpc box). The periodic boundary conditions used in the MR simulation limit the typical distance between two points to

below $250\,h^{-1}$Mpc and homogeneity is imposed automatically at this radius[3]. This is at odds with the theoretical expectation in ΛCDM ($\sim 260\,h^{-1}$Mpc) [117].

Ref. [115] determined the 'counts-in-cells' dimension by drawing a thousand randomly selected centres from the DM halo distribution that were at least a certain distance ('depth') away from the edges of the box (without taking advantage of the periodic boundary conditions). They noticed 'spurious homogenisation' effects, specifically, $D_2(r)$ exceeding the ambient dimension $D_2 = 3$ at radii ('depths') larger than $160\,h^{-1}$Mpc. The origin of this unphysical result is the fact that at larger radii the spheres were preferentially drawn from the central part of the simulation box and thus could not be considered statistically independent. Taking many large overlapping spheres, all with centres in a small central subregion of the simulation box makes the errors artificially low which in turn hides the underlying bias in the determination of D_2 (i.e. the 'confinement' and 'overlapping' bias [116, 118]). Therefore, in order to overcome the shortcomings described above and reliably probe scales $\sim 100\,h^{-1}$Mpc a volume much bigger than the MR simulation is needed.

The Dark Sky Simulation with a volume of $(8000\,h^{-1}\text{Mpc})^3$ is big enough to draw a thousand spheres from it that do not overlap significantly. The correlation dimension $D_2(r)$ is calculated up to $200\,h^{-1}$Mpc. The same method is applied to a random catalogue of the same size and the same number of points (see Fig. 3.1). This compares to the work done before on the Millennium Run simulation DM halo catalogue, which used a thousand significantly *overlapping* spheres drawn from it.

In Fig. 3.1 we see that the scaling for the random distribution reaches the expected value ($D_2(r) \simeq 3$) at about $40\,h^{-1}$Mpc. Before that radius the effects of discreteness influence the scaling dimension (mean particle separation λ is $\sim 6\,h^{-1}$Mpc, so the scaling makes sense at radii $r \gg \lambda$). Hence, the relevant quantity that determines whether a clustered distribution can be distinguished from the random one is $\Delta D_2(r) = D_2^{\text{clustered}}(r) - D_2^{\text{unclustered}}(r)$, which is plotted in Fig. 3.2.

The 'counts-in-cells' dimension $D_2(r)$ is always below $D_2 = 3$ all the way to $200\,h^{-1}$Mpc, avoiding the spurious effects resulting from the significant overlap as discussed above. Even small inhomogeneities above about $100\,h^{-1}$Mpc are detectable since the correlation

[3]Modes bigger than that are missing altogether

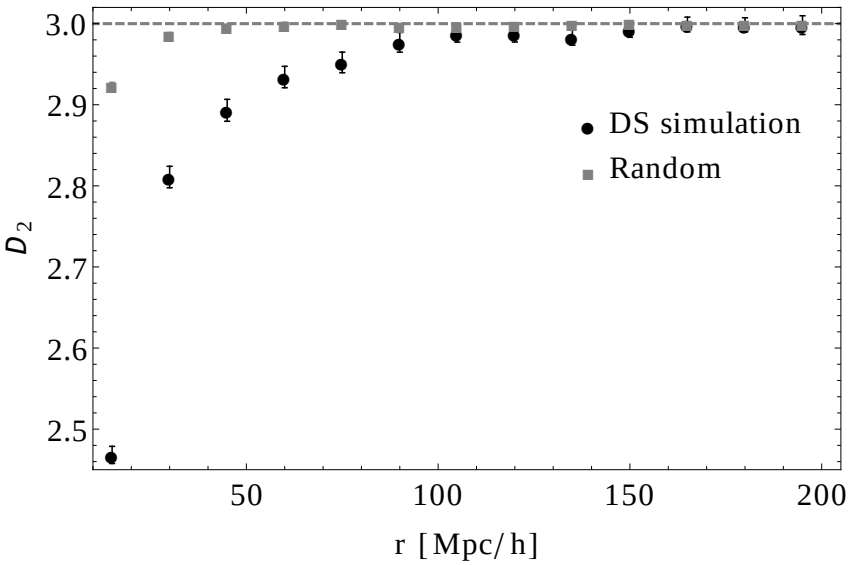

Figure 3.1: $D_2(r)$ for DS simulation and an equivalent random distribution. The scaling for the random distribution reaches $D_2 = 3$ very quickly. Note that the errorbars for the random distribution are much smaller compared to the clustered one.

dimension D_2 has not reached the homogeneous value within its errorbars. The transition to homogeneity happens at about $150\,h^{-1}$Mpc which is higher than but broadly comparable to previous work [115].

We illustrate the 'confinement' and 'overlapping' bias by randomly selecting a thousand centres in each of 10 MR-sized $(500\,h^{-1}\text{Mpc})^3$ subvolumes of the DS simulation. The exponent D_2 is determined for depths $200\,h^{-1}$Mpc and $140\,h^{-1}$Mpc in each subvolume. This is then compared to the D_2 exponent deduced by using a thousand centres from the full DS volume where the spheres are not overlapping significantly. We plot $\Delta D_2(r) = D_2^{\text{independent}}(r) - D_2^{\text{overlapping}}(r)$ in Figs. 3.3 and 3.4. The bias is bigger and the errors relatively smaller for the depth of $200\,h^{-1}$Mpc compared to $140\,h^{-1}$Mpc since the sampled spheres overlap more and are more confined. The systematic offset persist across all scales, also the relevant ones at around $100\,h^{-1}$Mpc. This suggests that volumes as small as the MR simulation are prone to systematic bias of the order of 1%. Hence, the methods to determine the transition to homogeneity either by focussing on the statistical error in the scaling exponent, $\sigma_{\Delta D_2}$ [117], or proximity to the theoretical scaling exponent, $(D_2 - D)/D = 1\%$ [112], cannot be applied reliably. This analysis also shows that the precise shape of the two-point correlation function, which is related to D_2 via $D_2(r) \simeq D - D(\overline{\xi}(r) - \xi(r))$, is also affected when measured in a MR size simu-

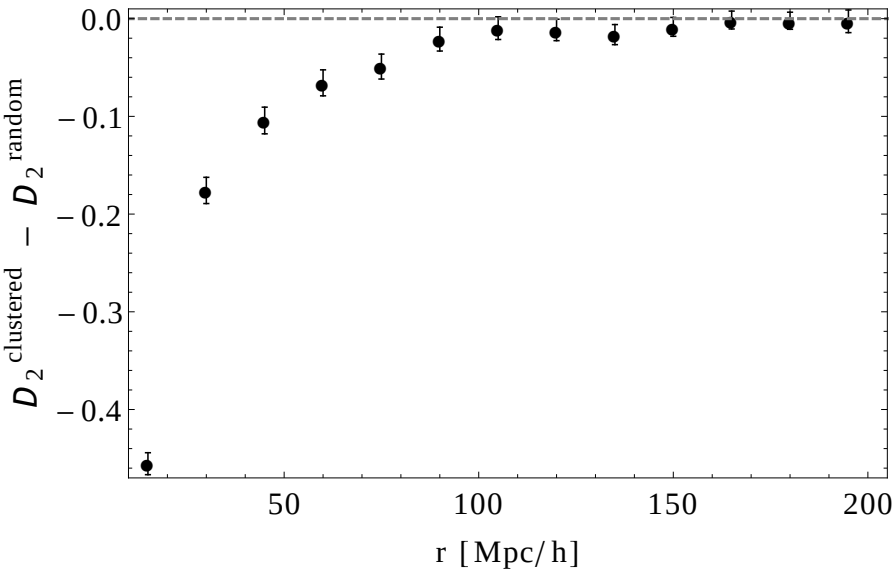

Figure 3.2: $\Delta D_2 = D_2^{clustered} - D_2^{random}$ vs radius in h^{-1}Mpc for 'counts-in-cells' method. The transition to homogeneity happens at around $150\,h^{-1}$Mpc.

lation or a survey. For a MR-sized simulation the biases can be mitigated by employing periodic boundary conditions which reduce confinement and overlapping of the spheres.

3.3.2 Anomalous diffusion dimensions

In this section we discuss a new method of characterising the cosmic structure as seen in DM halos in N-Body simulations. It is based on the concept of anomalous diffusion (Sec. 3.2) which we model using random walkers.

The network used for random walkers was constructed in such a way that each DM halo had a neighbourhood of 12 nearest halos. The construction of the network is computationally expensive, especially for large catalogues. Additionally, the links that were farther than $20\,h^{-1}$Mpc were rejected in order to keep short-distance effects from influencing the long-distance scaling. This lower 'cut-off' provides a separation of small scales from the large ones that are of interest here. However, together with the discreteness of the data, the 'cut-off' introduces spurious effects at smaller scales which can be seen for the diffusion on the unclustered random distribution of halos (see Fig. 3.5 and Fig. 3.7). Note how the scaling for the random distribution approaches the expected theoretical values. To correct for this spurious effect, the difference of scaling exponents between the clustered and unclustered distributions is taken as relevant for the study of the transition to homogeneity.

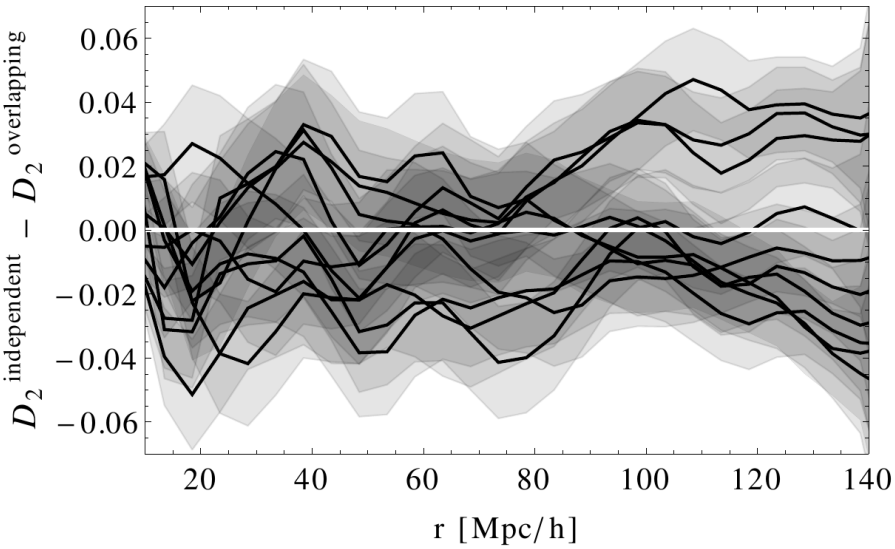

Figure 3.3: Each black line represents the difference between the 'counts-in-cells' dimension, $\Delta D_2 = D_2^{independent} - D_2^{overlapping}$, calculated in the full DS volume and in one of the ten $(500\,h^{-1}\text{Mpc})^3$ subvolumes of DS where the spheres overlap substantially. 'Depth' is $140\,h^{-1}$Mpc. Shaded regions are errors ($\approx \pm 0.02$) corresponding to each line.

The analysis was repeated for a network constructed by connecting each halo to the 18 nearest halos. This was done in order to check that the results for the scaling dimensions did not substantially depend on such a choice[4] (see Fig. 3.6 and Fig. 3.8). Some differences are expected at smaller scales due to spurious discreetness effects.

The method was applied to a set of lattice distributions and deterministic fractal distributions with known scaling exponents in order to confirm that the implementation of the diffusive process gave correct asymptotic scaling exponents.

The number of walkers for each starting point is chosen to be very large in order for the walkers to saturate the possible ways of exploring a given volume starting from a specific point. Thus, the spread in the scaling exponents comes dominantly from having different points used as centres for the random walkers.

3.3.2.1 Mean square displacement scaling α

The scaling of the mean distance squared with the number of steps, $\langle \mathbf{R}^2 \rangle \propto t^{\alpha}$, up to an effective radius $\sqrt{\langle \mathbf{R}^2 \rangle}$ of $220\,h^{-1}$Mpc was explored. The number of starting centres for the random walkers was 512 and care was taken to make sure that the diffusion processes were terminated before overlapping significantly.

[4]As well as varying the number of nearest neighbour links we also set the 'cut-off' length for the links to $15\,h^{-1}$Mpc and $25\,h^{-1}$Mpc to check that arbitrariness on the small scales did not influence the values on the large scales.

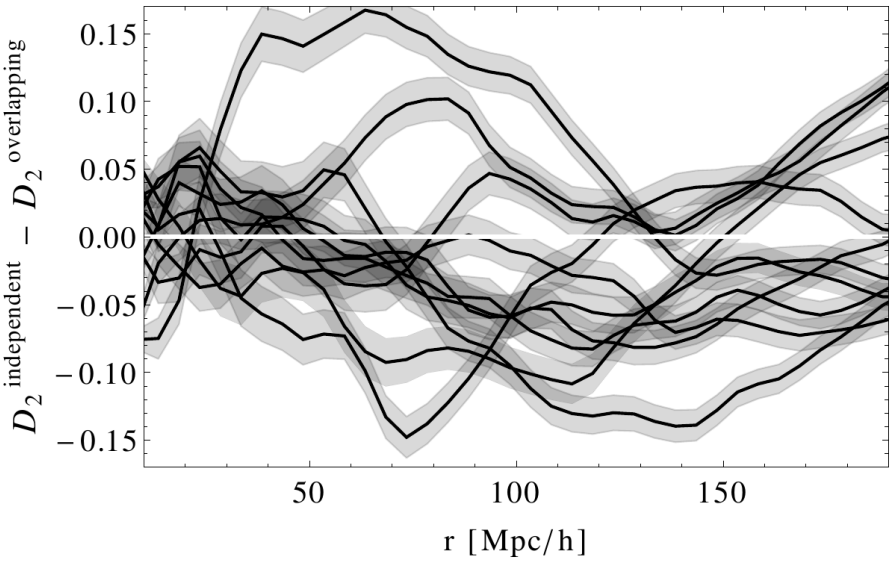

Figure 3.4: Each black line represents the difference between the 'counts-in-cells' dimension, $\Delta D_2 = D_2^{independent} - D_2^{overlapping}$, calculated in the full DS volume and in one of the ten $(500\,h^{-1}\text{Mpc})^3$ subvolumes of DS where the spheres overlap substantially. 'Depth' is $200\,h^{-1}$Mpc. Shaded regions are errors ($\approx \pm 0.02$) corresponding to each line.

This is a less efficient method in terms of using the available volume compared to the 'counts-in-cells' method. The reason is that, in order to evaluate the scaling exponent α, all the random walkers for a given number of steps t_0 are needed. Hence, the diffusive process extends over a range of scales (with the characteristic scale $\sqrt{\langle \mathbf{R}^2(t_0)\rangle}$ much smaller than $|\mathbf{R}_{max}(t_0)|$). As a result, the transition to homogeneity happens slowly as the notion of scale is spread out (see Figs. 3.7 and 3.8). This explains the slow convergence of α for the random distribution to the theoretical value $\alpha = 1$ as well as the slow convergence of the clustered distribution to the random one up to $\sqrt{\langle \mathbf{R}^2\rangle} \sim 220\,h^{-1}$Mpc.

3.3.2.2 Walk dimension d_W

The scaling of the mean number of steps needed to leave a ball of radius R, $\langle T\rangle \propto R^{d_w}$, was determined up to $350\,h^{-1}$Mpc. The same volume of $(8.0h^{-1}\,\text{Gpc})^3$ as in the 'counts-in-cells' method was used (same efficiency of volume use). This enables a direct comparison of the results and the errorbars. The distance scale for this diffusive process is well-defined, contrary to the method measuring α discussed above. This can be seen from the walk dimension d_W and anomalous diffusion dimension α for the unclustered distribution in Figs. 3.5 and 3.7. The walk dimension, d_W, converges to the

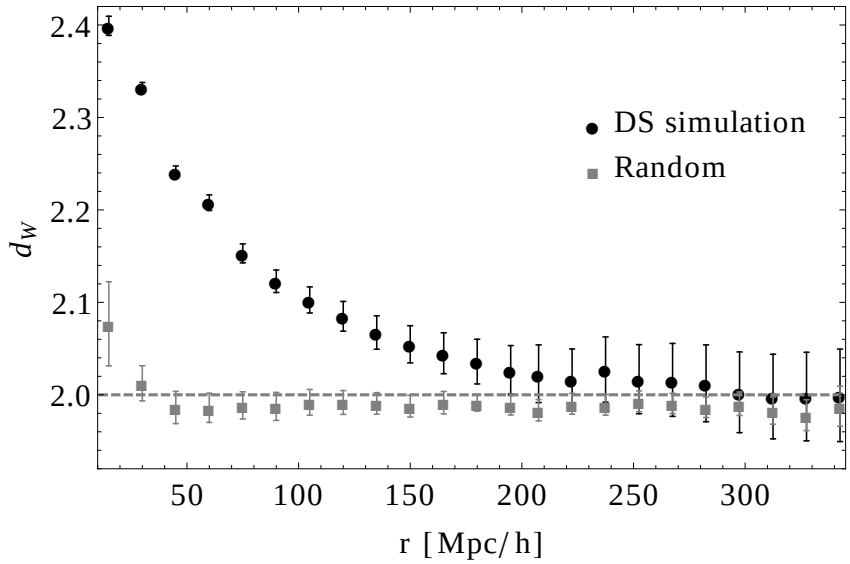

Figure 3.5: $d_W(r)$ for DS and equivalent implementation on a random catalogue. The small scale effects of the implementation of the random walkers is seen in the lower set of points (random catalogue). Anomalous diffusion persists beyond $200\,h^{-1}$Mpc in the clustered distribution.

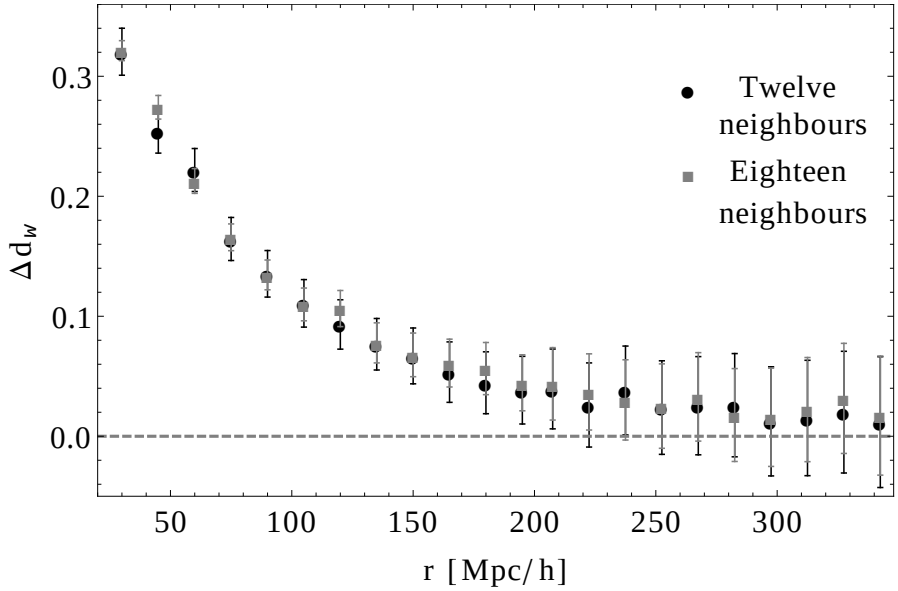

Figure 3.6: $\Delta d_W = d_W^{clustered} - d_W^{unclustered}$ between the DS sample and a random distribution for the implementation where the neighbourhood of each halo is the 12 or 18 nearest halos.

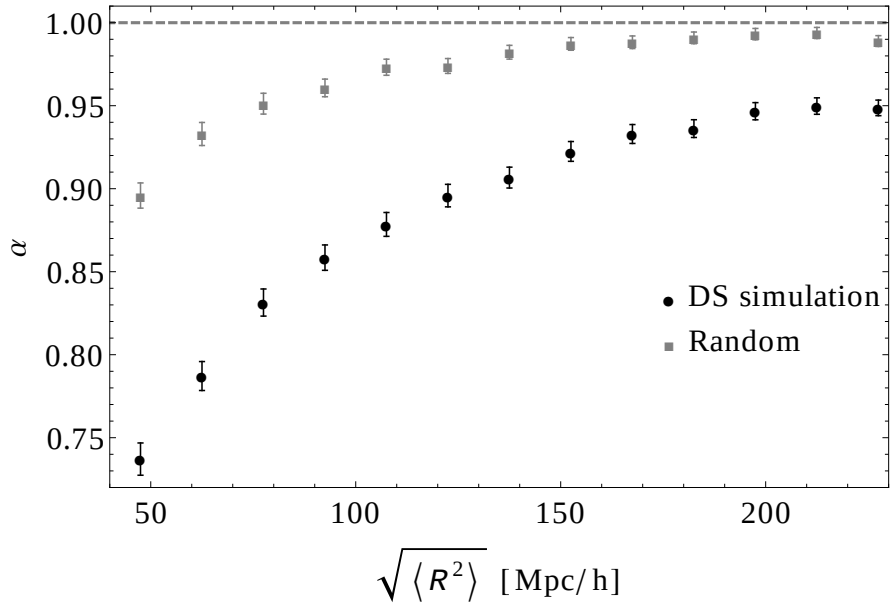

Figure 3.7: Mean square displacement scaling $\alpha(r)$ for a random distribution (upper set of points) and DS for the implementation where the neighbourhood of each halo is the nearest 12 halos.

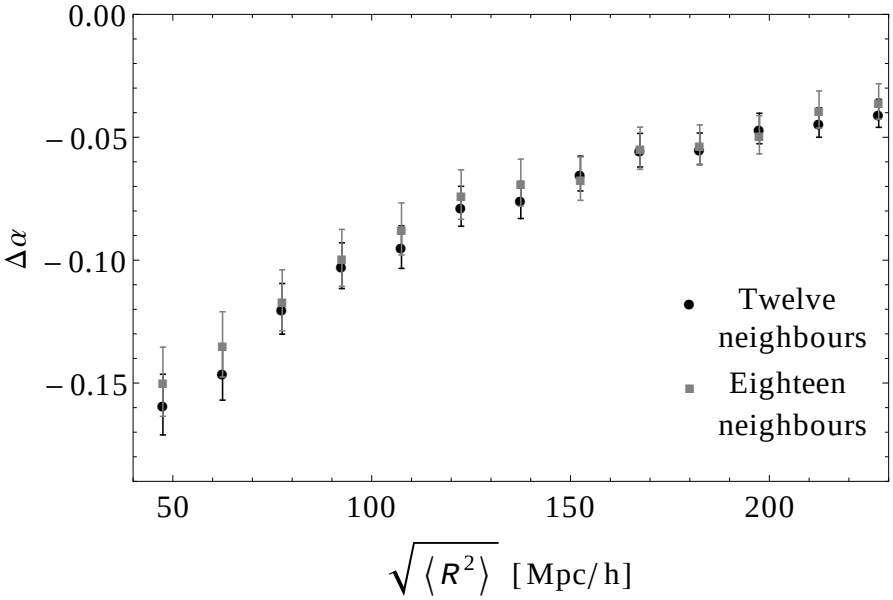

Figure 3.8: $\Delta\alpha = \alpha^{clustered} - \alpha^{unclustered}$ between the DS sample and a random distribution for the implementation where the neighbourhood of each halo is the nearest 12 or 18 halos.

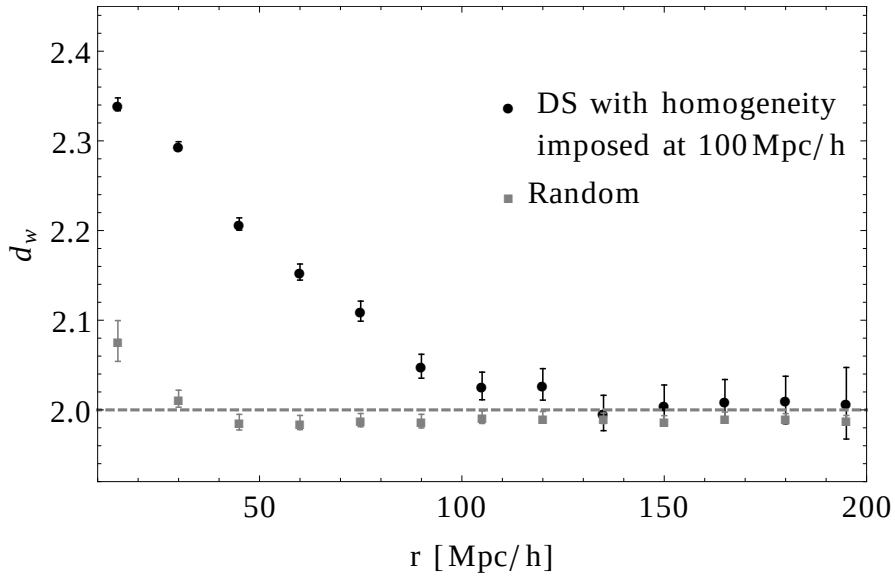

Figure 3.9: $d_W(r)$ for the case where the homogeneity is artificially imposed at $100\,h^{-1}$Mpc. The lower set of points corresponds to the unclustered distribution.

theoretically expected value at about $50\,h^{-1}$Mpc whereas α takes longer. The transition to homogeneity via anomalous diffusion, as defined in Sec. 3.2, happens at a different, larger scale (above $250\,h^{-1}$Mpc) than for the 'counts-in-cells' method (see Figs. 3.5 and 3.6).

It is useful to check how sensitive the walk dimension d_W is to the transition to homogeneity. This is done by randomly sampling subvolumes of the DS simulation with $100\,h^{-1}$Mpc box lengths and imposing periodic boundary conditions to achieve homogeneity at this scale. In Fig. 3.9 we see that the transition to homogeneity does begin at about $100\,h^{-1}$Mpc. This should be compared with Fig. 3.5, where the transition happens later, as described above.

3.4 Summary

In this chapter we investigated dark matter clustering at the present epoch from a fractal viewpoint in order to determine the scale where the self-similar scaling property of the DM halo distribution transits to homogeneity. We used the well-established 'counts-in-cells' methods as well as completely new approaches based on anomalous diffusion and random walks. The methods were tested on the biggest DM halo catalogue from the 'Dark Sky Simulations' (DS), a very large N-body simulation of $(8h^{-1}\,\mathrm{Gpc})^3$ volume. Diffusion was modelled by performing random walks on the set of halos. The underlying

distribution was described by scaling exponents for various diffusive processes. Determination of the values of the scaling exponents and their dependence on the distance scale was used to decide whether a particular distribution of DM halos could be distinguished from the homogeneous one.

We measured the mean number of steps $\langle T \rangle$ for a random walker to leave a ball of radius R, and how it scaled with the radius: $\langle T \rangle \propto R^{d_w}$. In terms of efficiency of volume use, this method is comparable to the 'counts-in-cells' method, which has been extensively used in the past to characterise the distribution of matter in the universe. For an explicitly homogeneous distribution (i.e. random, unclustered) we find quick convergence of d_W to the theoretically expected value, namely $d_W \simeq 2$. For the diffusion on the DS distribution of halos we find the convergence of the scaling exponent d_W to the homogeneous value to be at about $250\,h^{-1}$Mpc, which establishes a characteristic distance describing the distribution.

We also measured how the RMS distance traversed by a random walker scaled with the number of steps, $\langle \mathbf{R}^2 \rangle \propto t^{\alpha}$. The notion of distance here is only effective, $\sqrt{\langle \mathbf{R}^2 \rangle}$, and therefore sensitive to a range of scales. Unsurprisingly the convergence of the scaling exponent α to the homogeneous values was slow. Measuring α probes shorter distance scales compared to the method above in a finite volume sample and is less efficient in the use of the available volume.

The size of the DS simulation also enabled the improvement in the determination of the 'counts-in-cells' fractal dimension compared to previous work that used smaller volumes. We showed that Millennium Run sized volumes used in past studies of the 'counts-in-cells' fractal dimension are not sufficiently big to precisely and accurately determine the transition to homogeneity, irrespective of the exact definition when transition happens. In particular, not taking advantage of the periodic boundary conditions in previous work resulted in preferential sampling of the central regions and consequently led to 'confinement' bias. The substatial overlapping of the spheres also meant artificial reduction of the errorbars. We found that the transition to homogeneity, as measured by the 'counts-in-cells' dimension, happens at around $150\,h^{-1}$Mpc at redshift $z = 0$ which is slightly higher but broadly consistent with previous studies.

Chapter 4: How rare is the Bullet Cluster?

4.1 Introduction

Large clusters of galaxies are the biggest gravitationally bound objects in the universe. Naïvely they would be expected to correspond to 'fundamental observers' who follow the Hubble flow and move *away* from each other. The discovery of the Bullet Cluster (1E 0657-56), a system consisting of two very massive clusters of galaxies which have undergone a collision with a high relative velocity, thus requires an assessment of whether the standard ΛCDM cosmology is able to accommodate such an extreme event. The subsequent discovery of many more merging clusters[1] motivates a general study of the statistics of such events. Since such collisions involve non-linear interactions, the predictions of the ΛCDM model have to be extracted from cosmological N-body simulations.

The Bullet Cluster located at $z = 0.296$ is the best studied of such mergers, since its collisional trajectory is normal to the line of sight. It is extreme in several respects. The main cluster has a high mass of $M_{\rm main} \simeq 1.5 \times 10^{15} M_\odot$, with the subcluster mass $M_{\rm Bullet} \simeq 1.5 \times 10^{14} M_\odot$, separation $d_{12} \simeq 0.72\,{\rm Mpc}$ [132, 133], and a very high velocity $v_{12} \simeq 4500\,{\rm km/s}$ [134] deduced from the analysis of the bow shock. This should be compared to the expected separation velocity in the Hubble flow: $v_{\rm Hubble} = H_{z=0.3} \times d_{12} \simeq 70\,{\rm km/s}$, where $H_z \simeq H_0(1+z)\sqrt{1+\Omega_m z}$ and $H_0 \equiv 100h$ km/s/Mpc is the Hubble parameter at $z = 0$ with $h \simeq 0.7$. However the relative velocity of the two dark matter (DM) peaks does not necessarily correspond to the shock front velocity of the baryons observed in X-rays, and a lower estimate of $v_{12} \simeq 3000\,{\rm km/s}$ was given in Ref. [135].

Recent hydrodynamical simulations indeed show that the morphology (DM and gas) of the Bullet system is well reproduced by requiring $v_{12} \simeq 3000\,{\rm km/s}$ and $d_{12} \simeq 2.5\,{\rm Mpc}/h$ between the DM halos at redshift $z = 0.5$ [136, 137]. This is broadly comparable to Ref. [138] which had estimated earlier: $v_{12} \simeq 3200\,{\rm km/s}$ at $d_{12} \simeq 2.5\,{\rm Mpc}/h$. Simpler hydrodynamical simulations done earlier [139,140] had also found a lower relative velocity to reproduce the morphology better. The extreme properties of 1E 0657-56 can now be framed in terms of these initial conditions required to produce the observed collision.

[1] Listed on `http://www.mergingclustercollaboration.org/`

Searching for Bullet-like systems satisfying these initial conditions in N-Body simulations is convenient as the two clusters can be taken to be well separated and are thus easily identified. However because of its rarity the Bullet system can only be found in the largest N-Body simulations, provided the mass resolution is good (i.e. the DM 'particle' mass is small). Ref. [141] shows that to find a Bullet-like system, the volume of the simulation needs to be at least $\sim (4.5\,\mathrm{Gpc}/h)^3$, with the mass resolution better than $M_{\mathrm{par}} \sim 6.5 \times 10^{11} M_\odot/h$.

Various definitions of what constitutes a Bullet-like system have been employed. Ref. [142] used a $0.5\,(\mathrm{Gpc}/h)^3$ simulation and looked at the most massive subclusters moving away from the host cluster with velocity $> 4500\,\mathrm{km/s}$ and a separation $> 0.7\,\mathrm{Mpc}/h$ at redshift $z = 0.3$. With such a small simulation volume they did not find any host halo as massive as 1E 0657-56 so needed to extrapolate to find the fraction of appropriate subclusters. They estimated this to be ~ 0.01, however this is uncertain to at least an order of magnitude.

Ref. [143] used a $(3\,\mathrm{Gpc}/h)^3$ simulation with $M_{\mathrm{par}} \sim 2.3 \times 10^{11} M_\odot/h$ to look at the fraction of subhalos with high enough velocity among systems satisfying the conditions in Ref. [138]. This fraction, dubbed 'probability', was found to be about 10^{-10} at $z = 0$, by fitting a Gaussian to the pairwise velocity distribution in order to estimate the tail of the distribution. This was interpreted as an inconsistency between ΛCDM and the observation of 1E 0657-56.

Ref. [141] studied the effect of the box size and the resolution on the tail of the pairwise velocity distribution and found that simulations with small boxes and poor resolution struggle to produce systems as extreme as 1E 0657-56. Using rather different definitions for a Bullet-like system than Refs. [142] and [143] they estimated the fraction of systems with high enough relative velocity by fitting a skewed Gaussian to the pairwise velocity distribution. Again dubbed 'probability', this was estimated to be $\sim 10^{-8}$, still very inconsistent with ΛCDM.

Ref. [144] used a large simulation with volume of $(21\,\mathrm{Gpc}/h)^3$ but poor resolution $M_{\mathrm{par}} \sim 1.2 \times 10^{12} M_\odot/h$. They also used a different percolation parameter ($b = 0.15$ instead of the conventional $b = 0.2$) in their Friend of Friends (FoF) halo finder, arguing that this more faithfully reconstructs the masses of halos corresponding to the Bullet

system. The tail of the pairwise velocity distribution was analysed in the Extreme Value Statistics (EVS) approach to show that it is significantly fatter than a Gaussian-like tail. Using a similar definition for Bullet-like systems as Ref. [141] they found that the fraction (again called 'probability') of such high-velocity encounters is about $\sim 6 \times 10^{-6}$, again raising a problem for ΛCDM.

Ref. [145] explored the effect of halo finders on the pairwise velocity distribution. In particular, a configuration-space based FoF algorithm was compared to ROCKSTAR [45], a phase-space based halo finder. Using the same definition for a Bullet-like system as in Ref. [141], it was found that the FoF halo finder fails to identify the collisions in the high-velocity tail and leads to 'probabilities' almost two orders of magnitude lower that when the better performing ROCKSTAR halo finder is used.

Finally Ref. [146] used a $(6\,\mathrm{Gpc}/h)^3$ volume with $M_{\mathrm{par}} \sim 7.5 \times 10^{11} M_\odot/h$ and argued that a Bullet-like system [139] at $z = 0.3$ is not too far from other halo pairs in the simulation. Instead of focussing on the extreme properties of colliding dark matter halos, Ref. [147] looked at the morphology of the gas and dark matter in the colliding clusters and found that the displacement between the gas and dark matter similar to 1E 0657-56 is expected in about 1% of the clusters. Some other investigations [135, 144, 148] have even considered whether the apparent inconsistency posed by the Bullet Cluster can be alleviated by invoking a new long range 'fifth' force in the 'dark sector'. Rather than engage in such speculations we address in this chapter the main shortcoming of the previous studies, viz. the ill-defined 'probability' of finding systems like 1E 0657-56 on the sky.

It is not unexpected to finds deviations or 'anomalies' in a rich dataset. Care must be taken when analysing data and looking for such rare events by making more and more narrow after-the-fact (a posteriori) choices which apparently amplify the significance of those 'anomalies'. However, the highly unlikely events are a useful guide and motivation for new theories or models. We alleviate the aforementioned issues by not studying the probabilities of finding a Bullet-like system but the expected number of such systems on the sky as well as providing a generic formula for the expected number of mergers for a range of parameters describing them.

We use Dark Sky Simulations [44], one of the biggest N-Body simulations with vol-

ume $(8\,\mathrm{Gpc}/h)^3$, as well as one of the best resolutions $M_{\mathrm{par}} \sim 3.9 \times 10^{10} M_{\odot}/h$. The halo catalogue used was produced by a phase-space based (ROCKSTAR) halo finder that performs better than the configuration-space based finders used earlier. We carefully explore the dependence of the pairwise velocity distribution on the different definitions of Bullet-like systems. Furthermore, the machinery of EVS is used to examine the tail of the distribution, rather than *assuming* that a Gaussian fit is a good description. We also study an observationally better motivated quantity, viz. the absolute number of bullet-like systems expected in a survey up to some particular redshift. This should be contrasted with the fraction of extreme objects (in a population of less extreme objects) that has been the focus of earlier studies.

In Sec. 4.2 we describe the N-Body simulation used and demonstrate the importance of using a phase-space based halo finder for searching for systems similar to 1E 0657-56. Sec. 4.3 summarises the EVS tools relevant for modelling the tails of distributions. In Sec. 4.4 we show how the expected number of Bullet-like systems can be estimated. We also discuss some of the paradoxical features of the 'probability' — defined as a fraction of Bullet-like systems in a population of candidate systems — that has been studied previously. Sec. 4.5 contains the main results of this chapter, viz. the expected number of systems similar to 1E 0657-56 in ΛCDM.

4.2 Simulations and halo finders

We use the biggest dataset of the Dark Sky Simulation (DS) Early Data Release [44] described in detail in Sec. 1.1.5. The simulation has a box of volume $(8\,\mathrm{Gpc}/h)^3$ with $N^3 = 10240^3$ 'dark matter particles' corresponding to $M_{\mathrm{par}} \sim 3.9 \times 10^{10} M_{\odot}/h$. Such a large volume and good resolution make it ideal for the study of rare objects like the Bullet Cluster [141].

Halos in the DS simulation were identified with the ROCKSTAR [45] halo finder. For computational convenience we reduced the halo catalogue by requiring $M_{\mathrm{halo}} > 3.5 \times 10^{13} M_{\odot}/h$. ROCKSTAR is a phase-space based halo finder and therefore performs better at identifying Bullet-like systems which are characterised by a small distance between the two massive clusters with a high relative velocity. Standard Friend of

Friend (FoF) halo finders work in configuration space and therefore struggle to tell the two nearby clusters apart — this leads to *underestimation* of the number of Bullet-like systems in N-Body simulations. In phase space however the host and the bullet clusters are well separated due to the high relative velocity, hence can be correctly identified as two separate clusters.

To illustrate this point, the host and the bullet halo are generated at the DS simulation resolution, using the NFW [149] density profile as it best fits weak lensing data on 1E 0657-56 [135]. The DM particles are given the velocities as in Ref. [150]. The two halos are placed at various distances with their relative velocity set at 3000 km/s. Then both ROCKSTAR and a FoF algorithm with percolation parameter $b = 0.2$ are used to extract the halo information. At separations of $5\,\mathrm{Mpc}/h$ and $4\,\mathrm{Mpc}/h$ both halo finders identify the two halos correctly. However at $3\,\mathrm{Mpc}/h$ the FoF algorithm identifies 2 halos only $\sim$30% of the time, while at $2\,\mathrm{Mpc}/h$ and below it identifies only 1. By contrast, ROCKSTAR finds 2 halos at all separations. Thus we expect a depletion of the number of nearby mergers when a FoF based halo finder is used, leading to underestimation of the number of objects similar to the Bullet system.

4.3 Extreme value statistics

Events in the tail of the pairwise velocity distribution need to be modelled without assuming a functional form for the underlying distribution and EVS provides a framework for doing so. We briefly outline the formalism relevant to this study following Ref. [151].

We are interested in modelling the statistical behaviour of extreme values of a random variable X. The probability that X exceeds a specified high threshold μ is:

$$\Pr\{X > \mu + x | X > \mu\} = \frac{1 - F(\mu + x)}{1 - F(\mu)} \tag{4.1}$$

Here $F(x) = \Pr\{X < x\}$ is the cumulative distribution function which is unknown and needs to be estimated.

The central result of EVS is that the maxima of a sequence of random variables $X_{\max} = \{X_1, ..., X_N\}$ with a common cumulative distribution function $F(x)$ tend to be distributed in the limit $N \to \infty$ according the Generalized Extreme Value distribution

$G(x)$:

$$\Pr\{X_{\max} < x\} = F_{X_1}(x) \times ... \times F_{X_N}(x) = F^N(x) \approx G(x) \tag{4.2}$$

where

$$G_{\mu,\sigma,\xi}(x) = \exp\left\{-\left[1+\xi\left(\frac{x-\mu}{\sigma}\right)\right]^{-1/\xi}\right\} \tag{4.3}$$

for some $\mu, \sigma > 0$ and ξ. From Eqs.(4.2) and (4.3) we can estimate $F(x)$ and thus approximate Eq.(4.1) by the Generalized Pareto Distribution (GPD) $H(x)$:

$$\Pr\{X > \mu + x | X > \mu\} = 1 - H_{\mu,\sigma,\xi}(x), \quad \text{where}: \quad H_{\mu,\sigma,\xi}(x) = 1 - \left[1+\xi\left(\frac{x-\mu}{\sigma}\right)\right]^{-1/\xi} \tag{4.4}$$

with the condition $1 + \xi\left((x-\mu)/\sigma\right) > 0$. The above expression is fitted to the extreme events and provides a model independent description of the tails of probability distributions. If the underlying distribution is 'Gaussian-like' (e.g. Gaussian or skewed Gaussian), the tail parameter ξ equals 0. Longer tails have $\xi > 0$ whereas shorter ones have $\xi < 0$.

The next step in modelling the tail is the choice of the threshold μ. If it is too low, the asymptotically valid GPD does not apply and our estimate will be biased. If μ is too high, the reduced number of extreme events available results in high variance in the estimated parameters. Provided the GPD description is valid above some threshold μ_1 then it is also valid for a higher threshold $\mu_2 > \mu_1$ with new parameters $(\mu_2, \sigma_{\mu_2}, \xi_{\mu_2})$. However, the tail parameter ξ_μ and the combination $\sigma_\mu - \mu\xi_\mu$ should remain constant. Therefore the simplest method for the appropriate choice of the threshold μ focusses on finding a region of stability of these parameter combinations. In order to minimise the variance, the *lowest* μ consistent with stability is chosen as the threshold.

4.4 The number (versus 'probability') of Bullet-like systems

A Bullet-like system can be defined by cuts in the collisional parameters describing the merger of two clusters. Such a definition is particularly suited for the DM-only N-Body simulations. The collisional parameters are the separation d_{12} between the two halos, the two masses m_1 and m_2, the relative speed v_{12}, and the angle θ between the relative

velocity and the separation. To simplify the problem the mass cut is often made in terms of the average mass $\langle M \rangle$ of the two halos and we shall do so too.

The most prominent feature of 1E 0657-56 is the high relative velocity of its subcluster with respect to the main cluster. Thus both the pairwise velocity distribution $\mathrm{d}n/\mathrm{d}v_{12}$ and its cumulative $n(> v_{12})$ (where n is the number density of the halo pairs) will be studied.

The observationally relevant quantity is the expected number of Bullet-like objects up to some redshift. However, the quantity studied so far has been the fraction of such objects with respect to less extreme candidate systems (i.e. having a lower relative velocity) [141–145]. This fraction is then interpreted as the 'probability' of finding a Bullet-like system although it is not directly related to the likelihood of observing such an object on the sky. In terms of the number densities it is expressed as $p_v = n(v_{12} > v_{\mathrm{Bullet}} \mid \text{other cuts})/n(v_{12} > 0 \mid \text{other cuts})$. The probability defined in this way is relative to the objects defined by the initial mass, distance, and angle cuts and has a non-trivial and sometimes paradoxical dependence on those cuts. For example, increasing the mass cut in the definition of a Bullet-like system leads to an increase in the 'probability', even though the actual number of systems has been *reduced* drastically (see Figs. 4.2-4.3).

Alternatively, the high masses of the two colliding clusters can be taken as the main defining parameters and the 'probability' written as $p_m = n(m_1, m_2 > M_{\mathrm{main}}, M_{\mathrm{Bullet}} \mid \text{other cuts})/n(m_1, m_2 > 0 \mid \text{other cuts})$, where the relative velocity cut has now been taken before the mass cut. Even though we are looking at the *same* Bullet-like objects, one finds $p_v \neq p_m$ simply due to the different order of the cuts taken in the collisional parameters.

In what follows we focus therefore on the observationally motivated and intuitively accessible quantity, viz. the expected number of Bullet-like systems on the sky up to a specified redshift. This can be expressed (in a flat universe) as:

$$N(< z) = \int_0^z n(v_{12} > v_{\mathrm{Bullet}}, \mathrm{cuts} \mid z') 4\pi D_{\mathrm{c}}^2(z')\, \mathrm{d}D_{\mathrm{c}}(z'), \tag{4.5}$$

where $n(v_{12} > v_{\mathrm{Bullet}}, \mathrm{cuts} \mid z)$ is the comoving number density of Bullet-like objects at redshift z, and $D_{\mathrm{c}}(z)$ is the comoving distance to z.

Estimating the pairwise velocity function $\mathrm{d}n/\mathrm{d}v_{12}$ and its cumulative version $n(>$

v_{12}) in large simulations at many different redshifts can be computationally expensive. However, $\mathrm{d}n/\mathrm{d}v_{12}$, and consequently $n(>v_{12})$, were found to have a stable shape up to $z \sim 0.5$ [141, 144]. This simplifies the analysis and we can approximate:

$$n(v_{12} > v_{\rm Bullet}, \text{cuts} \mid z) \approx \alpha(z) \times n(v_{12} > v_{\rm Bullet}, \text{cuts} \mid z = 0), \tag{4.6}$$

where the normalisation $\alpha(z)$ is proportional to the number of pairs of halos satisfying specific cuts (mass, distance ...) and is set equal to 1 at $z = 0$. When one halo has a mass above m_1 and the other above m_2, with their separation less than d_{12}, it can be written as:

$$\alpha(z) \propto \iiint_{m_1,m_2,0}^{\infty,\infty,d_{12}} \left.\frac{\mathrm{d}n_{\rm h}}{\mathrm{d}m_1'}\right|_z \left.\frac{\mathrm{d}n_{\rm h}}{\mathrm{d}m_2'}\right|_z [1 + \xi_{\rm hh}(r, m_1', m_2', z)]\, 4\pi r^2 \mathrm{d}r\, \mathrm{d}m_2'\, \mathrm{d}m_1', \tag{4.7}$$

where $(\mathrm{d}n_{\rm h}/\mathrm{d}m)|_z$ is the halo mass function at redshift z and $\xi_{\rm hh}(r, m_1, m_2, z)$ is the two-point correlation function of halos of mass m_1 and m_2 which is conventionally expressed as $b(m_1, r, z)b(m_2, r, z)\xi_{\rm lin}(r, z)$ in terms of the halo bias b (which includes the non-linear correction). Non-trivial mass cuts are simply implemented by including an appropriate window function in Eq.(4.7).

Our semi-analytical expression (4.7) provides an excellent description of N-body simulations as illustrated in Fig.4.1. We use a DEUSS-Lambda [152] N-Body simulation (containing 2048^3 particles in a $(2592\,\mathrm{Mpc}/h)^3$ volume, using a FoF halo finder) that is small enough to be analysed at several redshifts. We have used the halo mass function from Ref. [153], the power-spectrum from CAMB (`http://camb.info`), and the best-fit halo bias formula from Ref. [154] in the expression (4.7). The normalisation $\alpha(z)$ is extracted by taking the ratio $n(>v_{12} = 0|z)/n(>v_{12} = 0|z = 0)$ which is then compared to the value from Eqs.(4.6-4.7). Fig.4.1 shows that our semi-analytic model becomes less accurate at high redshifts, high masses and small distances as is expected. Bigger simulations are required to explore these extreme regions in parameter space.

From Eqs. (4.5-4.7) it then follows that the number of Bullet-like systems factorises as:

$$N(<z) \approx n(v_{12} > v_{\rm Bullet}, \text{cuts} \mid z = 0) \times V_{\rm eff}(z), \tag{4.8}$$

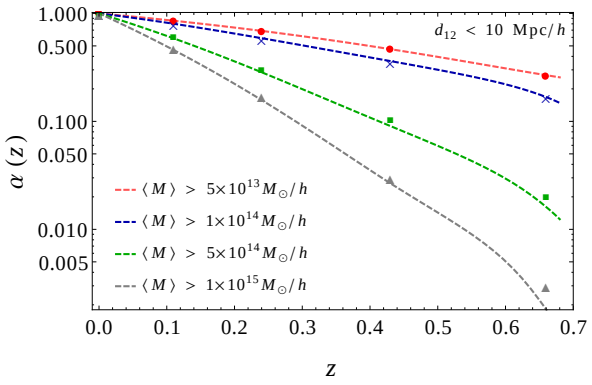

(a) The normalisation $\alpha(z)$ from Eq.(4.7) for various mass cuts, compared to simulation 'data'.

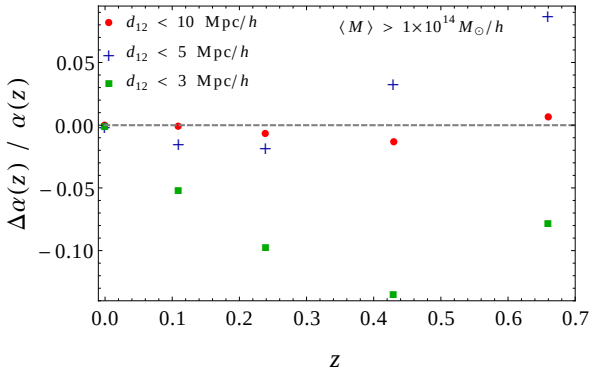

(b) The fractional difference in $\alpha(z)$ between the value extracted from the simulation and calculated using Eq.(4.7), for different separation cuts.

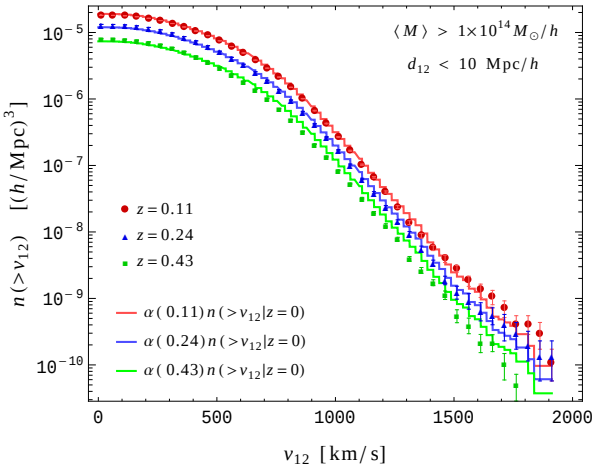

(c) Simulated 'data' on cumulative pairwise velocity distribution at various redshifts, compared to the approximation (4.6). Errors shown are estimated by bootstrapping.

Figure 4.1: Testing our semi-analytic model (4.6–4.7) against the DEUSS-Lambda N-Body simulation.

where:

$$V_{\rm eff}(z) = \int_0^z \alpha(z')4\pi D_c^2(z')\,{\rm d}D_{\rm c}(z'). \tag{4.9}$$

Therefore, the pairwise velocity distribution can be studied at $z = 0$ in simulation outputs, provided we can estimate (either semi-analytically as in Eq.(4.7), or from a set of smaller N-Body simulations) the effective volume $V_{\rm eff}$. This simplification is valid in the observationally interesting redshift range $z < 1$.

Given that $V_{\rm eff}$ is big enough (such that the clustering of objects of interest is negligible), we can treat $N(< z)$ as being Poisson distributed. Then the probability that we see at least one object up to redshift z is just: $\Pr\{N \geq 1\} = 1 - \text{Poisson}\{N = 0 \mid \langle N\rangle = N(< z)\}$.

4.5 Results

Now we study the high-velocity tail of the pairwise velocity distribution, in particular its dependence on the collisional parameters — the average mass, the relative distance, the collisional angle, and the relative velocity of the halo pairs — and the correlations among these. The relative velocity of halo pairs, v_{12}, is considered in *proper* coordinates, i.e. including the Hubble flow term $\mathbf{v}_{\rm H} = H\mathbf{d}_{12}$. Using Eq.(4.6) we analyse the output of the N-Body simulation (Sec. 5.2) at redshift $z = 0$.

Increasing the cut in the average mass $\langle M\rangle$ of the halo pairs, while keeping other collisional parameters (in particular v_{12}) unchanged, the number density of the halo pairs *decreases* as seen in Fig. 4.2. By contrast, if we chose to normalise the velocity distribution for each mass cut (as is done in Refs. [141–145]), we would conclude that the 'probability', i.e. the fraction of the high-velocity collisions, increases (see Fig. 4.3).

In Newtonian gravity, for a bound system with mass m we expect $v_{12} \propto \sqrt{m}$. Therefore more massive halo pairs are likely to have a higher relative velocity. Indeed in Fig. 4.2 the tail of the low-$\langle M\rangle$ velocity distribution converges to the high-$\langle M\rangle$ tail at large relative velocities, indicating that the tail of the pairwise velocity distribution consists mostly of very massive halos. This is also seen in the mass distribution of halo pairs in the high-velocity tail (see Fig. 4.4). Therefore, small N-Body simulations that

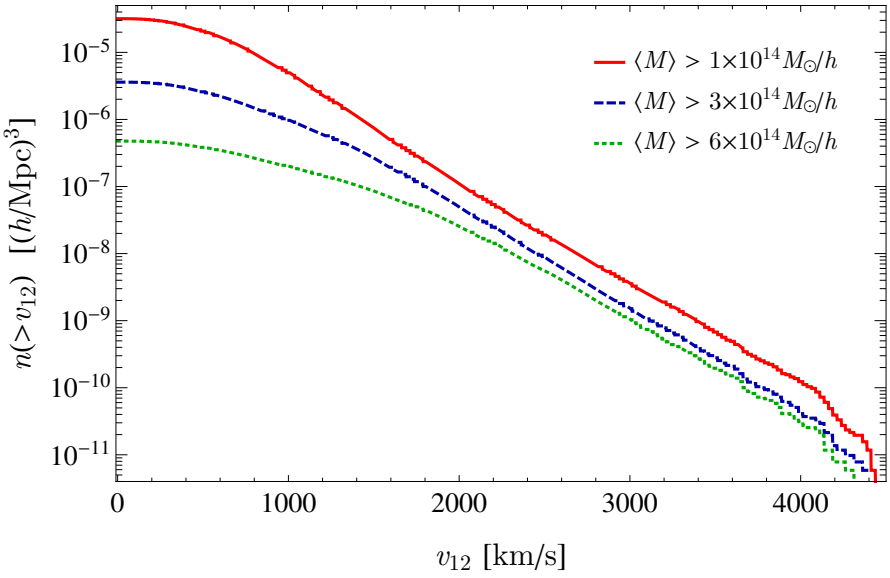

Figure 4.2: The dependence of the cumulative pairwise velocity distribution on the average mass $\langle M\rangle$ of the halo pairs. The halo mass function is steeply descending with $\langle M\rangle$, and so is the total number density of halo pairs, $n(> v_{12} = 0|\langle M\rangle)$.

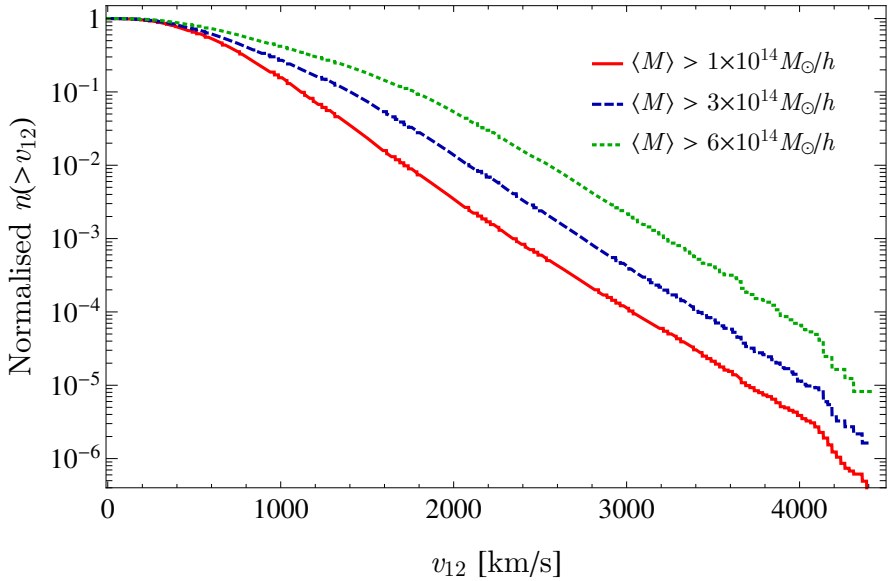

Figure 4.3: The cumulative pairwise velocity distribution normalised separately for each cut in the average mass. In the set of more massive halos, the fraction of higher relative velocity pairs is bigger. Naïvely this would be interpreted as a higher probability, however Fig. 4.2 shows that the absolute number density of more massive halos pairs *decreases* with $\langle M\rangle$.

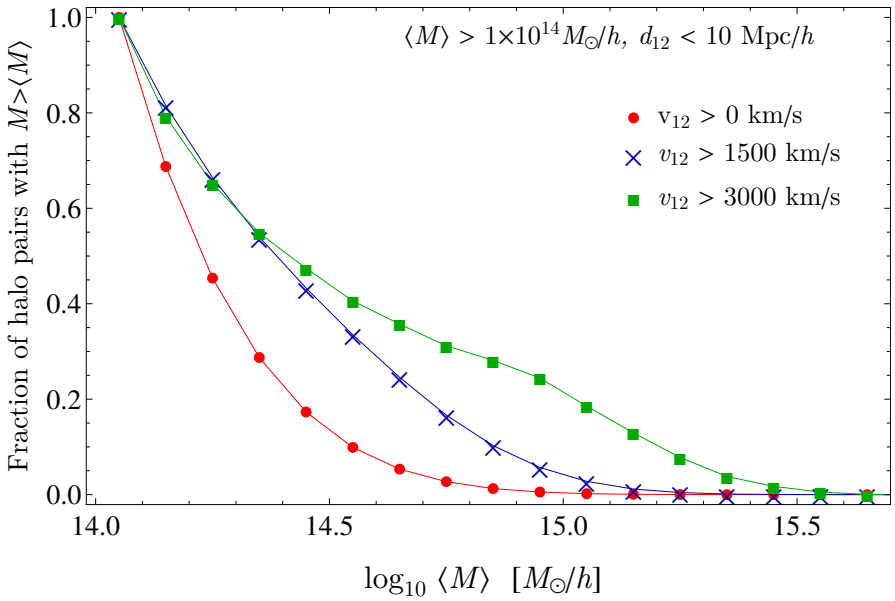

Figure 4.4: The fraction of halo pairs above a specified average mass $\langle M\rangle$, given the relative velocity v_{12}. The fraction of high-mass halo pairs is *higher* in the high-velocity population. Here $\langle M\rangle > 10^{14} M_\odot/h$ and $d_{12} < 10\,\mathrm{Mpc/h}$.

fail to produce halos with high masses *underestimate* the tail of the pairwise velocity distribution.

The next collisional parameter we examine is the angle θ between the separation and the relative velocity of a halo pair. In Fig. 4.5 we see that the tail of the velocity distribution consists almost entirely of the halo pairs approaching each other ($\cos\theta < 0$). However, the number density of colliding halo pairs is not as sensitive to cuts in the angle as to the cuts in the halo masses. Again, as expected from Newtonian gravity, halo collisions with high relative velocity are more likely to be approximately head-on, as seen in Fig. 4.6.

In Fig. 4.7 we see that the halo pairs with a high relative velocity are more likely to be *closer* together compared to the low pairwise velocity. Therefore, a configuration-space based halo finder (e.g. FoF) will miss relatively more high velocity mergers compared to the low velocity ones, and hence bias the tail of the pairwise velocity distribution to be shorter. This characteristic of the halo finders has been explored in greater detail in Ref. [145]. The fact that the high relative velocity halo pairs are closer together is expected since high velocities are generated through gravitational attraction that also brings the halos closer together.

We have shown above that the number of Bullet-like systems has a non-trivial de-

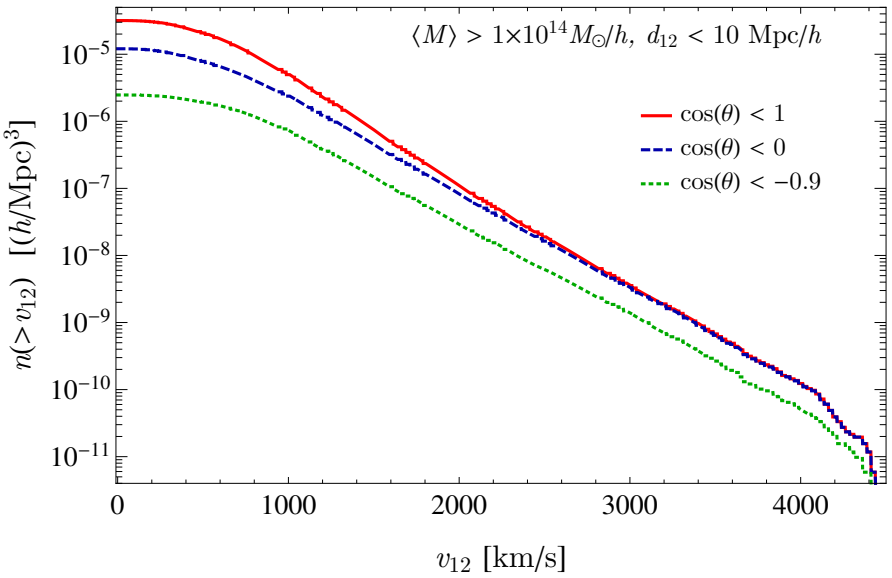

Figure 4.5: Cumulative pairwise velocity distribution for different cuts on the collisional angle θ, taking $\langle M\rangle > 10^{14} M_\odot/h$ and $d_{12} < 10\,\mathrm{Mpc/h}$. Note that the high-velocity tail consists almost entirely of halos moving *towards* each other ($\cos\theta < 0$).

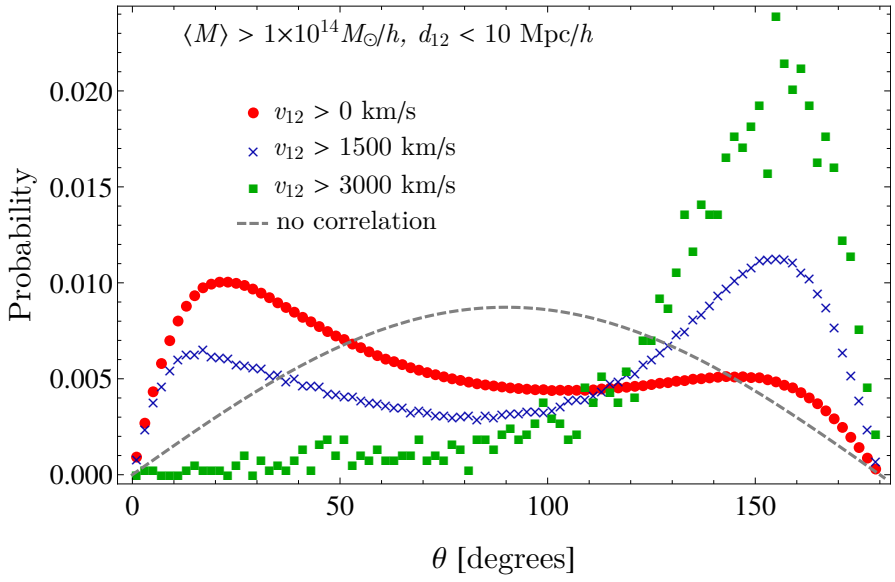

Figure 4.6: The probability distribution for the collisional angle θ given the relative velocity v_{12}, taking $\langle M\rangle > 10^{14} M_\odot/h$ and $d_{12} < 10\,\mathrm{Mpc/h}$. Small relative velocities are mainly associated with the Hubble flow, $\theta \sim 0°$, whereas high velocities are mainly head-on collisions, $\theta \simeq 180°$. The dashed line shows the case when the separation vector and the relative velocity vector are uncorrelated.

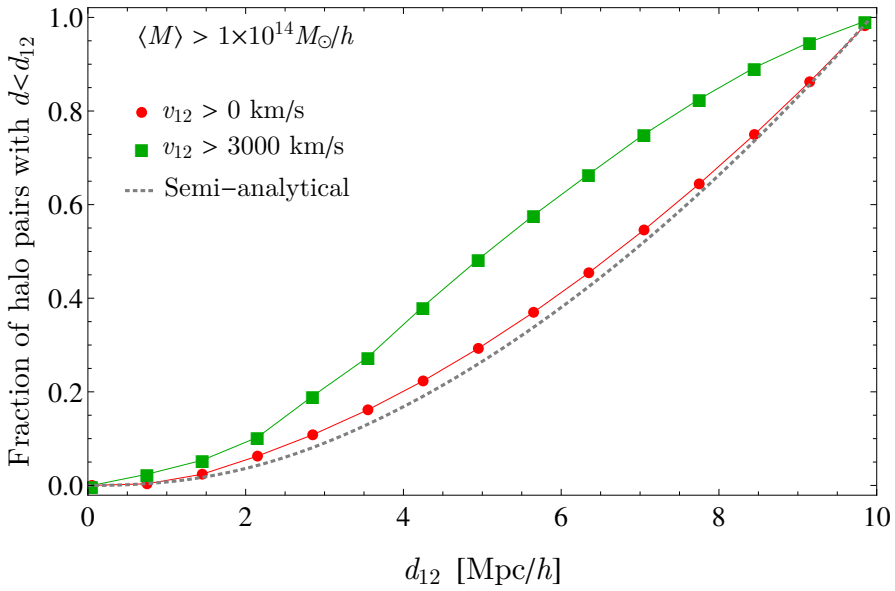

Figure 4.7: The fraction of halo pairs below a specified separation, given some relative velocity. For high-velocity collisions the halos are closer than for low pairwise velocities. The dashed line is the semi-analytical expectation for $v_{12} > 0\,\mathrm{km/s}$, calculated using Eq.(4.7) with the cosmological parameters matching the Dark Sky simulation.

pendence on the collisional parameters, which are moreover *correlated* with each other. Therefore, the expected number of Bullet-like systems depends strongly on the adopted definition of such a system. A conservative (i.e. *over*-) estimate of the number of Bullet-like systems within a cosmic volume up to some redshift can be obtained by choosing cuts in the collisional parameters that are less extreme than those characterising 1E 0657-56. Accordingly, we adopt the following conditions on the average mass, separation, and the relative velocity of the halo pairs: $\langle M \rangle > 10^{14} M_\odot/h$, $d_{12} \leq 10\,\mathrm{Mpc/h}$, and $v_{12} > 3000\,\mathrm{km/s}$. This is comparable to the cuts made in Refs. [144] and [141]. Any additional cuts in the separation and the angle reduce the number of Bullet-like objects, thus *exacerbating* any tension of ΛCDM with observations. The pairwise velocity distribution and its cumulative version are shown in Figs. 4.8 and 4.9, where the errorbars have been estimated by a bootstrap technique[2]. We fit the tail to the GPD form using the maximum likelihood method. The stability analysis is presented in Fig. 4.10. The appropriate choice for the threshold μ is around 1900 km/s; below this the events in the distribution are normal while above this threshold the variance increases substantially and the bias due to the finite simulation box appears (i.e. very rare events are missing

[2]Specifically, we randomly sample subsamples from the simulation data and then use the dispersion in the set of subsamples as an indication of the error.

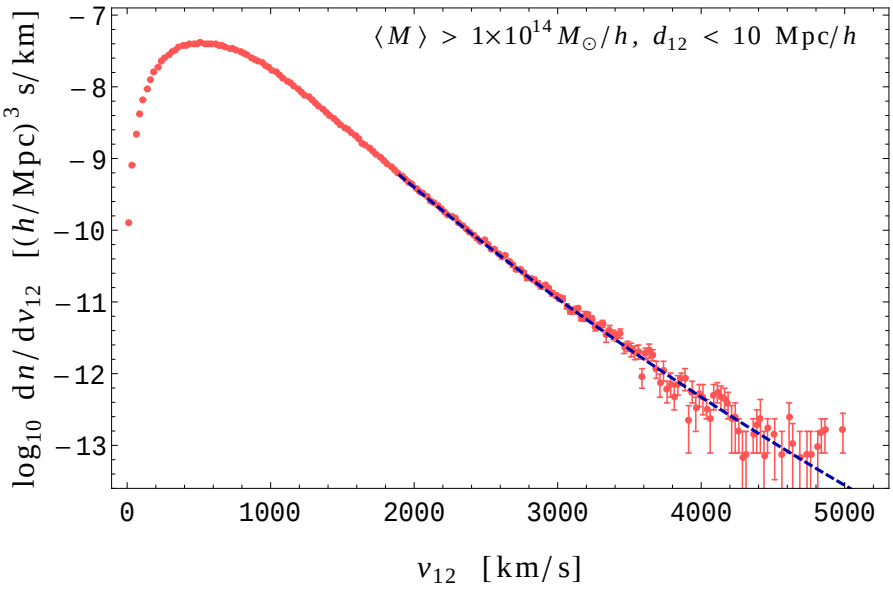

Figure 4.8: Pairwise velocity distribution from the simulation at redshift $z = 0$ compared to the best fit Generalised Pareto Distribution.

altogether). Therefore the tail of the pairwise velocity distribution is well characterised by: $\mu \simeq 1900\,\mathrm{km/s}$, $\xi = 0.038 \pm 0.003$ and $\sigma = 268.0 \pm 1.4\,\mathrm{km/s}$. This is broadly consistent with the results of Ref. [144]. Thus the extreme events in the tail of the pairwise velocity distribution are *not* drawn from a Gaussian-like distribution ($\xi = 0$) as has been assumed previously [141, 143, 145].

We calculate the expected number of Bullet-like systems as defined above ($\langle M \rangle > 10^{14} M_\odot/h, d_{12} \leq 10\,\mathrm{Mpc}/h$, and $v_{12} > 3000\,\mathrm{km/s}$) up to $z = 0.3$ (where 1E 0657-56 is located) and $z = 0.5$ (where the initial conditions for the collision are known). The corresponding effective volumes from Eq. (4.9) are $V_{\mathrm{eff}}(< z = 0.3) \simeq 4.6\,(\mathrm{Gpc}/h)^3$ and $V_{\mathrm{eff}}(< z = 0.5) \simeq 13\,(\mathrm{Gpc}/h)^3$. Using this and the cumulative pairwise velocity distribution, the expected number of Bullet-like systems is:

$$N(< z = 0.3) \simeq 17^{+6}_{-5}, \text{ and } N(< z = 0.5) \simeq 47^{+8}_{-7}, \tag{4.10}$$

where the variance has been estimated by sampling the subvolumes of size V_{eff} from the full N-Body simulation.

We now focus on the expected number of objects as or more extreme than 1E 0657-56

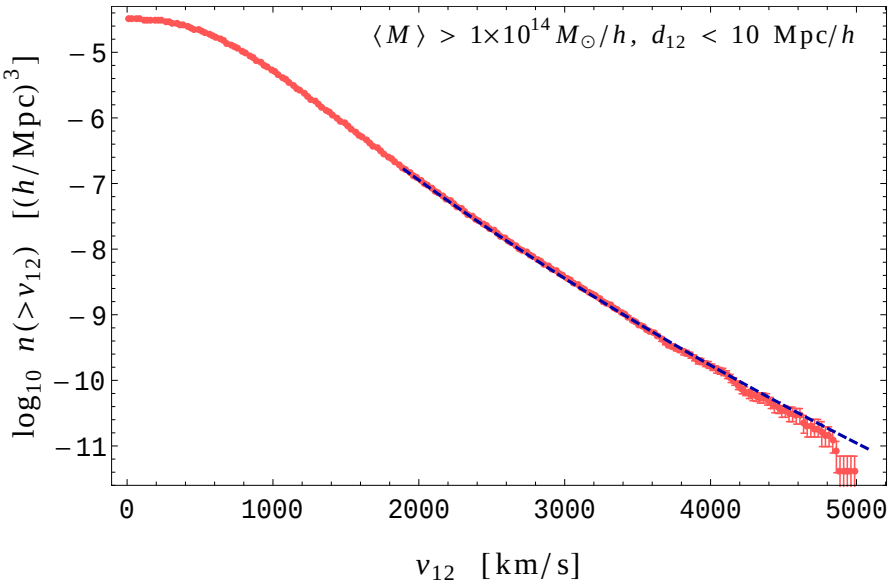

Figure 4.9: Cumulative pairwise velocity distribution from the simulation at redshift $z = 0$ compared to the best fit Generalised Pareto Distribution.

in particular. Making cuts in the collisional parameters similar to Ref. [145]:

$$\langle M\rangle > (M_{\rm main} + M_{\rm Bullet})/2 = 5.67\times 10^{14} M_\odot/h, \qquad M_{1,2} > 10^{14} M_\odot/h,$$
$$d_{12} \leq 10\,{\rm Mpc}/h, \qquad v_{12} > 3000\,{\rm km/s}, \tag{4.11}$$

we obtain:

$$N(<z=0.3) \simeq 1.3^{+2.0}_{-0.6} \quad \text{and} \quad N(<z=0.5) \simeq 2.5^{+2.1}_{-1.2}, \tag{4.12}$$

However since 1E 0657-56 is observed shortly *after* the collision we should require further that the halo pairs must be moving away from each other, i.e. $\cos\theta > 0$. This leads to:

$$N(<z=0.3) \simeq 0.1 \quad \text{and} \quad N(<z=0.5) \simeq 0.15 \tag{4.13}$$

Since the pairwise velocity distribution is steeply descending, increasing the relative velocity v_{12} up to the 4500 km/s velocity of the shock front in the 1E 0657-56 merger would *decrease* this number further by two orders of magnitude, as we see from Fig. 4.2.

About a dozen other merging clusters have been observed, each with a different set of collisional parameters. Since a cluster collision is expected to take a short time compared to the cosmic time we can consider events both before and after collision by setting $\cos\theta < -0.9$ or $\cos\theta > 0.9$. Requiring $v_{12} \geq 4000\,{\rm km/s}$ in addition to the mass cuts in Eq.(4.11), we find only 4 halo pairs in the full (Hubble) volume of the simulation (see Table 4.1). Hence, the expected number of such systems is $\langle N\rangle(<z=0.3) \simeq 0.02$,

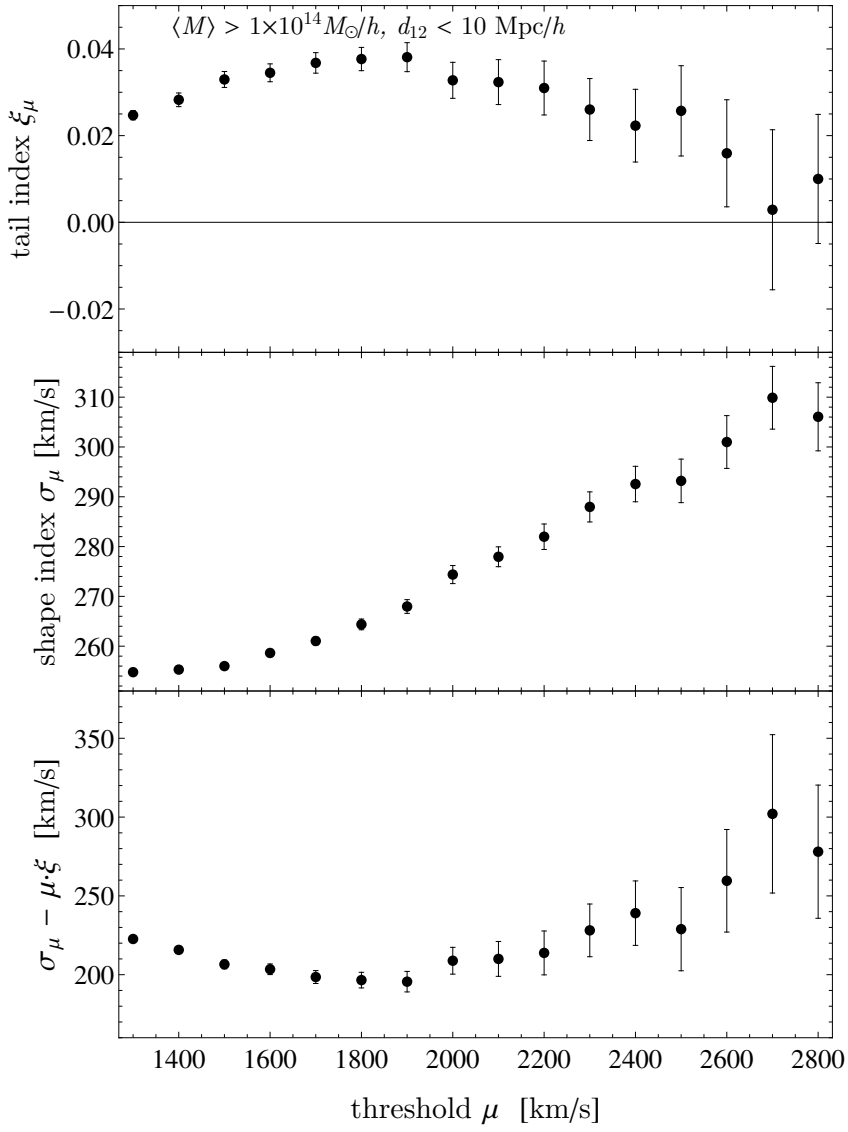

Figure 4.10: Stability plots for the EVS tail fitting exercise. The most appropriate threshold μ is seen to be around 1900 km/s where ξ_μ is approximately constant and σ_μ increases linearly.

$M_1\,[M_\odot/h]$	$M_2\,[M_\odot/h]$	d_{12} [Mpc/h]	v_{12} [km/s]	$\cos\theta$
1.73×10^{15}	1.1×10^{14}	6.9	4262	−0.99
3.11×10^{15}	1.2×10^{14}	8.3	4140	−0.96
3.0×10^{15}	1.3×10^{14}	2.7	4121	−0.93
3.8×10^{15}	1.4×10^{14}	3.5	4132	−0.94

Table 4.1: Colliding halo pairs with the mass cuts from Eq.(4.11) and $v_{12} > 4000$ km/s in the $(8\,\mathrm{Gpc}/h)^3$ Dark Sky simulation. All collisions are selected to be head-on ($|\cos\theta| > 0.9$).

leading to the probability, $p(N \geq 1) = 1 - \mathrm{Poisson}(N = 0 \mid \langle N \rangle = 0.02) \simeq 0.02$, of having at least one such system in a cosmic volume up to redshift $z = 0.3$. Furthermore, setting $v_{12} \geq 4500\,\mathrm{km/s}$ we find *no* candidate halo pairs. This places an upper limit of 0.005 on the probability $p(N \geq 1)$ of having at least one system with such an extreme relative velocity up to $z = 0.3$.

For observers, an approximate formula for the number of colliding clusters expected up to a specified redshift, given specific collisional parameters, might be of interest:

$$N(<z;\ <d_{12};\ >v_{12};\ >\langle M\rangle;\ >\cos\theta) \approx A\langle M\rangle^a d_{12}^b z^c (1-\cos\theta)^d \times \\ \exp\left[\alpha \times (d_{12}/\langle M\rangle) + \cos^2\theta(\beta + \gamma \times \langle M\rangle + \delta \times v_{12}) + v_{12}(\epsilon + \zeta \times d_{12}) + \eta \times \langle M\rangle z\right], \tag{4.14}$$

where $(A, a, b, c, d, \alpha, \beta, \gamma, \delta, \epsilon, \zeta, \eta) = (80.7\times10^3, 0.26, 0.93, 2.78, 1.44, 0.22, 1.15, -0.071, 2.50\times 10^{-4}, -3.43\times10^{-3}, -4.82\times10^{-5}, -0.58)$. Our fit is valid to within 10% for $10^{14}M_\odot/h \lesssim \langle M\rangle \lesssim 7\times10^{14}M_\odot/h$, $z < 0.6$, $3\,\mathrm{Mpc}/h \lesssim d_{12} \lesssim 10\,\mathrm{Mpc}/h$, $\cos\theta \lesssim 0.9$, and $2000\,\mathrm{km/s} \lesssim v_{12} \lesssim 4000\,\mathrm{km/s}$. However it becomes unreliable at higher velocities and masses, as well as at lower separations. The effective volumes (4.9) used in the expression (4.14) above are in fact estimated from a set of smaller simulations [152].

4.6 Summary

In this chapter we have studied the prevalence of rare DM halo collisions in ΛCDM cosmology using the pairwise velocity distribution for halos extracted from a N-body simulation with volume comparable to the observable universe and the finest resolution to date. Our approach differs from previous studies that have attempted to quantify the probability that a cluster and its subcluster, given some masses and separation, will have a relative velocity as high as 1E 0657-56. We find that such a definition of probability can lead to paradoxical conclusions, so instead we investigate the dependence of the expected *number* of Bullet-like systems on the collisional parameters, as well as the correlations among them. We demonstrate that the expected number of halo pairs is very sensitive to cuts in the parameters defining the mergers. Given recent observations of more merging clusters, we provide a formula for the expected number of halo-halo

collisions with specified collisional parameters up to some redshift.

The tail of the pairwise velocity distribution for the colliding halos is modelled using Extreme Values Statistics to demonstrate that it is fatter than a Gaussian. Hence, the combination of a configuration-space based halo finder, the assumption of a Gaussian-like tail, small simulation boxes, and poor simulation resolutions, have resulted in *underestimation* of the number of high-velocity mergers in previous studies.

We find that only about 0.1 systems like the Bullet Cluster 1E 0657-56 (where the collision has occurred *already*) can be expected up to $z = 0.3$. Increasing the relative velocity to 4500 km/s — the shock front velocity deduced from X-ray observations of 1E 0657-56 — *no* candidate systems are found in the simulation. Thus the existence of 1E 0657-56 is only marginally compatible with the ΛCDM cosmology, even if the relative velocity of the two colliding clusters is at the lowest value suggested by hydrodynamical simulations. Hence if more such systems are found this would challenge the standard cosmological model.

Chapter 5: Frames of most uniform Hubble Flow

5.1 Introduction

The standard Lambda Cold Dark Matter (ΛCDM) cosmological model is based on an assumed background Friedmann-Lemaître-Robertson-Walker (FLRW) geometry that is isotropic and homogeneous. The structure in the universe is modelled as statistically isotropic and homogeneous, initially Gaussian distributed perturbations to this background. This would result in some scatter in the Hubble diagram due to local 'peculiar' (non-Hubble) velocities. The cosmic rest frame is defined by comoving observers in the FLRW background and the Cosmic Microwave Background (CMB) frame is conventionally taken to correspond to this 'standard of rest' in which both the leading order linear Hubble law and peculiar velocities are defined. The observed dipole pattern in the CMB is then interpreted as due to our peculiar velocity with respect to the cosmic rest frame.

For an ensemble of observers, the frame where the velocity flow around an average observer is most uniform corresponds to the CMB frame. However, for a particular observer, the most uniform flow may well be in a frame boosted with respect to the CMB. In this chapter we are primarily concerned with the reference frame wherein the Hubble parameter in successive radial shells converges most quickly to the background value. We call this the 'minimum Hubble variation frame' or frame with most uniform Hubble flow.

The authors of Refs. [77, 155] looked for a different standard of rest based on the uniformity of the Hubble flow. They found that the Hubble parameter averaged in radial shells converges quickest to its background value in a frame that is boosted with respect to the CMB frame and corresponds roughly to the frame of the Local Group (LG) of galaxies. Moreover, they found that the dipole structure of the velocity flow persists in the CMB frame at large distances, contrary to expectation, but is smaller after boosting to the LG frame. Both of these observations make the local universe as seen in the boosted LG frame closer to the usual (ΛCDM) expectation. It was suggested [155] that the velocity of the minimum Hubble variation frame should correspond roughly to

the group velocity of the 'finite infinity' region [156–158]. Ref. [159] continued the study of the Hubble flow anisotropy with emphasis on the non-kinematic differential expansion of space as the origin of (at least a part) of the CMB dipole. Note that this general relativistic effect where the Hubble parameter is both a function of space and time is *not* captured in N-Body simulations where by construction there is a single background expansion rate.

These studies [77, 155, 159] were in part motivated by some analyses of the local bulk flow of galaxies (as measured in the CMB frame) which show a lack of convergence to the CMB frame even beyond ~ 100 Mpc [160–170], as would be the naïve expectation if the universe is indeed homogeneous on larger scales as inferred from galaxy counts in the SDSS [171] and WiggleZ [172] surveys. Other authors have used different methods (and data) to argue however that observed bulk flows are *consistent* with ΛCDM [173–182]. The situation is rather confusing e.g. Ref. [167] showed using 165 SNe Ia with redshift $z \lesssim 0.1$ in the Union 2 catalogue that there is an anomalously high and apparently constant bulk flow of ~ 250 km/s extending out to the Shapely supercluster at $z \simeq 0.06$ (~ 260 Mpc). This was *confirmed* using 117 new SNe Ia from the Nearby Supernova Factory survey and it was shown that the flow extends out beyond Shapely, nevertheless these authors concluded that their finding is in agreement with ΛCDM [182]. SNe Ia catalogues do have rather incomplete distributions on the sky which can bias the result, however the discrepancy with the standard expectation was also confirmed by analysis of the 6dF galaxy redshift survey which is the largest, most homogeneously derived peculiar velocity sample to date [168].

The variance of the Hubble parameter can be calculated in linear perturbation theory (e.g. Ref. [72]) or using N-Body simulations (e.g. Ref. [73]). In the latter study the dependence of the local Hubble parameter on the observer's environment (i.e. halos versus voids) was explored and it was found, as expected, that in voids the local value of the Hubble parameter is biased towards higher values while the opposite is true for observers in halos. Given the evidence that we are located in a large under-dense region [183–186] this is particularly relevant to explaining the tension between the locally measured value of H_0 and the (smaller) value inferred by fitting CMB data (see e.g. Refs. [74, 75]). Another approach is to reconstruct the local universe in N-Body simulations e.g. Ref. [187]

finds that our particular position biases the measured Hubble parameter towards higher values, thus accounting for some of the tension between the local and distant probes of the Hubble parameter. In Ref. [188] it is shown that the Hubble parameter can be measured more precisely if observations are restricted to only the zones around critical points of the velocity field, in contrast with the usual approach of increasing statistics by averaging indiscriminately over large datasets.

In this chapter we study the statistical properties of boosted frames in which the spherically averaged Hubble flow looks most uniform. We are specially interested whether such a boost particular to our position (as measured in Ref. [155]) is consistent with the ΛCDM expectation. We also look at the dipolar structure of the Hubble flow and its role in determining the frames of minimum Hubble variation. We re-derive the expression for the systematic offset of Hubble parameters between different reference frames paying attention to the dipolar structure. Our expression agrees with the measured offset between the CMB and LG frames and resolves much of the discrepancy found in previous studies [77, 155].

We use one of the biggest N-Body simulations of ΛCDM to date [44] having a volume of $(8\,h^{-1}\mathrm{Gpc})^3$ with the observers placed randomly in large-scale under- and over-densities. We find that the expectations derived from the simulation are *consistent* with the measurements for our particular position [77, 155]. Specifically, for an observer in an under-density, a boost simultaneously makes the spherically averaged Hubble parameter converge quicker to the background value and reduces the dipole structure. We also find that the boost velocity of the frame that minimises the Hubble variation for our location is consistent with the distribution extracted from the ΛCDM simulation and is indeed correlated with the group velocity of the 'finite infinity' region as has been suggested earlier [155].

In Sec.5.2 we describe the N-Body simulation and the halo finder used in this chapter. Sec.5.3 summarises the methods and the theoretical concepts used in this chapter. Our results are presented and discussed in Sec.5.4, and we conclude in Sec.5.5.

5.2 Simulations and data

We use the largest N-Body simulation of the Dark Sky (DS) Simulations Early Data Release [44] which we describe in detail in Sec. 1.1.5. The mean halo-halo distance in the catalogue we use is approximately $6\,h^{-1}$Mpc. This number density is about twice that of the COMPOSITE catalogue [163, 166] used in Ref. [77, 155] and comparable to the *Cosmicflows-2.1* [189] catalogue used in Ref. [155]. We use both of these in § 5.4. Although *Cosmicflows-2.1* is affected by Malmquist bias as discussed in Refs. [155, 190] we do not attempt to correct for this as we are interested in calculating quantities where this bias cancels.

5.3 Frames with minimal Hubble flow variation

In this section we study frames of observers where the spherically averaged Hubble flow converges the quickest to the background value. In an universe with structure there is a specific reference frame at each position where the expansion looks most uniform and we can determine its velocity $\mathbf{v}_{\rm min}$ relative to the cosmic rest frame. If the universe has no preferred direction, the unique frame where the variation of the Hubble flow is minimised for an ensemble of observers corresponds, by symmetry, to the cosmic rest frame (aka the CMB frame) i.e. $\langle \mathbf{v}_{\rm min} \rangle = \mathbf{0}$, where the brackets correspond to the ensemble average. Therefore, we expect a distribution of velocities $\mathbf{v}_{\rm min}$ for an ensemble of observers in a ΛCDM universe and consequently a non-zero expectation for the amplitude of $\mathbf{v}_{\rm min}$ for any particular observer. This directly parallels the consideration of bulk velocities, insofar as $\langle \mathbf{v}_{\rm bulk} \rangle = \mathbf{0}$ for any region of space but $\langle |\mathbf{v}_{\rm bulk}| \rangle \neq 0$. In fact as we will show later frames of minimum Hubble variation are in large part determined by the bulk flows.

To sum up, in the standard framework, the cosmic rest frame and the frame of minimum Hubble flow variation need *not* coincide for a particular observer. What we will now determine is whether the measured value of $\mathbf{v}_{\rm min}$ at our position [77, 155] is consistent with the ΛCDM expectation.

5.3.1 Fitting the linear Hubble law

Let us consider measuring the Hubble parameter in spherical shells about a particular point (here we follow the notation of [77]). The observer fits a linear Hubble law to data in each shell. We consider low redshifts where the linear Hubble law is a good approximation and there is no dependence on the parameters of the ΛCDM cosmological model (other than H_0).

The standard linear regression in each spherical shell s is performed by minimising $\chi^2_{\rm s} = \sum_i \left[\sigma_i^{-1}(r_i - cz_i/H)\right]^2$ with respect to H, where r_i is the distance to a particular object, σ_i is the error on the distance measurement, and z_i is the redshift of the object. This gives the Hubble parameter for that shell and the associated error:

$$H_{\rm s} = \left(\sum_{i=1}^{N_{\rm s}} \frac{(cz_i)^2}{\sigma_i^2}\right)\left(\sum_{i=1}^{N_{\rm s}} \frac{cz_i r_i}{\sigma_i^2}\right)^{-1}, \quad \sigma^2_{\rm s} = \left(\sum_{i=1}^{N_{\rm s}} \frac{(cz_i)^2}{\sigma_i^2}\right)^{3}\left(\sum_{i=1}^{N_{\rm s}} \frac{cz_i r_i}{\sigma_i^2}\right)^{-4}. \tag{5.1}$$

In a N-body simulation there are no distance uncertainties, so σ_i in the equation above can be set to unity for simplicity and without loss of generality. This yields the "pure" ΛCDM result. Survey specific predictions can be obtained by producing mock catalogues which include the distance (and other) uncertainties.

We study the contributions to the Hubble parameter and, later, the effects of changing reference frames, by expanding the relevant quantities up to the dipole term. The redshifts of objects as measured in some initial frame in a thin spherical shell at distance r are:

$$z_i = z(r)(1 + \mathbf{d}\cdot\hat{\mathbf{r}}_i + ...), \tag{5.2}$$

where $z(r)$ is the background redshift at the position of an object and $\hat{\mathbf{r}}_i$ is a unit vector in the direction of that object. The dipole part for the continuous distribution of objects can be estimated as

$$\mathbf{d} = 3\langle z(\theta,\phi)\hat{\mathbf{r}}(\theta,\phi)\rangle / \langle z(\theta,\phi)\rangle, \tag{5.3}$$

where θ and ϕ are spherical polar angles and $\langle\bullet\rangle$ corresponds to the spherical average. We use the fact that $\langle\hat{r}_x^2\rangle = \langle\hat{r}_y^2\rangle = \langle\hat{r}_z^2\rangle = 1/3$. The formula above can be rewritten then

for isotropically distributed discrete tracers as

$$\mathbf{d} \approx 3 \left(\sum_{i=1}^{N} z_i \hat{\mathbf{r}}_i \right) / \left(\sum_{i=1}^{N} z_i \right). \tag{5.4}$$

The redshifts can be written in terms of the peculiar velocities $\mathbf{v}_\mathrm{p}$ as (setting $c = 1$):

$$z_i = z(r) + \mathbf{v}_\mathrm{p} \cdot \hat{\mathbf{r}}_i. \tag{5.5}$$

All velocities considered in this chapter are non-relativistic. We neglect relativistic effects as they lead to errors of the order $\mathcal{O}(v/c)$ which is $\sim 0.1\%$ for typical peculiar velocities of several hundred km/s. These errors are much smaller than errors in distance measurements, for example, and are irrelevant in practice when working with real data.

By applying Eq.(5.4) to the above expression we find that the dipole term is approximately related to the bulk velocity of the spherical shell:

$$\mathbf{d}(r) \approx \mathbf{v}_\mathrm{bulk}(r)/z(r). \tag{5.6}$$

This expression is exact when all the objects have the same peculiar velocity.[1] The bulk velocity is defined here as the volume average of the peculiar velocities:

$$\mathbf{v}_\mathrm{bulk} = \frac{1}{V} \int_V \mathbf{v}_\mathrm{p} \, \mathrm{d}V \approx \frac{1}{N} \sum_{i=1}^{N} \mathbf{v}_{p,i}, \tag{5.7}$$

where the last approximation is used to estimate the bulk flow of N discrete tracers in volume V (e.g. halos in a N-Body simulation).[2]

The spherically averaged Hubble parameter obtained by a linear fit (5.1) is:

$$H_\mathrm{s} = \frac{\langle (z(r)(1 + \mathbf{d} \cdot \hat{\mathbf{r}}_i + ...))^2 \rangle}{\langle (z(r)(1 + \mathbf{d} \cdot \hat{\mathbf{r}}_i + ...)) r \rangle} = \frac{z(r)}{r} \left(1 + \frac{1}{3} |\mathbf{d}|^2 + ... \right) \approx \frac{z(r)}{r} \left(1 + \frac{1}{3} \frac{|\mathbf{v}_\mathrm{bulk}(r)|^2}{z(r)^2} \right), \tag{5.8}$$

where $\langle \bullet \rangle$ corresponds to the spherical average (e.g. the spherical average $\langle (\mathbf{d} \cdot \hat{\mathbf{r}}_i)^2 \rangle$ is $|\mathbf{d}|^2/3$). The linear terms in H_s above on average cancel for an isotropic distribution of objects and we are left only with the quadratic contributions. The cancellation of linear

[1] The simple estimator (5.4) receives contributions from higher moments, so is *not* reliable for estimation of bulk velocity. However, it is precisely this sum from Eq.(5.4) that is needed later on, e.g. in Eq.(5.10).

[2] This is the approach of Ref. [191] which also showed that the bulk flow estimate does not depend on the mass of the halos used, so we can simply employ the number averages.

terms works even when the sky coverage is incomplete provided the missing patches are symmetrically distributed on the opposite sides of the sky as is the case for e.g. the Zone of Avoidance.

Note that the Hubble parameter obtained by performing a linear fit of the Hubble diagram is biased towards higher values provided that the redshifts of objects have a non-zero dipole term or equivalently if the bulk flows are non-zero. The typical magnitude of the bulk flows is of order a few hundred km/s [162, 163, 165–167, 170, 173, 175, 176] hence below $\sim 70h^{-1}$Mpc where $H_0 r \approx 7000\,\mathrm{km/s}$, the bias can be up to a few percent but becomes negligible for larger distances. The precise value of this bias can be calculated in linear theory or, more accurately, estimated from N-Body simulations since the distances involved are already in a mildly non-linear regime.

5.3.2 Boosted frames and systematic offset of H_s

Now we boost an observer by $\mathbf{v}$ with respect to the initial frame. The redshifts change to:

$$z_i' = z_i - \mathbf{v}\cdot\hat{\mathbf{r}}_i = z(r)(1 + \mathbf{d}'\cdot\hat{\mathbf{r}}_i + ...), \tag{5.9}$$

where $\mathbf{d}' = \mathbf{d} - \mathbf{v}/z(r)$. Using Eq.(5.1) and following Eq.(5.8) we find the difference between the spherically averaged Hubble parameters in boosted and initial frames to be:

$$H_\mathrm{s}' - H_\mathrm{s} = \frac{z(r)}{r}\left(1 + \frac{1}{3}|\mathbf{d}'|^2 + ...\right) - \frac{z(r)}{r}\left(1 + \frac{1}{3}|\mathbf{d}|^2 + ...\right) = \frac{\frac{1}{3}|\mathbf{v}|^2 - \frac{1}{3}2\mathbf{v}\cdot\mathbf{d}(r)z(r) + ...}{\langle z(r)r\rangle}. \tag{5.10}$$

Furthermore, we can replace $z(r)$ with $H_0 r$. The error in this substitution is of order δH so it affects the equation above (already of order δH) at the next order which we neglect. We can also approximate $\mathbf{d}(r)$ with $\mathbf{v}_\mathrm{bulk}(r)/z(r)$ as in Eq.(5.6). This leads to

$$H_\mathrm{s}' - H_\mathrm{s} \approx \frac{\frac{1}{3}|\mathbf{v}|^2 - \frac{1}{3}2\mathbf{v}\cdot\mathbf{v}_\mathrm{bulk}(r)}{H_0\langle r^2\rangle}. \tag{5.11}$$

We stress that any initial frame, including the frame in which the Hubble flow is most uniform, can have and typically does have dipole structure in the velocity field, as we show later. Allowing for this dipole structure originating in bulk flows leads to

the second term in the numerator in Eq.(5.10) above. This term spoils the pure $1/\langle r^2\rangle$ dependence of the differences in Hubble parameters in spherical shells between boosted and initial frames. Our formula (5.10) for systematic offset of $H_{\rm s}$ between reference frames is thus *different* from corresponding equations in Refs. [77, 155] where the second dipole term was neglected under the assumption that the initial frame has no dipole structure.[3] Therefore, the refinements of Eq.(5.10) and the correct spherical averages of quantities need to be taken into account when studying the systematic offsets in $H_{\rm s}$ due to Lorentz boosts and assessing the size of the non-kinematical effects studied in Refs. [77, 155].

Boosts can either increase or decrease the Hubble parameter in each spherical shell. Whereas $H'_{\rm s}$ can be increased without bound with large enough boost $\mathbf{v}$, there is a limit to how much it can be decreased. Let us write the boost in terms of the components parallel and perpendicular to the bulk velocity of the objects in the spherical shell, $\mathbf{v} = \alpha \mathbf{v}_{\rm bulk}(r) + \mathbf{v}_{\perp bulk}(r)$. Minimising Eq.(5.11) results in

$$\mathrm{Min}\,(H'_{\rm s} - H_{\rm s}) \approx \mathrm{Min}\left(\frac{\frac{1}{3}(\alpha^2|\mathbf{v}_{\rm bulk}|^2 + |\mathbf{v}_{\perp \rm bulk}|^2) - \frac{1}{3}2\alpha|\mathbf{v}_{\rm bulk}|^2}{H_0\langle r^2\rangle}\right) = \frac{-\frac{1}{3}|\mathbf{v}_{\rm bulk}(r)|^2}{H_0\langle r^2\rangle}. \tag{5.12}$$

This corresponds to the boost to the frame where the dipole vanishes and the Hubble parameter $H_{\rm s}$ only receives contribution from the pure monopole $z(r)/r$ (see Eq.5.8). Note that the dipoles are in general *different* from shell to shell and a single boost cannot make the dipoles vanish in all the shells simultaneously.

It follows that there are two separate cases based on whether the monopole part of the flow before the boost is above or below the background value H_0. When it is below, a boost can bring $H_{\rm s}$ arbitrarily close to H_0. If it is above, $H_{\rm s}$ can only be brought down to its monopole value which is the lowest any boost can achieve.

5.3.3 Finding the frame of minimum Hubble variation

We now define following Ref. [77] the measure of closeness of Hubble flow to the expected background flow and the method of finding the frame of the most uniform Hubble flow.

The fractional deviation of the Hubble parameter in a spherical shell from the back-

[3] In addition, there is a small numerical error in the denominator of Eq.(9) of Ref. [77] where the factor 2 should be 3, and similarly in Refs. [155, 159].

ground value is $\delta H_{\rm s} = (H_{\rm s} - H_0)$. The case of uniform flow is $\delta H = 0$, which is also the expectation of linear perturbation theory. The frame with minimum Hubble flow variation for a particular observer is found by solving for a boost velocity $\mathbf{v} = \mathbf{v}_{\rm min}$ that minimises the sum of the mean square differences of δH, weighted by their errors:

$$\chi^2(\mathbf{v}) = \sum_{j=s}^{N_{\rm shells}} \frac{\delta H_j^2}{\sigma_{H_j}^2}. \tag{5.13}$$

The boost velocity $\mathbf{v}_{\rm min}$ will depend somewhat on the details of binning the distances into concentric shells. The expression above is simplified compared to Refs. [77, 155] — in a N-Body simulation the value of H_0 is known exactly and so its errors are not included above.

We briefly mention another method to estimate the Hubble parameter that is suitable for, and frequently used in, N-body simulations where there are no errors on distances r_i. It is using an estimator that is linear in redshift:

$$H_{s,\rm lin} = \frac{1}{N_{\rm s}} \sum_{i=1}^{N_{\rm s}} \frac{cz_i}{r_i}, \quad \sigma_{\rm s}^2 = \frac{1}{N_{\rm s}} \sum_{i=1}^{N_{\rm s}} \left(\frac{cz_i}{r_i}\right)^2 - H_{s,\rm lin}^2 \tag{5.14}$$

The value of $H_{s,\rm lin}$ is unaffected by boosts because the linear contribution will cancel on average in Eq.(5.14) above. Hence the velocities of frames of minimum Hubble variation have a trivial uniform distribution when using the estimator above. In this chapter we use the observationally relevant estimator in Eq.(5.1).

5.3.4 Linear perturbation theory

Linear perturbation theory provides some insight into the relevant factors that determine the frames of minimum Hubble variation within the framework of standard cosmology. For the discussion of cosmological perturbation theory see Chapter 1.

The peculiar velocity field can be written as:

$$\mathbf{v}_{\rm p}(\mathbf{r}, t) = \frac{H(t) f}{4\pi} \int \frac{\delta(\mathbf{r}')(\mathbf{r} - \mathbf{r}')}{|\mathbf{r} - \mathbf{r}'|^3} \, {\rm d}\mathbf{r}'^3, \tag{5.15}$$

where $H(t)$,$a(t)$,f,$\delta(\mathbf{r})$ are the background Hubble parameter, the scale factor, the growth factor, and the overdensity respectively. Note that the dominant contribution in Eq.(5.15) comes from large scales. Taking the divergence of the peculiar velocity field

gives:

$$\nabla \cdot \mathbf{v}_{\rm p}(\mathbf{r}, t) = -H(t) f \delta(\mathbf{r}). \tag{5.16}$$

The local Hubble parameter is proportional to the divergence of the velocity field:

$$H_{\rm loc}(\mathbf{r}, t) = H(t) + \frac{1}{3}\nabla \cdot \mathbf{v}_{\rm p}(\mathbf{r}, t) = H(t) - \frac{1}{3}H(t) f \delta(\mathbf{r}). \tag{5.17}$$

The bulk flow velocity $\mathbf{v}_{\rm bulk}$ is obtained by taking a volume average of the peculiar velocity field in Eq.(5.15). Note that for spherical volumes the density monopole does not affect the bulk velocity in linear theory, that is, the dominant contribution comes from the density dipole term. However, the value of the Hubble parameter is positively correlated with the density monopole (i.e. low/high values correspond to overdensities/underdensities), as has been noted in the context of N-Body simulations [73].

We see from Eq.(5.10) that the contribution of a boost (consequently $\mathbf{v}_{\rm min}$) to the linear fit estimate of the Hubble parameter (5.1) depends on the bulk flow, $\mathbf{v}_{\rm bulk}$, as well as on the density monopole (via Eq.5.17). This leads to a non-trivial dependence of $\mathbf{v}_{\rm min}$ on the density of the local environment as well as the bulk flow as measured in the CMB frame.

5.3.5 Finite Infinity

The notion of finite infinity (FI) was originally introduced in discussion of the 'fitting problem' where it was defined as a time-like surface within which the dynamics can be treated as isolated from the rest of the universe [156]. Here, we adopt a more specific definition in line with Refs. [157,158]. Finite infinity is associated with the smallest region within which the average expansion, $\langle\theta\rangle_{\rm V}$, vanishes, while being positive outside. That is, the boundaries of finite infinity separate collapsing regions from the expanding ones. We further simplify the definition by estimating the average expansion, or equivalently the divergence of the velocity field, in a spherical volume using discrete tracers (i.e. DM halos):

$$\langle\theta\rangle_{\rm V} = \langle\nabla \cdot \mathbf{v}\rangle_{\rm V} \approx \frac{3}{N}\sum_{i=1}^{N}\left(\frac{\mathbf{v}_i \cdot \hat{\mathbf{r}}_i}{r_i}\right), \tag{5.18}$$

where $\mathbf{v} = H_0\mathbf{r} + \mathbf{v}_{\rm p}$. The region of finite infinity has an associated bulk(group) velocity, $\mathbf{v}_{\rm fi}$, with respect to the CMB frame. Virialised structure and discreteness of the tracers

provide the lower cut-off to the size and meaningfulness of the FI region.

5.3.6 A simple picture

Let us illustrate the relations among various velocities discussed so far with a simple set-up. Imagine a spherical volume of space that has a small collapsing central part while the outer part is expanding with the background (i.e. uniform Hubble flow). On top of this flow let us add peculiar velocities that are the same for each tracer, $\mathbf{v}_{\rm p}$. The bulk flow for any spherical subvolume or shell is $\mathbf{v}_{\rm bulk} = \mathbf{v}_{\rm p}$. In the CMB frame this bulk flow will bias the linear fit estimate of the Hubble parameter in spherical shells (see Eqs.(5.1) and (5.8)). Boosting into a frame with $\mathbf{v}_{\rm min} = \mathbf{v}_{\rm p}$ will remove the bulk flow and restore the background Hubble parameter in the outer regions. At the same time the bulk velocity of the collapsing finite infinity region,$\mathbf{v}_{\rm fi}$, is the same as the bulk flow of the whole spherical region and the velocity of the frame of most uniform Hubble flow ($\mathbf{v}_{\rm min} = \mathbf{v}_{\rm bulk} = \mathbf{v}_{\rm fi}$). In this simple situation we have a trivial peculiar velocity profile (i.e. constant and perfectly correlated). Since the actual velocity field is correlated, this simplistic set-up is still relevant hence we expect that the directions and magnitudes of $\mathbf{v}_{\rm min}, \mathbf{v}_{\rm bulk}, \mathbf{v}_{\rm fi}$ are also correlated.

5.4 Results and Discussion

When working with simulation data we use radial bins of width $10h^{-1}$Mpc with the lower limit $10h^{-1}$Mpc and the upper limit $100h^{-1}$Mpc. Changing the bin size (to $20h^{-1}$Mpc) and lower and upper limits (to $20h^{-1}$Mpc and $120h^{-1}$Mpc respectively) do not affect the results by more than 10%. We use the simulation output at $z = 0$ as we are only interested in distances below $100h^{-1}$Mpc (corresponding to $z \approx 0.025$) where the Hubble law is linear.

We select observers randomly in the simulation volume. This simple procedure does not place observers in halos where they may be expected to be in the actual universe [192]. However our volume weighted approach enables direct comparison to perturbation theory and analytical calculations (e.g. Refs. [72, 75]). We define overdense and underdense regions up to $100h^{-1}$Mpc as those that are consistently over or under the average density.

5.4.1 Systematic offset in Hubble parameter in different reference frames

The larger monopole variation of the Hubble law in the CMB frame compared to the LG frame as was noted in Refs. [77, 155] is due to the non-linear dependence of $H_{\rm s}$ on the redshift (see Eq.5.1). Boost to a different frame results in a systematic offset in the Hubble parameter $H_{\rm s}$. We have improved the earlier calculation [77, 155] by recognising that the frame of minimum Hubble flow variation typically has a dipolar structure. This yields the expression (5.10) which shows that the systematic offsets in $H_{\rm s}$ do *not* have the pure $1/r^2$ dependence as was assumed earlier, but additionally have a dependence on the dipole structure of the velocity field.

Using a N-Body simulation we extracted the difference between the Hubble parameters in the minimum Hubble variation frame and the CMB frame, $\delta H_{\rm s} = H_{\rm s,fin} - H_{\rm s,CMB}$, by looking for the appropriate boost $\mathbf{v}_{\rm min}$ using Eq.(5.13). This difference $\delta H_{\rm s}$ was compared to the estimate (5.10) where the dipoles in each spherical shell were obtained using Eq.(5.4). We plot the actual against the estimated $\delta H_{\rm s}$ in Fig.5.1 which shows that the points are well correlated with the best-fit slope very close to unity. Additionally, the scatter of the points provides an estimate of the error in Eq.(5.10) due to neglecting the terms higher than dipole.

We now test the boost formula (5.10) on real data in order to understand the discrepancy between the measured value of $H_{\rm CMB} - H_{\rm LG}$ and the $1/r^2$ expectation from Refs. [77, 155]. We use both the *Cosmicflows-2.1* catalogue [189] and the COMPOSITE catalogue [163, 166] to obtain the Hubble parameters in spherical shells in the CMB and LG frames. We plot these in Fig.5.2. The dipoles needed for our estimation of $H_{\rm CMB} - H_{\rm LG}$ in Eq.(5.10) are obtained via Eq.(5.4). The errors in the estimation are a combination of the distance errors in the catalogues and the error in the formula itself extracted from the tests on our N-Body simulation. Note that *Cosmicflows-2.1* has a Malmquist bias which largely cancels in $H_{\rm CMB} - H_{LG}$, however, some small differences in the measured values between the two catalogues can be attributed to this bias [155].

In Fig.5.3 we plot $H_{\rm CMB} - H_{LG}$ in radial bins chosen as in Refs. [77,155]. Note that the differences in Hubble parameters in the CMB and LG frames are completely consistent

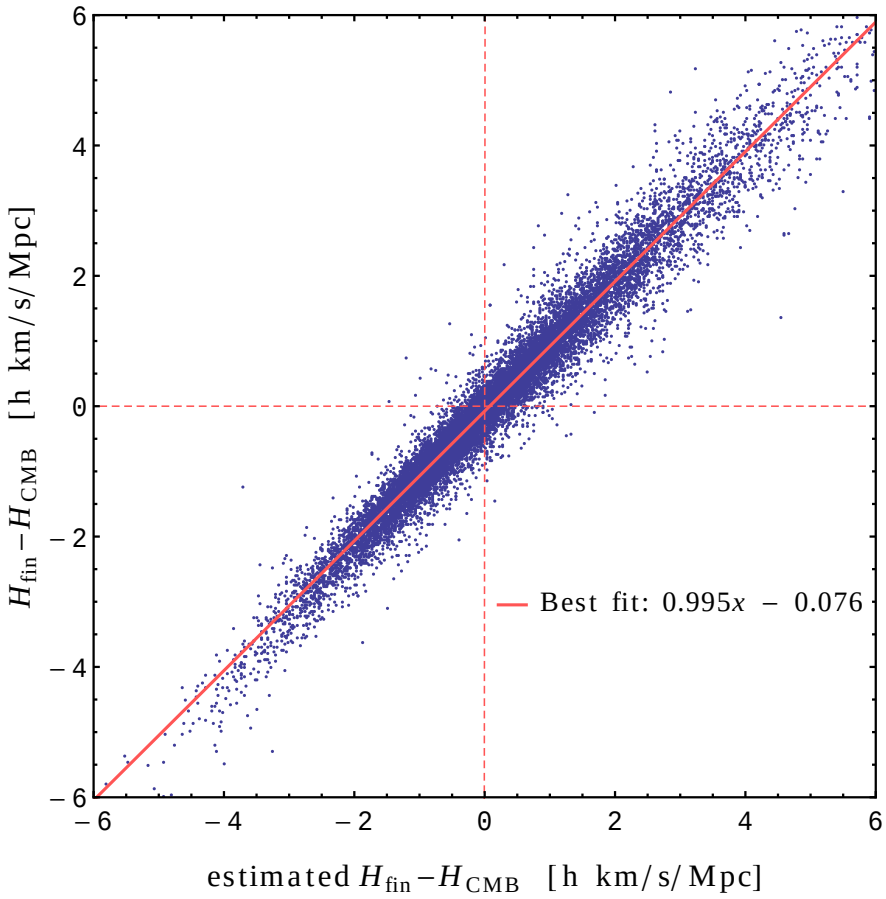

Figure 5.1: Actual versus estimated $H_{\rm fin} - H_{\rm CMB}$ for the radial bin at 40-50h^{-1}Mpc.

with the boost formula (5.10). The previously highlighted discrepancy was mainly due to the assumption that the frames close to the minimum Hubble flow variation frame have negligible dipole structure of the velocity field. However, as discussed in § 5.3.2, the initial dipoles in spherical shells are typically different (albeit correlated), and a boost to the frame of minimum Hubble flow variation therefore never reduces all the dipoles to zero. In fact, if the initial Hubble parameters in spherical shells are below the background value, then the boost to the minimum Hubble flow variation frame will *increase* the dipoles. Therefore, the dipole structure must necessarily be considered when deriving the expectation for the systematic offsets in $H_{\rm s}$ due to change of reference frame.

5.4.2 Variation of H

In this section we study the effect of boosting into frames with minimal Hubble variation. The expectation is that such boosts bring the radial Hubble flow profile closer to the background expectation of $H_0 \equiv 100h$ km/s/Mpc. Indeed we see in Fig.5.4 that the spread of measured Hubble parameter is much smaller in every radial bin and closer to

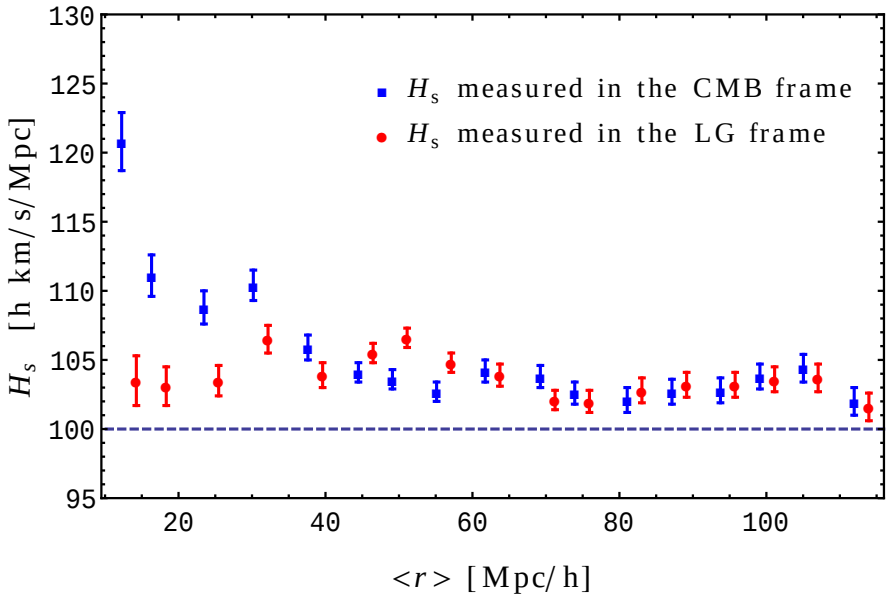

Figure 5.2: Hubble parameters $H_{\rm CMB}$ and $H_{\rm LG}$ for the COMPOSITE catalogue. The values for the LG frame have the radial coordinate shifted by $2h^{-1}$Mpc for clarity. The average radial coordinate of a bin, $\langle r \rangle$, is the error weighted average of positions of objects in that bin.

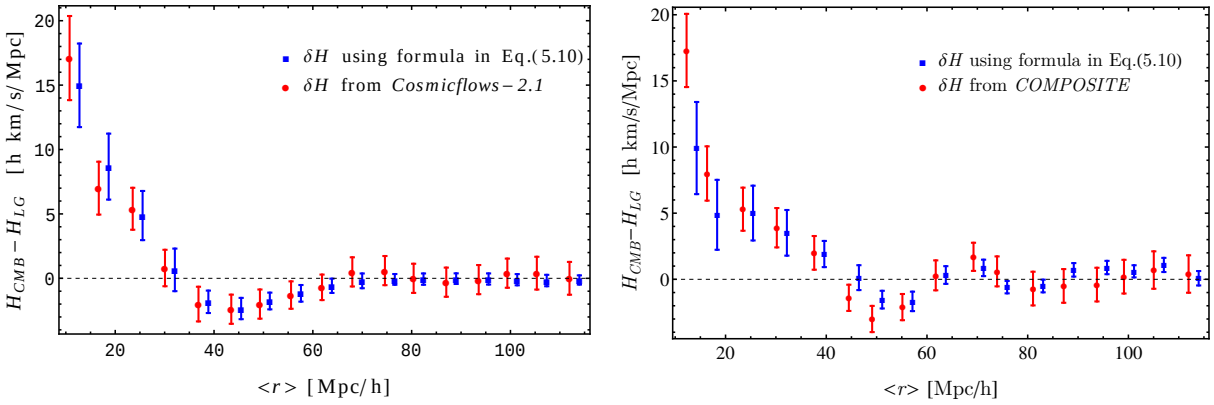

Figure 5.3: Actual vs estimated $H_{\rm CMB} - H_{\rm LG}$ for the *Cosmicflows-2.1* and COMPOSITE catalogues. The predicted values have the radial coordinate shifted by $2h^{-1}$Mpc for clarity. The average radial coordinate of a bin, $\langle r \rangle$, is the error weighted average of positions of objects in that bin.

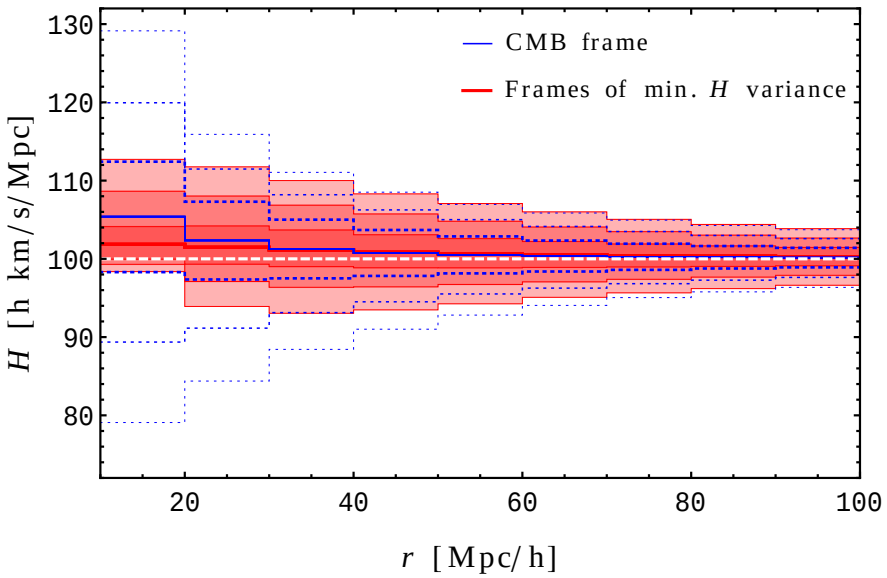

Figure 5.4: Hubble parameter as measured by randomly placed observers in the CMB frame (blue lines) and as measured in frames of most uniform Hubble flow (shaded red). The contours are 68.3%, 95.4% and 99.7% confidence intervals while solid lines are the mean values. Note the bias towards higher values of H compared to H_0.

H_0, once every observer is boosted by their respective $\mathbf{v}_{\rm min}$. However, above $\sim 60h^{-1}$Mpc there is not much difference. The effect of changing frames is suppressed by $1/\langle r^2\rangle$ (see Eq.5.10), so larger distances are less important in determining $\mathbf{v}_{\rm min}$ and less affected by the boosts. Therefore, most of the influence on the $\mathbf{v}_{\rm min}$ velocity distribution comes from the regions in the mildly non-linear to non-linear regime, which justifies the use of a N-Body simulation in our work.

At late times most of the volume of the universe is in voids. If an observer is placed in a random location, it is more likely to be located in an underdensity than an overdensity. This leads to the bias of the Hubble parameter towards higher values compared to H_0 as can be seen in Fig.5.4 where the solid line represents the average value of H for the ensemble of observers. This has also been noted in Ref. [73]. Additionally, at scales below about $50h^{-1}$Mpc there is an additional bias towards higher $H_{\rm s}$ due to the dipole component of the velocity field as discussed in § 5.3 and shown in Eq.(5.8).

Boosting to frames of most uniform Hubble flow will bring the Hubble parameter closer to H_0, however, the monopole part cannot be reduced (see Eqs.5.8,5.10,5.12) and therefore some residual bias towards higher values of H is left also in those frames (again see Fig.5.4).

For the cases where the value of H is smaller than the background, which are on

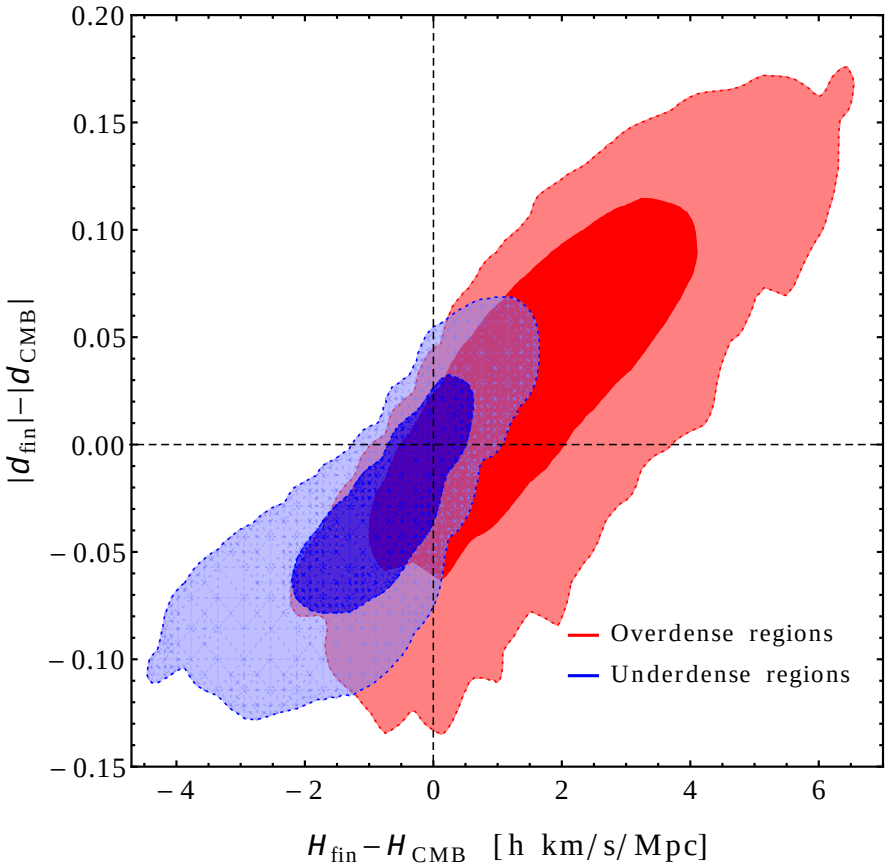

Figure 5.5: Difference between the dipole in the Hubble flow in the frame of minimum Hubble variation and in the CMB frame, plotted against the difference of the spherically averaged Hubble parameter. Observers in both overdense and underdense locations are chosen in the $40-50\,h^{-1}$Mpc radial bin. The contours correspond to 68.3% and 95.4% confidence intervals.

average associated with the overdense regions, boosts to the frame of minimum Hubble variation increase the dipole term in order to bring $H_{\rm s}$ closer to H_0. Differently, in the underdense regions, boosts to the frame of minimum Hubble variation decrease the dipole term in order to bring $H_{\rm s}$ closer to H_0. This preference can be seen in Fig.5.5 where we plot the difference between the dipoles against the difference in the Hubble parameters before and after boosting by $\mathbf{v}_{\rm min}$ for the over- and underdense positions.

5.4.3 The probability distribution of $\mathbf{v}_{\rm min}$

Now we study the distribution of velocities $\mathbf{v}_{\rm min}$ of frames where the spherically averaged Hubble flow looks most uniform. We separate observers based on their local environment: random in volume, in underdensities, and in overdensities. We find $\mathbf{v}_{\rm min}$ by an algorithm that scans randomly for the velocity vector that minimises the variation (see Eq.5.13) with resolution of about 150 km/s. The algorithm is then nested to

achieve an average precision of 10 km/s. Fig.5.6 shows the distribution of the individual components of $\mathbf{v}_{\rm min}$— the distributions are identical for each Cartesian component and centred on $\mathbf{v}_{\rm min}= \mathbf{0}$ as required by the symmetries of the simulation. We perform a Gaussian fit to find the associated variance of $\mathbf{v}_{\rm min}$and plot its norm in Fig.5.7. This should be Maxwell-Boltzmann distributed if the underlying distribution for the components is truly Gaussian but we note there are small departures consistent with the variances of the Gaussian fits. We also mark the norm and the error of the boost that makes the Hubble flow around our position most uniform (1203^{+529}_{-625} km/s) as obtained in Ref. [155]). We note that this value is not inconsistent with the ΛCDM expectation for a randomly located observer. An earlier estimate [77] suggested that $\mathbf{v}_{\rm min}$ for our location approximately corresponds to the velocity of the Local Group (635 ± 38 km/s as inferred from the CMB dipole).

The amplitude of $\mathbf{v}_{\rm min}$ depends on the local environment in terms of average density as can be seen from Fig.5.7. The denser the region around an observer's location the larger the amplitude of the boost. There are two reasons for this. Firstly, the Hubble parameter has bigger variance in the overdense locations relative to the underdense locations, stemming from the bigger variance in the density field there.[4] The bigger variance in H will result in a bigger amplitude of boosts required. Secondly, in the overdense locations the monopole of the Hubble flow is on average smaller than H_0[5]. The values of H smaller than H_0 can be brought arbitrarily close to H_0 by introducing an extra dipole which results in bigger boosts compared to the underdense case. For underdense locations the Hubble parameter H is expected to be above H_0. There is a limit, derived in Eq.(5.12), on how much the Hubble parameter can be lowered by a boost — it can only be brought to its 'pure' monopole value (which is on average closer to but still above H_0). Therefore the amplitude of $\mathbf{v}_{\rm min}$ for underdense locations is expected to be smaller compared to overdense locations.

[4]The underdense regions are bounded by $-1 \leq \delta$ where δ is the fractional density. There is no such bound for overdense locations.

[5]This can be heuristically understood in terms of extra gravitational attraction of matter in the overdense regions above the background expectation, thus effectively lowering the recessional velocities due to the expansion of background space.

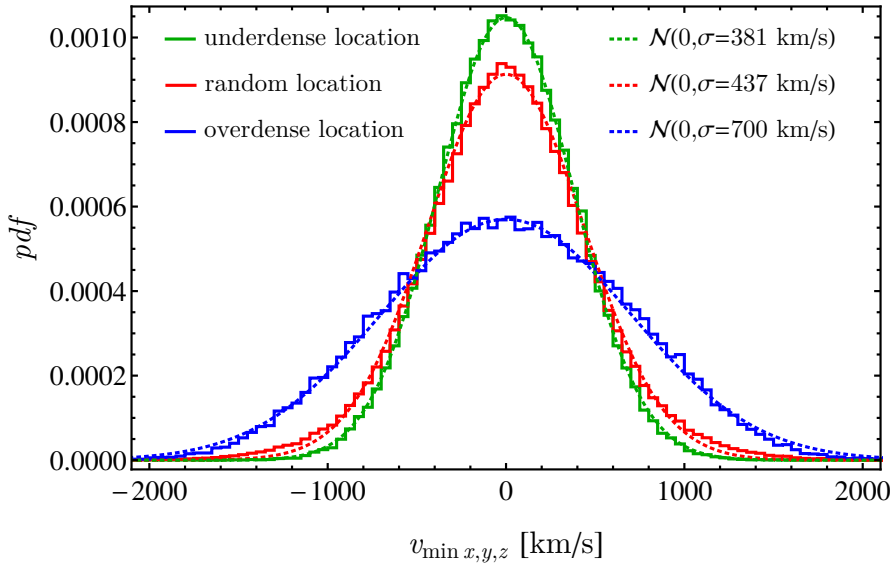

Figure 5.6: Probability distribution function for the components of the velocity $\mathbf{V}_{\mathrm{min}}$ for frames in which the Hubble flow looks most uniform. Observer locations are chosen based on the average density within 100 h^{-1}Mpc. The dashed lines are Gaussian fits.

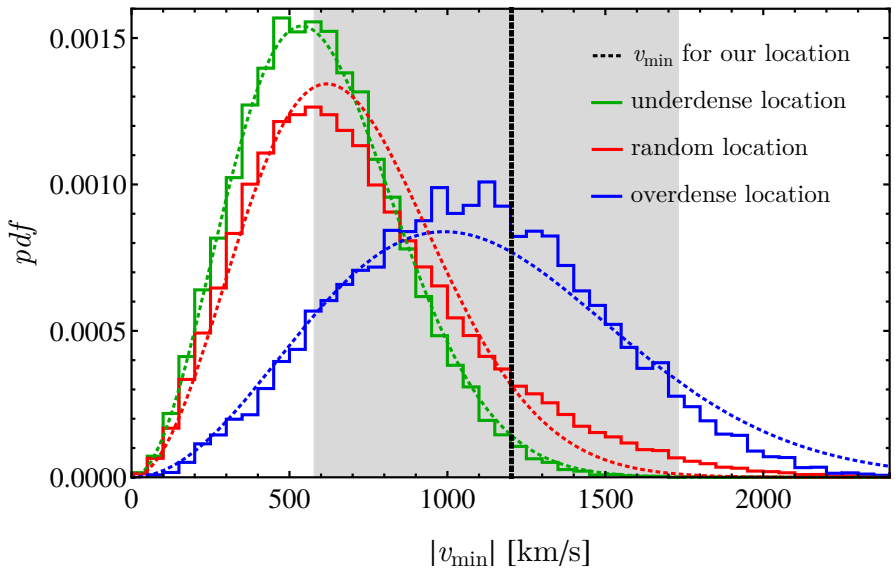

Figure 5.7: Probability distribution function for the norms of the velocity of frames of minimum Hubble variation. Observer locations are chosen as in the previous figure.

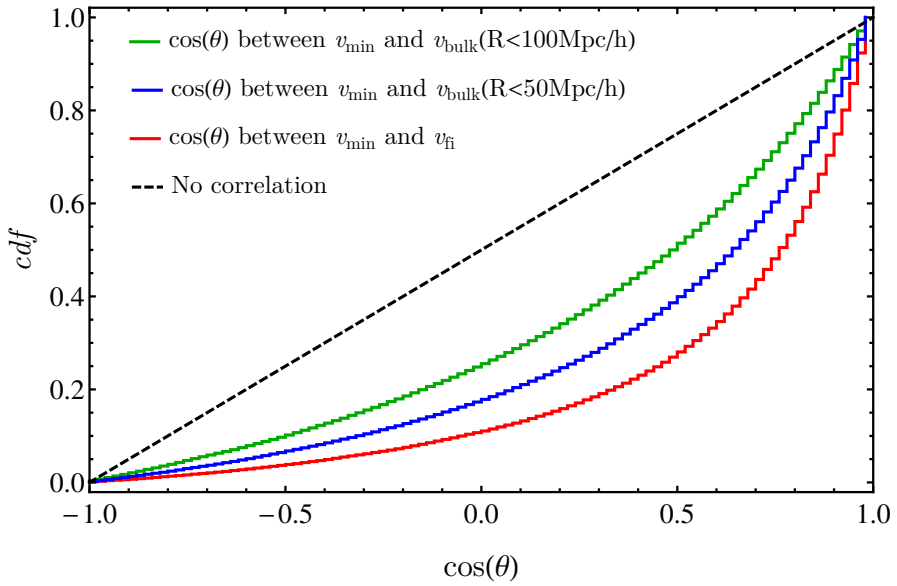

Figure 5.8: Cumulative distribution function for the cosine of the angle between $v_{\rm min}$ and various bulk velocities.

5.4.4 Correlations between $\mathbf{v_{bulk}}$, $\mathbf{v_{min}}$, and $\mathbf{v_{fi}}$

In Fig.5.8 we plot the cumulative distribution function (CDF) for the cosine of the angle between the boost $\mathbf{v}_{\rm min}$ and the bulk velocity of the finite infinity region $\mathbf{v}_{\rm fi}$, as well as the bulk velocities within $50h^{-1}$Mpc and $100h^{-1}$Mpc radii. The observers are located at random in the simulation volume[6]. In all cases the direction of $\mathbf{v}_{\rm min}$ is positively correlated with the bulk velocities. This is unsurprising as the average observer is located in an underdensity where boosts to the frames of minimum Hubble flow variation mainly reduce the existing dipole originating from the bulk velocity. The correlation is weaker for larger radii as the influence on $\mathbf{v}_{\rm min}$ is roughly suppressed by $1/\langle r^2\rangle$ (see Eq.5.10) and is thus strongest for the region of 'finite infinity' which is the smallest region considered (of typical size $15h^{-1}$Mpc in our N-body simulation). This supports the expectation that the boost to the frame of minimum Hubble variation should roughly correspond to the frame of the bulk motion of the 'finite infinity' region [155].

We examine this claim more closely by reversing the logic and calculating the Hubble parameter in the frames of 'finite infinity' for each observer (see Fig.5.9). The Hubble parameter is indeed closer to its background value and has smaller variance compared

[6]Note that at late times most of the matter has collapsed into highly non-linear structures and most of the volume consists of underdense regions. Placing an observer randomly in volume will preferentially sample the underdense regions. Conversely, placing observers in halos will preferentially sample the overdense regions where most halos are located.

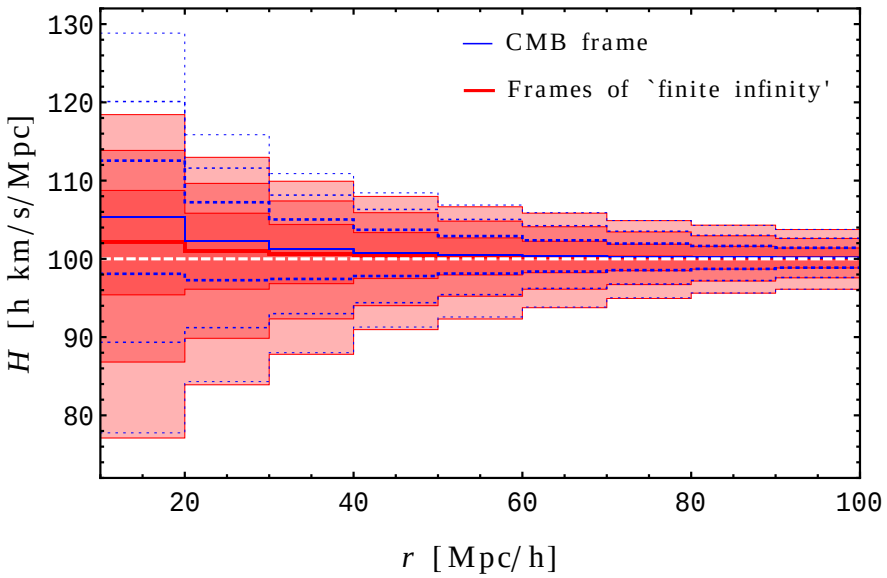

Figure 5.9: Hubble parameter as measured in the CMB frame (blue lines) and in frames of 'finite infinity' (shaded red). The contours are 68.3%, 95.4% and 99.7% confidence intervals while the solid lines are the means. Observers are located randomly. Note the small reduction in the Hubble variance (which is however still much bigger than in Fig.5.4).

to the CMB frame. Again, this is unsurprising as the bulk velocity of the 'finite infinity' region is correlated with the bulk velocity of a bigger region. Hence, boosting into the FI frame on average reduces the dipole in the velocity flow and lowers the estimate for H. For random observers that are more likely to be in underdense regions with $H > H_0$, this has the effect of making H closer to the background value. However, comparing the frame of minimum Hubble flow variation (Fig.5.4) to the 'finite infinity' frame (Fig.5.9), we note that the Hubble flow is much less uniform in the latter showing that further boosts are still required.

5.5 Summary

In this chapter we have studied the properties of boost velocities of observers with respect to the CMB frame that make the spherically averaged Hubble flow converge the quickest to its background value. We used a Hubble volume sized N-body simulation to place observers at locations with different local environment. We find that the distribution of boost velocities is near Gaussian with the amplitudes depending on the observer's location — the larger the overdensity the larger the amplitude of a typical boost required. For observers in underdense regions, on average, the boosts that make the spherically

averaged Hubble parameter converge faster to the background value reduce at the same time the dipole structure of the Hubble flow. Based only on such local measurements of the velocity field the observers would choose such a frame as the cosmic rest frame given that it is closest to the naïve FLRW expectation. However for the overdense locations, the boosts that make the Hubble parameter closer to the background value on average increase the dipole of the velocity field. We show that the boost velocity to the frame of most uniform flow is correlated with the bulk flow velocities and in particular with the group velocity of the 'finite infinity' region, as was suggested in [155]. The amplitude of the boost for our position [155] in the universe is found *not* to be in tension with the ΛCDM expectations.

Additionally we re-derived the expression for the systematic offset of the Hubble parameter between different frames, noting that the dipole structure in spherical shells cannot be boosted away entirely. Our expression agrees with the measured difference between $H_{\rm CMB}$ and $H_{\rm LG}$ and resolves discrepancies in previous work.

Chapter 6: Conclusion and future directions

Detailed summaries of the work in this thesis have been presented at the end of each chapter. Here we discuss how our results can be extended and motivate further research. The work in this thesis has been concerned with some of the issues and shortcomings of the ΛCDM model that stem from inhomogeneities in the universe.

We start by examining whether the generation of inhomogeneities within the inflationary paradigm can be understood generically without resorting to any particular model of inflation among the large number of 'toy' models considered so far. In Chapter 2 we showed that generic potentials of field theories for a single scalar field can be decomposed in a way that isolates the parts that dominate at lower energies. We used the solutions of the exact renormalisation group equations (ERGE) within the mean-field approximation (MFA). This amounts to neglecting the kinetic terms and roughly corresponds to the similar approximation in slow-roll scalar field models of inflation. We argued therefore that potentials that successfully drive inflation are just the ones singled out by the ERGE. That is, given some arbitrary UV theory containing a scalar field decoupled from other fields, the potential dominating the theory at lower energies (where inflation begins) will be the one preferred by the ERGE. Our work relied on several assumptions that can be relaxed in order to improve our analysis. Firstly, the condition where the kinetic term is exactly zero can be abandoned. Allowing the scalar field to have a small non-zero time derivative would bring our treatment of ERGE closer to the slow-roll approximation. In some of our potentials we identified regions where slow-roll conditions are violated. If MFA is abandoned and combined with the exact integration of the inflationary dynamics (away from slow-roll approximation), we can check whether the transient violations of the slow-roll regime lead to observable features in the primordial power spectrum. In our work we do not specify the size of self-coupling of the scalar field and neglect couplings to other fields. Our ERGE analysis can be strengthened by including such couplings. Finally, the most challenging task would be to include gravitational effects in the ERGE and performing the analysis in non-Minkowski space-time.

In Chapter 3 we introduced a new method to characterise the inhomogeneity in the distribution of matter. The method complements the established 'counts-in-cells' approaches and is based on anomalous diffusion modelled as random walks on the underlying set of DM halos. We use it to identify the onset of homogeneity in a cosmological N-Body simulation. The method proposed here improves on the 'counts-in-cells' approaches as it can distinguish whether the underlying distribution of halos is truly fractal or merely a homogeneous distribution of lower dimension (e.g. a uniform sheet or a filament). The natural extension is to perform a similar analysis on real datasets. Real surveys have non-trivial geometries and the method will have to be adapted to allow diffusion on such datasets as a consequence. At this stage, however, the surveys are too small and sparse for this to be viable.

The inhomogeneities can also be analysed in terms of the velocity field. In Chapter 4, motivated by the existence of the Bullet Cluster, we studied extremely rare mergers of galaxy clusters. We investigated whether the ΛCDM prediction for the number of such collisions is consistent with the number observed. There is currently mild tension that will increase if more such systems are discovered. Our analysis can be strengthened by directly employing the lightcone data in N-Body simulations instead of a single redshift slice. However, we do use an approximation to convert the $z = 0$ slice measurements to lightcone expectations. Additionally, the mechanism that increases the frequency of extreme cluster mergers can be investigated. It has been explored already that different models of dark energy result in different number of mergers [144]. Another mechanism can be via a change in the primordial spectrum, for example, adding non-negligible non-Gaussianity.

Finally, we focus on the role of the inhomogeneous velocity field in determining the background rate of expansion of space. In Chapter 5 we investigated whether the fact that the Hubble parameter converges faster to its asymptotic value in the Local Group frame and not in the CMB frame as might be naïvely expected in ΛCDM model is in fact consistent with the standard model. We show that the frames of minimum Hubble variation are determined by the local bulk flow and the monopole of the velocity field. We find that the measured value for the boost that makes the Hubble flow most uniform is consistent with ΛCDM. This work touches upon two important puzzles of the standard

model, namely the unexpectedly high bulk flows and the significantly higher Hubble parameter as measured locally compared to the global measurement. These puzzles motivate the study of all the things that could bias those measurements in order to reliably establish potential inconsistency with the ΛCDM model.

Bibliography

[1] A. Einstein, *Feldgleichungen der Gravitation*, *Sitzungsber. d. PreuR. Akad. d. Wiss.* (1915) 844–847.

[2] A. Friedmann, *Über die Krümmung des Raumes*, *Zeitschrift fur Physik* **10** (1922) 377–386.

[3] G. Lemaître, *Expansion of the universe, A homogeneous universe of constant mass and increasing radius accounting for the radial velocity of extra-galactic nebulae*, *MNRAS* **91** (Mar., 1931) 483–490.

[4] H. P. Robertson, *On the Foundations of Relativistic Cosmology*, *Proceedings of the National Academy of Science* **15** (Nov., 1929) 822–829.

[5] A. G. Walker, *On milne's theory of world-structure*, *Proceedings of the London Mathematical Society* **s2-42** (1937), no. 1 90–127, [`http://plms.oxfordjournals.org/content/s2-42/1/90.full.pdf+html`].

[6] E. Hubble, *A relation between distance and radial velocity among extra-galactic nebulae*, *Proceedings of the National Academy of Sciences* **15** (1929), no. 3 168–173, [`http://www.pnas.org/content/15/3/168.full.pdf`].

[7] F. Zwicky, *On the Masses of Nebulae and of Clusters of Nebulae*, *ApJ* **86** (Oct., 1937) 217.

[8] F. D. Kahn and L. Woltjer, *Intergalactic Matter and the Galaxy.*, *ApJ* **130** (Nov., 1959) 705.

[9] H. W. Babcock, *The rotation of the Andromeda Nebula*, *Lick Observatory Bulletin* **19** (1939) 41–51.

[10] V. C. Rubin and W. K. Ford, Jr., *Rotation of the Andromeda Nebula from a Spectroscopic Survey of Emission Regions*, *ApJ* **159** (Feb., 1970) 379.

[11] A. A. Penzias and R. W. Wilson, *A Measurement of Excess Antenna Temperature at 4080 Mc/s.*, *ApJ* **142** (July, 1965) 419–421.

[12] G. F. Smoot, C. L. Bennett, A. Kogut, E. L. Wright, J. Aymon, N. W. Boggess, E. S. Cheng, G. de Amici, S. Gulkis, M. G. Hauser, G. Hinshaw, P. D. Jackson, M. Janssen, E. Kaita, T. Kelsall, P. Keegstra, C. Lineweaver, K. Loewenstein, P. Lubin, J. Mather, S. S. Meyer, S. H. Moseley, T. Murdock, L. Rokke, R. F. Silverberg, L. Tenorio, R. Weiss, and D. T. Wilkinson, *Structure in the COBE differential microwave radiometer first-year maps*, *ApJL* **396** (Sept., 1992) L1–L5.

[13] S. Perlmutter, G. Aldering, G. Goldhaber, R. A. Knop, P. Nugent, P. G. Castro, S. Deustua, S. Fabbro, A. Goobar, D. E. Groom, I. M. Hook, A. G. Kim, M. Y. Kim, J. C. Lee, N. J. Nunes, R. Pain, C. R. Pennypacker, R. Quimby, C. Lidman, R. S. Ellis, M. Irwin, R. G. McMahon, P. Ruiz-Lapuente, N. Walton, B. Schaefer, B. J. Boyle, A. V. Filippenko, T. Matheson, A. S. Fruchter, N. Panagia, H. J. M. Newberg, W. J. Couch, and T. S. C. Project, *Measurements of* Ω *and* Λ *from 42 High-Redshift Supernovae*, *ApJ* **517** (June, 1999) 565–586, [`astro-ph/9812133`].

[14] A. G. Riess, A. V. Filippenko, P. Challis, A. Clocchiatti, A. Diercks, P. M. Garnavich, R. L. Gilliland, C. J. Hogan, S. Jha, R. P. Kirshner, B. Leibundgut, M. M. Phillips, D. Reiss, B. P. Schmidt, R. A. Schommer, R. C. Smith, J. Spyromilio, C. Stubbs, N. B. Suntzeff, and J. Tonry, *Observational evidence*

from supernovae for an accelerating universe and a cosmological constant, *The Astronomical Journal* **116** (1998), no. 3 1009.

[15] R. M. Wald, *General relativity*. 1984.

[16] M. P. Hobson, G. P. Efstathiou, and A. N. Lasenby, *General Relativity*. Dec., 2005.

[17] E. A. Milne, *Relativity, gravitation and world-structure*. 1935.

[18] E. Lifshitz, *On the Gravitational stability of the expanding universe*, *J. Phys.(USSR)* **10** (1946) 116.

[19] J. M. Bardeen, *Gauge-invariant cosmological perturbations*, *Phys. Rev. D* **22** (Oct., 1980) 1882–1905.

[20] H. Kodama and M. Sasaki, *Cosmological Perturbation Theory*, *Progress of Theoretical Physics Supplement* **78** (1984) 1.

[21] S. Dodelson, *Modern cosmology*. 2003.

[22] V. F. Mukhanov, H. A. Feldman, and R. H. Brandenberger, *Theory of cosmological perturbations*, *physrep* **215** (June, 1992) 203–333.

[23] R. Durrer, *Gauge Invariant Cosmological Perturbation Theory: A General Study and It's Application to the Texture Scenario of Structure Formation*, *Fund. Cosmic Phys.* **15** (1994) 209–339, [astro-ph/9311041].

[24] Planck Collaboration, P. A. R. Ade, N. Aghanim, M. Arnaud, F. Arroja, M. Ashdown, J. Aumont, C. Baccigalupi, M. Ballardini, A. J. Banday, and et al., *Planck 2015 results. XVII. Constraints on primordial non-Gaussianity*, *ArXiv e-prints* (Feb., 2015) [arXiv:1502.0159].

[25] A. A. Starobinsky, *A new type of isotropic cosmological models without singularity*, *Physics Letters B* **91** (Mar., 1980) 99–102.

[26] D. Kazanas, *Dynamics of the universe and spontaneous symmetry breaking*, *ApJL* **241** (Oct., 1980) L59–L63.

[27] A. H. Guth, *Inflationary universe: A possible solution to the horizon and flatness problems*, *Phys. Rev. D* **23** (Jan, 1981) 347–356.

[28] A. D. Linde, *A New Inflationary Universe Scenario: A Possible Solution of the Horizon, Flatness, Homogeneity, Isotropy and Primordial Monopole Problems*, *Phys. Lett.* **B108** (1982) 389–393.

[29] Planck Collaboration, P. A. R. Ade, N. Aghanim, M. Arnaud, M. Ashdown, J. Aumont, C. Baccigalupi, A. J. Banday, R. B. Barreiro, J. G. Bartlett, and et al., *Planck 2015 results. XIII. Cosmological parameters*, *ArXiv e-prints* (Feb., 2015) [arXiv:1502.0158].

[30] K. Enqvist and J. Sirkka, *Chemical equilibrium in QCD gas in the early universe*, *Physics Letters B* **314** (Sept., 1993) 298–302, [hep-ph/9304273].

[31] V. F. Mukhanov and G. V. Chibisov, *Quantum fluctuations and a nonsingular universe*, *Soviet Journal of Experimental and Theoretical Physics Letters* **33** (May, 1981) 532.

[32] L. Senatore and M. Zaldarriaga, *The constancy of ζ in single-clock Inflation at all loops*, *Journal of High Energy Physics* **9** (Sept., 2013) 148, [arXiv:1210.6048].

[33] D. H. Lyth and A. R. Liddle, *The Primordial Density Perturbation*. June, 2009.

[34] J. D. Barrow, *The inflationary universe - Modern developments*, *QJRAS* **29** (June, 1988) 101–117.

[35] E. R. Harrison, *Fluctuations at the threshold of classical cosmology*, *Phys. Rev. D* **1** (May, 1970) 2726–2730.

[36] Y. B. Zeldovich, *A hypothesis, unifying the structure and the entropy of the Universe*, *MNRAS* **160** (1972) 1P.

[37] A. R. Liddle and S. M. Leach, *How long before the end of inflation were observable perturbations produced?*, *Phys. Rev. D* **68** (Nov., 2003) 103503, [astro-ph/0305263].

[38] J. Noller, F. von Braun-Bates, and P. G. Ferreira, *Relativistic scalar fields and the quasistatic approximation in theories of modified gravity*, *Phys. Rev. D* **89** (Jan., 2014) 023521, [arXiv:1310.3266].

[39] G. Rigopoulos and W. Valkenburg, *On the accuracy of N-body simulations at very large scales*, *MNRAS* **446** (Jan., 2015) 677–682, [arXiv:1308.0057].

[40] J.-c. Hwang and H. Noh, *Why Newtonian gravity is reliable in large-scale cosmological simulations*, *MNRAS* **367** (Apr., 2006) 1515–1520, [astro-ph/0507159].

[41] S. J. Aarseth, *Dynamical evolution of clusters of galaxies, I*, *MNRAS* **126** (1963) 223.

[42] W. Dehnen, *Towards optimal softening in three-dimensional N-body codes - I. Minimizing the force error*, *MNRAS* **324** (June, 2001) 273–291, [astro-ph/0011568].

[43] A. Knebe, S. R. Knollmann, S. I. Muldrew, F. R. Pearce, M. A. Aragon-Calvo, Y. Ascasibar, P. S. Behroozi, D. Ceverino, S. Colombi, J. Diemand, K. Dolag, B. L. Falck, P. Fasel, J. Gardner, S. Gottlöber, C.-H. Hsu, F. Iannuzzi, A. Klypin, Z. Lukić, M. Maciejewski, C. McBride, M. C. Neyrinck, S. Planelles, D. Potter, V. Quilis, Y. Rasera, J. I. Read, P. M. Ricker, F. Roy, V. Springel, J. Stadel, G. Stinson, P. M. Sutter, V. Turchaninov, D. Tweed, G. Yepes, and M. Zemp, *Haloes gone MAD: The Halo-Finder Comparison Project*, *Mon. Not. R. Astron. Soc.* **415** (Aug., 2011) 2293–2318, [arXiv:1104.0949].

[44] S. W. Skillman, M. S. Warren, M. J. Turk, R. H. Wechsler, D. E. Holz, and P. M. Sutter, *Dark Sky Simulations: Early Data Release*, *ArXiv e-prints* (July, 2014) [arXiv:1407.2600].

[45] P. S. Behroozi, R. H. Wechsler, and H.-Y. Wu, *The ROCKSTAR Phase-space Temporal Halo Finder and the Velocity Offsets of Cluster Cores*, *Astrophys. J.* **762** (Jan., 2013) 109, [arXiv:1110.4372].

[46] D. N. Spergel, L. Verde, H. V. Peiris, E. Komatsu, M. R. Nolta, C. L. Bennett, M. Halpern, G. Hinshaw, N. Jarosik, A. Kogut, M. Limon, S. S. Meyer, L. Page, G. S. Tucker, J. L. Weiland, E. Wollack, and E. L. Wright, *First-Year Wilkinson Microwave Anisotropy Probe (WMAP) Observations: Determination of Cosmological Parameters*, *ApJS* **148** (Sept., 2003) 175–194, [astro-ph/0302209].

[47] J. Trøst Nielsen, A. Guffanti, and S. Sarkar, *Marginal evidence for cosmic acceleration from Type Ia supernovae*, *ArXiv e-prints* (June, 2015) [arXiv:1506.0135].

[48] J. Martin, *Everything you always wanted to know about the cosmological constant problem (but were afraid to ask)*, *Comptes Rendus Physique* **13** (July, 2012) 566–665, [arXiv:1205.3365].

[49] S. Sarkar, *Is the evidence for dark energy secure?*, *General Relativity and Gravitation* **40** (Feb., 2008) 269–284, [arXiv:0710.5307].

[50] S. Weinberg, *The cosmological constant problem*, *Rev. Mod. Phys.* **61** (Jan, 1989) 1–23.

[51] T. Buchert, *On Average Properties of Inhomogeneous Fluids in General Relativity: Dust Cosmologies*, *General Relativity and Gravitation* **32** (Jan., 2000) 105–126, [gr-qc/9906015].

[52] T. Buchert, *On Average Properties of Inhomogeneous Fluids in General Relativity: Perfect Fluid Cosmologies*, *General Relativity and Gravitation* **33** (Aug., 2001) 1381–1405, [gr-qc/0102049].

[53] E. W. Kolb, S. Matarrese, and A. Riotto, *On cosmic acceleration without dark energy*, *New Journal of Physics* **8** (Dec., 2006) 322, [astro-ph/0506534].

[54] D. L. Wiltshire, *Cosmic clocks, cosmic variance and cosmic averages*, *New Journal of Physics* **9** (Oct., 2007) 377, [gr-qc/0702082].

[55] C. Clarkson, G. Ellis, J. Larena, and O. Umeh, *Does the growth of structure affect our dynamical models of the universe? The averaging, backreaction and fitting problems in cosmology*, *Rept. Prog. Phys.* **74** (2011) 112901, [arXiv:1109.2314].

[56] T. Buchert, M. Carfora, G. F. R. Ellis, E. W. Kolb, M. A. H. MacCallum, J. J. Ostrowski, S. Räsänen, B. F. Roukema, L. Andersson, A. A. Coley, and D. L. Wiltshire, *Is there proof that backreaction of inhomogeneities is irrelevant in cosmology?*, *Classical and Quantum Gravity* **32** (Nov., 2015) 215021, [arXiv:1505.0780].

[57] J. J. Ostrowski and B. F. Roukema, *On the Green and Wald formalism*, in *14th Marcel Grossmann Meeting on Recent Developments in Theoretical and Experimental General Relativity, Astrophysics, and Relativistic Field Theories (MG14) Rome, Italy, July 12-18, 2015*, 2015. arXiv:1512.0294.

[58] S. R. Green and R. M. Wald, *How well is our Universe described by an FLRW model?*, *Classical and Quantum Gravity* **31** (Dec., 2014) 234003, [arXiv:1407.8084].

[59] S. R. Green and R. M. Wald, *Comments on Backreaction*, *ArXiv e-prints* (June, 2015) [arXiv:1506.0645].

[60] J. T. Giblin, J. B. Mertens, and G. D. Starkman, *Departures from the Friedmann-Lemaitre-Robertston-Walker Cosmological Model in an Inhomogeneous Universe: A Numerical Examination*, *Physical Review Letters* **116** (June, 2016) 251301, [arXiv:1511.0110].

[61] E. Bentivegna and M. Bruni, *Effects of Nonlinear Inhomogeneity on the Cosmic Expansion with Numerical Relativity*, *Physical Review Letters* **116** (June, 2016) 251302, [arXiv:1511.0512].

[62] G. F. R. Ellis and G. W. Gibbons, *Discrete Newtonian Cosmology*, *Class. Quant. Grav.* **31** (2014) 025003, [arXiv:1308.1852].

[63] T. Clifton, *What's the Matter in Cosmology?*, 2015. arXiv:1509.0668.

[64] J.-P. Bruneton and J. Larena, *Dynamics of a lattice Universe: the dust approximation in cosmology*, *Classical and Quantum Gravity* **29** (Aug., 2012) 155001, [arXiv:1204.3433].

[65] P. Fleury, H. Dupuy, and J.-P. Uzan, *Interpretation of the Hubble diagram in a nonhomogeneous universe*, *Phys. Rev. D* **87** (June, 2013) 123526, [arXiv:1302.5308].

[66] P. Fleury, H. Dupuy, and J.-P. Uzan, *Can All Cosmological Observations Be Accurately Interpreted with a Unique Geometry?*, *Physical Review Letters* **111** (Aug., 2013) 091302, [arXiv:1304.7791].

[67] I. Odderskov, S. M. Koksbang, and S. Hannestad, *The local value of H_0 in an inhomogeneous universe*, *JCAP* **2** (Feb., 2016) 001, [arXiv:1601.0735].

[68] E. Shellard, *The future of cosmology: observational and computational prospects in The Future of Theoretical Physics and Cosmology: Celebrating Stephen Hawking's Contributions to Physics*. Cambridge University Press, 2003.

[69] D. H. D. H. Lyth and A. A. Riotto, *Particle physics models of inflation and the cosmological density perturbation*, *physrep* **314** (June, 1999) 1–146, [hep-ph/9807278].

[70] J. Martin, C. Ringeval, and V. Vennin, *Encyclopædia Inflationaris*, *Physics of the Dark Universe* **5** (Dec., 2014) 75–235, [arXiv:1303.3787].

[71] L.-Y. Chiang, *The importance of Fourier phases for the morphology of gravitational clustering*, *MNRAS* **325** (July, 2001) 405–411, [astro-ph/0011021].

[72] Y. Wang, D. N. Spergel, and E. L. Turner, *Implications of Cosmic Microwave Background Anisotropies for Large-Scale Variations in Hubble's Constant*, *ApJ* **498** (May, 1998) 1–10, [astro-ph/9708014].

[73] R. Wojtak, A. Knebe, W. A. Watson, I. T. Iliev, S. Heß, D. Rapetti, G. Yepes, and S. Gottlöber, *Cosmic variance of the local Hubble flow in large-scale cosmological simulations*, *MNRAS* **438** (Feb., 2014) 1805–1812, [arXiv:1312.0276].

[74] I. Ben-Dayan, R. Durrer, G. Marozzi, and D. J. Schwarz, *Value of H_0 in the Inhomogeneous Universe*, *Physical Review Letters* **112** (June, 2014) 221301, [arXiv:1401.7973].

[75] V. Marra, L. Amendola, I. Sawicki, and W. Valkenburg, *Cosmic Variance and the Measurement of the Local Hubble Parameter*, *Physical Review Letters* **110** (June, 2013) 241305, [arXiv:1303.3121].

[76] A. R. King and G. F. R. Ellis, *Tilted homogeneous cosmological models*, *Communications in Mathematical Physics* **31** (1973), no. 3 209–242.

[77] D. L. Wiltshire, P. R. Smale, T. Mattsson, and R. Watkins, *Hubble flow variance and the cosmic rest frame*, *Phys. Rev. D* **88** (Oct., 2013) 083529, [arXiv:1201.5371].

[78] K. Wilson and J. B. Kogut, *The Renormalization group and the epsilon expansion*, *Phys.Rept.* **12** (1974) 75–200.

[79] J. Polonyi, *Lectures on the functional renormalization group method*, *Central Eur.J.Phys.* **1** (2003) 1–71, [hep-th/0110026].

[80] C. Bervillier, *The Wilson exact renormalization group equation and the anomalous dimension parameter*, *Condens. Matter Phys.* **16** (2013) 23003, [arXiv:1304.4131].

[81] C. Bagnuls and C. Bervillier, *Exact renormalization group equations. An Introductory review*, *Phys.Rept.* **348** (2001) 91, [hep-th/0002034].

[82] J. Serreau, *Renormalization group flow and symmetry restoration in de sitter space*, *Physics Letters B* **730** (2014) 271–274.

[83] D. Benedetti, *Critical behavior in spherical and hyperbolic spaces*, *Journal of Statistical Mechanics: Theory and Experiment* **2015** (2015), no. 1 P01002.

[84] M. Guilleux and J. Serreau, *Quantum scalar fields in de Sitter space from the nonperturbative renormalization group*, *Phys. Rev. D* **92** (Oct., 2015) 084010, [arXiv:1506.0618].

[85] S. Grozdanov, D. Kraljić, and E. E. Svanes, *Inflationary potentials from the exact renormalisation group*, *Nuclear Physics B* **909** (Aug., 2016) 657–676, [arXiv:1508.0148].

[86] T. Vachaspati and M. Trodden, *Causality and cosmic inflation*, *Phys. Rev. D* **61** (Jan., 2000) 023502, [gr-qc/9811037].

[87] A. A. Starobinsky, *Stochastic de sitter (inflationary) stage in the early universe*, in *Field theory, quantum gravity and strings*, pp. 107–126. Springer, 1986.

[88] A. A. Starobinsky and J. Yokoyama, *Equilibrium state of a selfinteracting scalar field in the De Sitter background*, *Phys.Rev.* **D50** (1994) 6357–6368, [astro-ph/9407016].

[89] J. Polonyi, *Renormalization group in quantum mechanics*, *Annals Phys.* **252** (1996) 300–328, [hep-th/9409004].

[90] D. F. Litim and L. Vergara, *Subleading critical exponents from the renormalization group*, *Phys. Lett.* **B581** (2004) 263–269, [hep-th/0310101].

[91] D. Zappala, *Enhancement of field renormalization in scalar theories via functional renormalization group*, *Phys. Rev.* **D86** (2012) 125003, [arXiv:1206.2480].

[92] C. S. Fischer and H. Gies, *Renormalization flow of Yang-Mills propagators*, *JHEP* **10** (2004) 048, [hep-ph/0408089].

[93] J. Borchardt and B. Knorr, *Global solutions of functional fixed point equations via pseudospectral methods*, *Phys. Rev.* **D91** (2015), no. 10 105011, [arXiv:1502.0751]. [Erratum: Phys. Rev.D93,no.8,089904(2016)].

[94] J. Borchardt and B. Knorr, *Solving functional flow equations with pseudospectral methods*, *Phys. Rev. D* **94** (July, 2016) 025027, [arXiv:1603.0672].

[95] A. Salvio and A. Strumia, *Agravity*, *JHEP* **06** (2014) 080, [arXiv:1403.4226].

[96] K. Kannike, G. Hütsi, L. Pizza, A. Racioppi, M. Raidal, A. Salvio, and A. Strumia, *Dynamically Induced Planck Scale and Inflation*, *JHEP* **05** (2015) 065, [arXiv:1502.0133].

[97] E. J. Copeland, C. Rahmede, and I. D. Saltas, *Asymptotically Safe Starobinsky Inflation*, *Phys. Rev.* **D91** (2015), no. 10 103530, [arXiv:1311.0881].

[98] A. Kaya, *Exact renormalization group flow in an expanding Universe and screening of the cosmological constant*, *Phys. Rev.* **D87** (2013) 123501, [arXiv:1303.5459].

[99] I. D. Saltas, *Higgs inflation and quantum gravity: An exact renormalisation group approach*, *JCAP* **1602** (2016), no. 02 048, [arXiv:1512.0613].

[100] J. Polchinski, *Renormalization and effective lagrangians*, *Nuclear Physics B* **231** (1984), no. 2 269–295.

[101] J. Comellas and A. Travesset, *O (n) models within the local potential approximation*, *Nuclear Physics B* **498** (1997), no. 3 539–564.

[102] K. Halpern and K. Huang, *Nontrivial directions for scalar fields*, *Phys. Rev.* **D53** (1996) 3252–3259, [hep-th/9510240].

[103] V. Periwal, *Halpern-Huang directions in effective scalar field theory*, *Mod. Phys. Lett.* **A11** (1996) 2915–2920, [hep-th/9512108].

[104] C. Cheung, A. L. Fitzpatrick, J. Kaplan, L. Senatore, and P. Creminelli, *The effective field theory of inflation*, *Journal of High Energy Physics* **3** (Mar., 2008) 14–014, [arXiv:0709.0293].

[105] D. S. Goldwirth and T. Piran, *Initial conditions for inflation*, *Phys.Rept.* **214** (May, 1992) 223–292.

[106] Planck Collaboration, P. A. R. Ade, N. Aghanim, M. Arnaud, F. Arroja, M. Ashdown, J. Aumont, C. Baccigalupi, M. Ballardini, A. J. Banday, and et al., *Planck 2015 results. XX. Constraints on inflation*, *ArXiv e-prints* (Feb., 2015) [arXiv:1502.0211].

[107] D. H. Lyth, *What would we learn by detecting a gravitational wave signal in the cosmic microwave background anisotropy?*, *Phys. Rev. Lett.* **78** (Mar, 1997) 1861–1863.

[108] C. Clarkson, *Establishing homogeneity of the universe in the shadow of dark energy*, *Comptes Rendus Physique* **13** (July, 2012) 682–718, [arXiv:1204.5505].

[109] J. Pan and P. Coles, *Large scale cosmic homogeneity from a multifractal analysis of the pscz catalogue*, *Mon.Not.Roy.Astron.Soc.* **318** (2000) L51, [astro-ph/0008240].

[110] D. W. Hogg, D. J. Eisenstein, M. R. Blanton, N. A. Bahcall, J. Brinkmann, et al., *Cosmic homogeneity demonstrated with luminous red galaxies*, *Astrophys.J.* **624** (2005) 54–58, [astro-ph/0411197].

[111] P. Sarkar, J. Yadav, B. Pandey, and S. Bharadwaj, *The scale of homogeneity of the galaxy distribution in SDSS DR6*, *MNRAS* **399** (Oct., 2009) L128–L131, [arXiv:0906.3431].

[112] M. Scrimgeour, T. Davis, C. Blake, J. B. James, G. Poole, et al., *The WiggleZ Dark Energy Survey: the transition to large-scale cosmic homogeneity*, *Mon.Not.Roy.Astron.Soc.* **425** (2012) 116–134, [arXiv:1205.6812].

[113] C. A. Chacón-Cardona and R. A. Casas-Miranda, *Multifractal analysis and lacunarity spectrum of the galaxies of the ninth Sloan Digital Sky Survey (SDSS) data release*, *preprint (arXiv:1212.4832)* (Dec., 2012) [arXiv:1212.4832].

[114] J. Gaite, *Fractal analysis of the dark matter and gas distributions in the Mare-Nostrum universe*, *JCAP* **3** (Mar., 2010) 6, [arXiv:0806.0730].

[115] C. A. Chacón-Cardona and R. A. Casas-Miranda, *Millennium simulation dark matter haloes: multifractal and lacunarity analysis and the transition to homogeneity*, *MNRAS* **427** (Dec., 2012) 2613–2624, [arXiv:1209.2637].

[116] F. Sylos Labini, N. L. Vasilyev, L. Pietronero, and Y. V. Baryshev, *Absence of self-averaging and of homogeneity in the large-scale galaxy distribution*, *EPL (Europhysics Letters)* **86** (May, 2009) 49001, [arXiv:0805.1132].

[117] J. K. Yadav, J. Bagla, and N. Khandai, *Fractal Dimension as a measure of the scale of Homogeneity*, *Mon.Not.Roy.Astron.Soc.* **405** (2010) 2009, [arXiv:1001.0617].

[118] B. Pandey, *A method for testing the cosmic homogeneity with Shannon entropy*, *MNRAS* **430** (Apr., 2013) 3376–3382, [arXiv:1301.4961].

[119] R. van de Weygaert and et al., *Alpha, Betti and the Megaparsec Universe: on the Topology of the Cosmic Web*, *Lecture Notes in Computer Science. Vol. 6970, Transactions on Computational Science XIV* (June, 2013) 60–110, [arXiv:1306.3640].

[120] R. Speare, J. R. Gott, J. Kim, and C. Park, *Horizon Run 3: Topology as a Standard Ruler*, *ApJ* **799** (Feb., 2015) 176, [arXiv:1310.4278].

[121] C. Park and Y.-R. Kim, *Large-scale Structure of the Universe as a Cosmic Standard Ruler*, *ApJL* **715** (June, 2010) L185–L188, [arXiv:0905.2268].

[122] V. Springel and et al., *Simulations of the formation, evolution and clustering of galaxies and quasars*, *Nature* **435** (June, 2005) 629–636, [astro-ph/0504097].

[123] M. Kuhlen, M. Vogelsberger, and R. Angulo, *Numerical simulations of the dark universe: State of the art and the next decade*, *Physics of the Dark Universe* **1** (Nov., 2012) 50–93, [arXiv:1209.5745].

[124] J. W. Haus and K. W. Kehr, *Diffusion in regular and disordered lattices*, *physrep* **150** (June, 1987) 263–406.

[125] D. Ben-Avraham and S. Havlin, *Diffusion and reactions in fractals and disordered systems*. Cambridge University Press, 2000.

[126] I. Sokolov, *"anomalous diffusion on fractal networks"*, in *Mathematics of Complexity and Dynamical Systems* (R. A. Meyers, ed.), pp. 13–25. Springer New York, 2011.

[127] J. Bagla, J. Yadav, and T. Seshadri, *Fractal Dimensions of a Weakly Clustered Distribution and the Scale of Homogeneity*, *Mon.Not.Roy.Astron.Soc.* **390** (2007) 829, [arXiv:0712.2905].

[128] V. J. Martinez and E. Saar, *Statistics of the galaxy distribution*. CRC Press, 2010.

[129] V. J. Martinez, B. J. T. Jones, R. Dominguez-Tenreiro, and R. van de Weygaert, *Clustering paradigms and multifractal measures*, *ApJ* **357** (July, 1990) 50–61.

[130] B. J. T. Jones, V. J. Martinez, E. Saar, and J. Einasto, *Multifractal description of the large-scale structure of the universe*, *ApJL* **332** (Sept., 1988) L1–L5.

[131] P. J. E. Peebles, *The large-scale structure of the universe*. 1980.

[132] D. Clowe, A. Gonzalez, and M. Markevitch, *Weak-Lensing Mass Reconstruction of the Interacting Cluster 1E 0657-558: Direct Evidence for the Existence of Dark Matter*, *Astrophys. J.* **604** (Apr., 2004) 596–603, [astro-ph/0312273].

[133] M. Bradač, D. Clowe, A. H. Gonzalez, P. Marshall, W. Forman, C. Jones, M. Markevitch, S. Randall, T. Schrabback, and D. Zaritsky, *Strong and Weak Lensing United. III. Measuring the Mass Distribution of the Merging Galaxy Cluster 1ES 0657-558*, *Astrophys. J.* **652** (Dec., 2006) 937–947, [astro-ph/0608408].

[134] M. Markevitch, A. H. Gonzalez, D. Clowe, A. Vikhlinin, W. Forman, C. Jones, S. Murray, and W. Tucker, *Direct Constraints on the Dark Matter Self-Interaction Cross Section from the Merging Galaxy Cluster 1E 0657-56*, *Astrophys. J.* **606** (May, 2004) 819–824, [astro-ph/0309303].

[135] G. R. Farrar and R. A. Rosen, *A New Force in the Dark Sector?*, *Phys. Rev. Lett.* **98** (Apr., 2007) 171302, [astro-ph/0610298].

[136] C. Lage and G. Farrar, *Constrained Simulation of the Bullet Cluster*, *Astrophys. J.* **787** (June, 2014) 144, [arXiv:1312.0959].

[137] C. Lage and G. R. Farrar, *The bullet cluster is not a cosmological anomaly*, *JCAP* **2** (Feb., 2015) 038, [arXiv:1406.6703].

[138] C. Mastropietro and A. Burkert, *Simulating the Bullet Cluster*, *Mon. Not. R. Astron. Soc.* **389** (Sept., 2008) 967–988, [arXiv:0711.0967].

[139] V. Springel and G. R. Farrar, *The speed of the 'bullet' in the merging galaxy cluster 1E0657-56*, *Mon. Not. R. Astron. Soc.* **380** (Sept., 2007) 911–925, [astro-ph/0703232].

[140] M. Milosavljević, J. Koda, D. Nagai, E. Nakar, and P. R. Shapiro, *The Cluster-Merger Shock in 1E 0657-56: Faster than a Speeding Bullet?*, *Astron. J. Lett.* **661** (June, 2007) L131–L134, [astro-ph/0703199].

[141] R. Thompson and K. Nagamine, *Pairwise velocities of dark matter haloes: a test for the Λ cold dark matter model using the bullet cluster*, *Mon. Not. R. Astron. Soc.* **419** (Feb., 2012) 3560–3570, [arXiv:1107.4645].

[142] E. Hayashi and S. D. M. White, *How rare is the bullet cluster?*, *Mon. Not. R. Astron. Soc.* **370** (July, 2006) L38–L41, [astro-ph/0604443].

[143] J. Lee and E. Komatsu, *Bullet Cluster: A Challenge to ΛCDM Cosmology*, *Astrophys. J.* **718** (July, 2010) 60–65, [arXiv:1003.0939].

[144] V. R. Bouillot, J.-M. Alimi, P.-S. Corasaniti, and Y. Rasera, *Probing dark energy models with extreme pairwise velocities of galaxy clusters from the DEUS-FUR simulations*, *MNRAS* **450** (June, 2015) 145–159, [arXiv:1405.6679].

[145] R. Thompson, R. Davé, and K. Nagamine, *The rise and fall of a challenger: the Bullet Cluster in Λ cold dark matter simulations*, *MNRAS* **452** (Sept., 2015) 3030–3037, [arXiv:1410.7438].

[146] W. A. Watson, I. T. Iliev, J. M. Diego, S. Gottlöber, A. Knebe, E. Martínez-González, and G. Yepes, *Statistics of extreme objects in the Juropa Hubble Volume simulation*, *Mon. Not. R. Astron. Soc.* **437** (Feb., 2014) 3776–3786, [arXiv:1305.1976].

[147] J. E. Forero-Romero, S. Gottlöber, and G. Yepes, *Bullet Clusters in the MARENOSTRUM Universe*, *Astrophys. J.* **725** (Dec., 2010) 598–604, [arXiv:1007.3902].

[148] J. Lee and M. Baldi, *Can Coupled Dark Energy Speed up the Bullet Cluster?*, *Astrophys. J.* **747** (Mar., 2012) 45, [arXiv:1110.0015].

[149] J. F. Navarro, C. S. Frenk, and S. D. M. White, *The Structure of Cold Dark Matter Halos*, *Astrophys. J.* **462** (May, 1996) 563, [astro-ph/9508025].

[150] L. Hernquist, *N-body realizations of compound galaxies*, *Astrophys. J. Suppl.* **86** (June, 1993) 389–400.

[151] S. Coles, *An Introduction to Statistical Modeling of Extreme Values*. Lecture Notes in Control and Information Sciences. Springer, 2001.

[152] Y. Rasera, J.-M. Alimi, J. Courtin, F. Roy, P.-S. Corasaniti, A. Füzfa, and V. Boucher, *Introducing the dark energy universe simulation series (DEUSS)*, vol. 1241, pp. 1134–1139, June, 2010. arXiv:1002.4950.

[153] J. L. Tinker, B. E. Robertson, A. V. Kravtsov, A. Klypin, M. S. Warren, G. Yepes, and S. Gottlöber, *The Large-scale Bias of Dark Matter Halos: Numerical Calibration and Model Tests*, *Astrophys. J.* **724** (Dec., 2010) 878–886, [arXiv:1001.3162].

[154] J. L. Tinker, D. H. Weinberg, Z. Zheng, and I. Zehavi, *On the Mass-to-Light Ratio of Large-Scale Structure*, *Astrophys. J.* **631** (Sept., 2005) 41–58, [astro-ph/0411777].

[155] J. H. McKay and D. L. Wiltshire, *Defining the frame of minimum non-linear Hubble expansion variation*, *MNRAS* **457** (Apr., 2016) 3285–3305, [arXiv:1503.0419].

[156] G. F. R. Ellis, *Relativistic cosmology - Its nature, aims and problems*, in *General Relativity and Gravitation Conference* (B. Bertotti, F. de Felice, and A. Pascolini, eds.), pp. 215–288, 1984.

[157] D. L. Wiltshire, *Cosmic clocks, cosmic variance and cosmic averages*, *New Journal of Physics* **9** (Oct., 2007) 377, [gr-qc/0702082].

[158] D. L. Wiltshire, *Cosmological equivalence principle and the weak-field limit*, *Phys. Rev. D* **78** (Oct., 2008) 084032, [arXiv:0809.1183].

[159] K. Bolejko, M. A. Nazer, and D. L. Wiltshire, *Differential cosmic expansion and the Hubble flow anisotropy*, *JCAP* **6** (June, 2016) 035, [arXiv:1512.0736].

[160] T. R. Lauer and M. Postman, *The motion of the Local Group with respect to the 15,000 kilometer per second Abell cluster inertial frame*, *ApJ* **425** (Apr., 1994) 418–438.

[161] M. J. Hudson, R. J. Smith, J. R. Lucey, and E. Branchini, *Streaming motions of galaxy clusters within 12 000 km s^{-1}- V. The peculiar velocity field*, *MNRAS* **352** (July, 2004) 61–75, [astro-ph/0404386].

[162] A. Kashlinsky, F. Atrio-Barandela, D. Kocevski, and H. Ebeling, *A Measurement of Large-Scale Peculiar Velocities of Clusters of Galaxies: Results and Cosmological Implications*, *ApJL* **686** (Oct., 2008) L49–L52, [arXiv:0809.3734].

[163] R. Watkins, H. A. Feldman, and M. J. Hudson, *Consistently large cosmic flows on scales of 100h^{-1}Mpc: a challenge for the standard ΛCDM cosmology*, *MNRAS* **392** (Jan., 2009) 743–756, [arXiv:0809.4041].

[164] G. Lavaux, R. B. Tully, R. Mohayaee, and S. Colombi, *Cosmic Flow From Two Micron All-Sky Redshift Survey: the Origin of Cosmic Microwave Background Dipole and Implications for ΛCDM Cosmology*, *ApJ* **709** (Jan., 2010) 483–498, [arXiv:0810.3658].

[165] A. Kashlinsky, F. Atrio-Barandela, H. Ebeling, A. Edge, and D. Kocevski, *A New Measurement of the Bulk Flow of X-Ray Luminous Clusters of Galaxies*, *ApJL* **712** (Mar., 2010) L81–L85, [arXiv:0910.4958].

[166] H. A. Feldman, R. Watkins, and M. J. Hudson, *Cosmic flows on 100 h^{-1} Mpc scales: standardized minimum variance bulk flow, shear and octupole moments*, *MNRAS* **407** (Oct., 2010) 2328–2338, [arXiv:0911.5516].

[167] J. Colin, R. Mohayaee, S. Sarkar, and A. Shafieloo, *Probing the anisotropic local Universe and beyond with SNe Ia data*, *MNRAS* **414** (June, 2011) 264–271, [arXiv:1011.6292].

[168] C. Magoulas, C. Springob, M. Colless, D. H. Jones, L. Campbell, J. Lucey, and J. Mould, *Maximum-likelihood fitting of the 6dfgs peculiar velocities*, in *Advancing the Physics of Cosmic Distances*, vol. 8 of *Proceedings of the International Astronomical Union*, pp. 402–405, 8, 2012.

[169] E. Macaulay, H. A. Feldman, P. G. Ferreira, A. H. Jaffe, S. Agarwal, M. J. Hudson, and R. Watkins, *Power spectrum estimation from peculiar velocity catalogues*, *MNRAS* **425** (Sept., 2012) 1709–1717, [arXiv:1111.3338].

[170] R. Watkins and H. A. Feldman, *Large-scale bulk flows from the Cosmicflows-2 catalogue*, *MNRAS* **447** (Feb., 2015) 132–139, [arXiv:1407.6940].

[171] D. W. Hogg, D. J. Eisenstein, M. R. Blanton, N. A. Bahcall, J. Brinkmann, J. E. Gunn, and D. P. Schneider, *Cosmic Homogeneity Demonstrated with Luminous Red Galaxies*, *ApJ* **624** (May, 2005) 54–58, [astro-ph/0411197].

[172] M. I. Scrimgeour, T. Davis, C. Blake, J. B. James, G. B. Poole, L. Staveley-Smith, S. Brough, M. Colless, C. Contreras, W. Couch, S. Croom, D. Croton, M. J. Drinkwater, K. Forster, D. Gilbank, M. Gladders, K. Glazebrook, B. Jelliffe, R. J. Jurek, I.-h. Li, B. Madore, D. C. Martin, K. Pimbblet, M. Pracy, R. Sharp, E. Wisnioski, D. Woods, T. K. Wyder, and H. K. C. Yee, *The WiggleZ Dark Energy Survey: the transition to large-scale cosmic homogeneity*, *MNRAS* **425** (Sept., 2012) 116–134, [arXiv:1205.6812].

[173] A. Nusser and M. Davis, *The Cosmological Bulk Flow: Consistency with ΛCDM and $z \approx 0$ Constraints on σ_8 and γ*, *ApJ* **736** (Aug., 2011) 93, [arXiv:1101.1650].

[174] D.-C. Dai, W. H. Kinney, and D. Stojkovic, *Measuring the cosmological bulk flow using the peculiar velocities of supernovae*, *JCAP* **4** (Apr., 2011) 015, [arXiv:1102.0800].

[175] S. J. Turnbull, M. J. Hudson, H. A. Feldman, M. Hicken, R. P. Kirshner, and R. Watkins, *Cosmic flows in the nearby universe from Type Ia supernovae*, *MNRAS* **420** (Feb., 2012) 447–454, [arXiv:1111.0631].

[176] Y.-Z. Ma and D. Scott, *Cosmic bulk flows on 50 h^{-1} Mpc scales: a Bayesian hyper-parameter method and multishell likelihood analysis*, *MNRAS* **428** (Jan., 2013) 2017–2028, [arXiv:1208.2028].

[177] Y.-Z. Ma and J. Pan, *An estimation of local bulk flow with the maximum-likelihood method*, *MNRAS* **437** (Jan., 2014) 1996–2004, [arXiv:1311.6888].

[178] T. Hong, C. M. Springob, L. Staveley-Smith, M. I. Scrimgeour, K. L. Masters, L. M. Macri, B. S. Koribalski, D. H. Jones, and T. H. Jarrett, *2MTF - IV. A bulk flow measurement of the local Universe*, *MNRAS* **445** (Nov., 2014) 402–413, [arXiv:1409.0287].

[179] S. Appleby, A. Shafieloo, and A. Johnson, *Probing Bulk Flow with Nearby SNe Ia Data*, *ApJ* **801** (Mar., 2015) 76, [arXiv:1410.5562].

[180] D. Huterer, D. L. Shafer, and F. Schmidt, *No evidence for bulk velocity from type Ia supernovae*, *JCAP* **12** (Dec., 2015) 033, [arXiv:1509.0470].

[181] M. I. Scrimgeour, T. M. Davis, C. Blake, L. Staveley-Smith, C. Magoulas, C. M. Springob, F. Beutler, M. Colless, A. Johnson, D. H. Jones, J. Koda, J. R. Lucey, Y.-Z. Ma, J. Mould, and G. B. Poole, *The 6dF Galaxy Survey: bulk flows on 50-70 h^{-1} Mpc scales*, *MNRAS* **455** (Jan., 2016) 386–401, [arXiv:1511.0693].

[182] U. Feindt, M. Kerschhaggl, M. Kowalski, G. Aldering, P. Antilogus, C. Aragon, S. Bailey, C. Baltay, S. Bongard, C. Buton, A. Canto, F. Cellier-Holzem, M. Childress, N. Chotard, Y. Copin, H. K. Fakhouri, E. Gangler, J. Guy, A. Kim, P. Nugent, J. Nordin, K. Paech, R. Pain, E. Pecontal, R. Pereira, S. Perlmutter, D. Rabinowitz, M. Rigault, K. Runge, C. Saunders, R. Scalzo, G. Smadja, C. Tao, R. C. Thomas, B. A. Weaver, and C. Wu, *Measuring cosmic bulk flows with Type Ia supernovae from the Nearby Supernova Factory*, *A&A* **560** (Dec., 2013) A90, [arXiv:1310.4184].

[183] A. Conley, R. G. Carlberg, J. Guy, D. A. Howell, S. Jha, A. G. Riess, and M. Sullivan, *Is There Evidence for a Hubble Bubble? The Nature of Type Ia Supernova Colors and Dust in External Galaxies*, *ApJL* **664** (July, 2007) L13–L16, [arXiv:0705.0367].

[184] I. Zehavi, A. G. Riess, R. P. Kirshner, and A. Dekel, *A Local Hubble Bubble from Type IA Supernovae?*, *ApJ* **503** (Aug., 1998) 483–491, [astro-ph/9802252].

[185] R. C. Keenan, A. J. Barger, and L. L. Cowie, *Evidence for a ˜300 Megaparsec Scale Under-density in the Local Galaxy Distribution*, *ApJ* **775** (Sept., 2013) 62, [arXiv:1304.2884].

[186] J. R. Whitbourn and T. Shanks, *The local hole revealed by galaxy counts and redshifts*, *MNRAS* **437** (Jan., 2014) 2146–2162, [arXiv:1307.4405].

[187] S. Heß and F.-S. Kitaura, *Cosmic flows and the expansion of the local Universe from non-linear phase-space reconstructions*, *MNRAS* **456** (Mar., 2016) 4247–4255, [arXiv:1412.7310].

[188] H. Liu, R. Mohayaee, and P. Naselsky, *Critical points of the cosmic velocity field and the uncertainties in the value of the Hubble constant*, *JCAP* **6** (June, 2016) 009, [arXiv:1605.0515].

[189] R. B. Tully, H. M. Courtois, A. E. Dolphin, J. R. Fisher, P. Héraudeau, B. A. Jacobs, I. D. Karachentsev, D. Makarov, L. Makarova, S. Mitronova, L. Rizzi,

E. J. Shaya, J. G. Sorce, and P.-F. Wu, *Cosmicflows-2: The Data*, *AJ* **146** (Oct., 2013) 86, [arXiv:1307.7213].

[190] Y. Hoffman, H. M. Courtois, and R. B. Tully, *Cosmic bulk flow and the local motion from Cosmicflows-2*, *MNRAS* **449** (June, 2015) 4494–4505, [arXiv:1503.0542].

[191] M. Li, J. Pan, L. Gao, Y. Jing, X. Yang, X. Chi, L. Feng, X. Kang, W. Lin, G. Shan, L. Wang, D. Zhao, and P. Zhang, *Bulk Flow of Halos in ΛCDM Simulation*, *ApJ* **761** (Dec., 2012) 151, [arXiv:1207.5338].

[192] E. L. Turner, R. Cen, and J. P. Ostriker, *The relation of local measures of Hubble's constant to its global value*, *AJ* **103** (May, 1992) 1427–1437.